Fast 3D imaging in the auditory cortex of awake mice reveals that astrocytes control neurovascular coupling responses locally at arteriole-capillary junctions.

Barbara Lykke Lind[1,2*] and Andrea Volterra[1,3]

1. Department of Fundamental Neuroscience, University of Lausanne, Rue du Bugnon 9, 1005, Lausanne, Switzerland.

2. Department of neuroscience, University of Copenhagen, Blegdamsvej 3B, 2200 Copenhagen, Denmark.

3. Wyss Center for Bio- and Neuro-engineering, Chemin des Mines 9, 1202, Geneva, Switzerland

*Corresponding author: barbarall@sund.ku.dk

Abstract:

During neuronal activity, cerebral blood flow increases to ensure adequate glucose and oxygen supply, a crucial mechanism known as the neurovascular coupling response. Blood is drawn from the brain's surface through penetrating arterioles (PA) and locally redistributed via branching capillaries in the cerebral cortex. All blood vessels, regardless of cortical layer or size, are covered by astrocytic end-feet, suggesting a potential regulatory role. Though the regulatory machinery is known to be present in astrocyte end-feet, its role in this blood recruitment is still controversial. A likely explanation for the controversy is that studies so far have been done without considering the structural basis for blood flow regulation and the heterogeneity in blood vessel dilation patterns. We performed our experiments in awake mice, using a 3D+t two-photon imaging approach by which we could image regions at the branching point between PA and capillary bed at high speed. This led us to detect rapid, localized astrocytic Ca2+ signals in the end-feet surrounding the sphincter connecting the two vascular compartments. Mice often moved during experiments, and we noticed that in these cases, most of the natural vessel dilations in our imaged region were multicompartmental, extending from the PA to the 1st order capillary across the pre-capillary sphincter or vice versa. In contrast, when the mouse was at rest, dilations were more spatially restricted, with at least half of them remaining confined to one of the two compartments. The local Ca2+ rises in the end-feet encircling the pre-capillary sphincters preceded dilations spread and were notably correlated with multicompartment dilations. These Ca2+ signals were attenuated in IP3R2KO mice, lacking a major source of astrocyte Ca2+ rises, and the number of dilations crossing the sphincter was significantly reduced or slowed down compared to wild-type mice. When we induced dilations by auditory stimulation, we found that they had patterns and dependency on local astrocyte Ca2+ activity analogous to those of naturally occurring dilations. In conclusion, we discovered that pre-capillary sphincters play a pivotal role in the bidirectional dilation spread between vascular compartments and that local astrocyte Ca2+ signaling controls this function. This mechanism, described here for the first time, allows astrocytes to control the dilation transition across the sphincters and contribute to laminar blood flow regulation during neurovascular coupling responses.

Introduction

Adequate regulation of cerebral blood flow is the basis of healthy brain function. The neurovascular coupling (NVC) response ensures sufficient oxygen and energy during increased neuronal activity and, when impaired, contributes to pathophysiological alterations in several common cerebral diseases (Iadecola, 2017). The blood is recruited to the capillary bed from the brain surface via penetrating arterioles (PAs). The first branch point from the PAs into the capillary bed, the 1st order capillary, also dubbed precapillary arteriole (Hartmann et al., 2021; Hill et al., 2015) or post-arteriolar transition zone (Mughal, Nelson, & Hill-Eubanks, 2023), is a microvascular inflow tract believed to be critically important for blood flow regulation during NVC (Hartmann, Coelho-Santos, & Shih, 2022). Intriguingly, the presence of a gating structure, the pre-capillary sphincter, was recently described precisely at this level (Grubb et al., 2020). This structure expresses α-smooth muscle actin in its mural cells (αSMA) (Grubb et al., 2020; Hall et al., 2014; Zambach et al., 2021), which makes it contractile and capable of modifying vessel diameter. Changes in the sphincter diameter may then control the blood flow to the downstream brain tissue (Grubb, Lauritzen, & Aalkjaer, 2021). Astrocytes' end-feet continuously cover all the blood vessel segments and could, in principle, impose control at each level (McCaslin, Chen, Radosevich, Cauli, & Hillman, 2011). Intracellular Ca2+ increases in astrocytes can induce the release of vasoactive factors (Bazargani & Attwell, 2016), yet the role of astrocytes in blood flow regulation remains controversial. Notably, it is unclear if Ca2+ elevations in astrocytes are rapid and prevalent enough to contribute to blood flow recruitment (Howarth, Mishra, & Hall, 2021). To this point, different studies produced discrepant results: some reported that astrocytes recruit blood flow specifically at the capillary, not arteriole, level (Biesecker et al., 2016; Mishra et al., 2016), others that astrocytes regulate PA diameter, but only during extended sensory experiences (Institoris et al., 2022). In addition, some studies concluded that astrocytes do not exert any Ca2+-dependent regulation. This conclusion was based on the authors' inability to observe any changes in the NVC response in mice lacking IP3R2, the IP3 receptor isoform whose activation is considered to be the main source of intracellular Ca^{2+} elevation in astrocytes (Bonder & McCarthy, 2014; Del Franco, Chiang, & Newman, 2022; Nizar et al., 2013). However, all these studies looked at blood vascular dynamics in a simplistic manner, mainly focusing on individual compartments, disregarding the heterogenous nature of dilations progressing through the vascular bed (Longden et al., 2017; Rungta, Chaigneau, Osmanski, & Charpak, 2018; Rungta et al., 2021). Moreover, different studies used different imaging conditions to investigate astrocyte intracellular Ca^{2+} dynamics with respect to size, timing, and frequency of the recorded Ca2+ signals (Del Franco et al., 2022; Gu et al., 2018; Institoris et al., 2022; Lind et al., 2018; Nizar et al., 2013; Otsu et al., 2015; Ozawa et al., 2023; Petzold, Albeanu, Sato, & Murthy, 2008; Santello, Toni, & Volterra, 2019; Stobart, Ferrari, Barrett, Gluck, et al., 2018; Tran, Peringod, & Gordon, 2018; Wang et al., 2006; Winship, Plaa, & Murphy, 2007). Finally, most studies were performed in anesthetized mice in which both astrocytic Ca^{2+} (Bindocci et al., 2017; Thrane et al., 2012) and blood flow responses (Takuwa et al., 2012) are severely dampened. Overall, the several pitfalls affecting the studies so far do not allow for drawing firm conclusions on the role of astrocyte Ca2+ signaling in the control of brain hemodynamics.

In the present study, we aimed to overcome those pitfalls. To start, we performed our experiments in awake mice, which permitted us to consider the impact of the mouse activity state on the NVC response and the heterogeneity of the dilation patterns in different inherent conditions. Secondly, to our

knowledge, for the first time in NVC studies, we used a 3D+t two-photon imaging approach developed by our group (Bindocci et al., 2017), by which we could monitor entire regions (30-150 µm in the z-axis) at the branching point between penetrating arterioles and capillary bed. This approach enabled us to investigate vascular responses simultaneously at the PA, 1st order capillary, and connecting sphincter levels, as well as the Ca2+ activity in surrounding astrocyte structures. Thirdly, we imaged these stacks at high speed (10 Hz), capturing the full range of astrocytic Ca2+ dynamics, including fast and local signals.

Our observations indicate that the pattern of natural dilations at the PA-capillary junctions in the mouse auditory cortex differs depending on the inherent activity of the mouse. Some dilations are multicompartmental, whereas others remain confined to one of the two compartments. Astrocytes occasionally underwent large Ca2+ activations, but we also noticed smaller Ca2+ rises in the end-feet enwrapping the pre-capillary sphincters. Such local Ca2+ rises preceded the spread of the dilations and appeared in specific correlation with multicompartment dilations. Both the astrocyte Ca2+ activity and the spread of the dilations across the sphincter were affected in IP3R2KO mice. When we subjected mice to auditory stimulation, we observed dilation patterns analogous to those seen in naturally behaving mice and similarly dependent on astrocyte Ca2+ activity. We conclude that pre-capillary sphincters play a central role in the bi-directional spreading of dilations between vascular compartments and that astrocyte Ca2+ signaling controls their function locally.

Results

3D imaging of vessel dilations and astrocyte Ca2+ activity in the auditory cortex of awake mice: observations along the descending PA paths.

We investigated the astrocytic contribution to hemodynamic responses in the auditory cortex of awake mice (Figure 1A). First, we focused on the PA tracts. We mapped the surface vessels to identify appropriate positions for imaging, where PAs dive into the tissue, i.e., where in the vascular tree, the freshly oxygenated blood enters the cortex (Figure 1B). By 2-photon imaging, we then studied astrocyte and blood vessel dynamics along the descending PA paths. Astrocyte Ca2+ activity was visualized using the *GFAPCreERT2:GCaMP6f* mouse strain that enables astrocyte selective, inducible expression of the green Ca2+ indicator GCaMP6f upon tamoxifen (TAM) injections (Methods). In parallel, PA dynamics were revealed by loading blood vessels with red fluorescent dyes (Texas Red, TRITC-dextran or SR101) to highlight their lumen. In this first set of experiments, we positioned our three-dimensional fields of view (3D-FOV) along the PAs to cover descending tracts up to 280 µm in the z dimension (Figure 1C). The fast 3D imaging approach (Bindocci et al., 2017) enabled us to monitor vascular and astrocyte dynamics quasi-simultaneously in multiple focal planes along the z-axis (Figure 1C, Sup. figure S1). Our investigation of the astrocyte dynamics focused on the Ca2+ activity within the end-feet, as they represent the contact points of the astrocytes with the contractile vascular cells. The end-feet regions of interest (ROIs) were automatically defined as the structures present within 2µm from the vessel surface in each z-plane and repositioned during vascular dynamics, according to the vessel diameter changes (Sup. figure S1). In this way, we followed astrocyte end-foot Ca2+ activity along single PAs while tracing the volume changes occurring in the corresponding PA segments (Figure 1D). Some end-feet Ca2+ activities would spread far

along the PA and cover up to 205 µm in the z-dimension, whereas others were local and could not be seen beyond an individual focal plane (Figure 1E, Sup. figure S2A). The duration of the activity only partly explained how far it spread. (Sup. figure S2B). As for the spontaneous PA dilations that we observed, only about half (324/668) occurred in the presence of end-foot Ca2+ activity along the PA. But, when the two phenomena coincided, the spread of dilations was larger, reaching further down inside the cortex (Figure 1F). Moreover, the spread of the PA dilations correlated with the spread of the end-foot Ca2+ activity (Sup. figure S2C). Very large astrocytic Ca^{2+} elevations are known to occur during mouse locomotion (Bindocci et al., 2017; Paukert et al., 2014; Tran et al., 2018). To detect the mouse movements, we recorded EMGs via electrodes implanted in the neck muscles of the animals (Figure 1D, bottom). We found that the spread of the astrocytic end-foot Ca2+ activity in the z-direction almost doubled during mouse movements with respect to when the mouse was at rest, changing, on average, from 23±3µm to 50±7µm (Figure 1E).

As others before, we found that not all mouse movements triggered an astrocytic Ca2+ activity in the end-feet along the PA (Tran et al., 2018). Still, less than 30% of PA dilations seen during mouse movements (78/262) arose without Ca2+ activity in the astrocyte end-feet. This was a lower proportion than in the resting mouse. Again, dilations spread further when coinciding with Ca2+ increases in the end-feet (Figure 1G). These data suggest that end-foot Ca2+ activity influences PA dilations without, however, being a prerequisite for the dilations to occur.

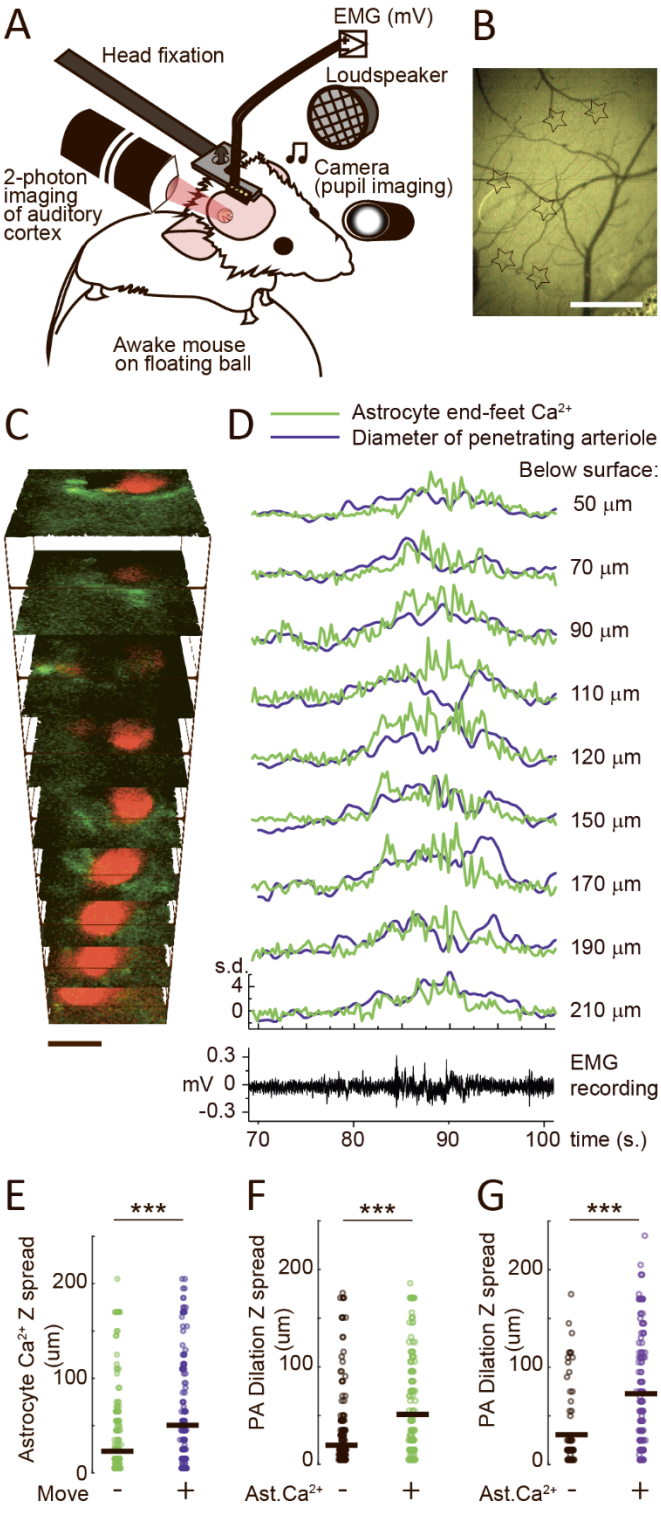

Figure 1. 3D imaging of the PA dynamics in the auditory cortex of awake mice: both naturally occurring dilations and astrocytic Ca2+ activity spread along the descending PA path.

A. Complete setup for our experiments in chronically implanted head-fixed awake mice.

B. Brightfield image of the vessels at the surface of the auditory cortex seen from the chronic cranial window. Visual inspection of the blood flow direction in vessels allows distinction between arterioles and venules. *Stars*: PAs. Scale bar: 500µm

C. Representative cumulative average of the 3D timeseries taken in the auditory cortex of a *GFAPCreERT2:GCaMP6f* mouse (green, reporting astrocyte Ca2+ activity) injected in the circulation with Texas red dextran (red, reporting vessels lumen). Imaging was performed in 20 µm z-steps, from 50 to 210 µm below the surface (x=75.5 µm; y=75.5 µm). Scale bar: 20µm

D. *Top:* Example traces reporting simultaneous astrocyte end-foot Ca2+ activity (mean fluorescence) and PA diameter (area) changes normalized to SD values in the different z-planes of our 3D-FOV, before and during a period of mouse locomotion. The resting periods are used as baseline. *Bottom*: The movements are visible in the electromyogram (EMG) recorded from the mouse's neck muscles throughout the imaging session.

E. Spread of end-foot astrocyte Ca2+ activity along the length of the PA; *green*: mouse is resting; *violet*: mouse is moving (Mann-Whitney test: $p=1.8*10^{-11}$; N=668 Ca2+ events in the resting mouse and 262 in the moving mouse).

F. Spread of PA dilations along the length of the PA in the resting mouse; *black*: without Ca2+ activity in the astrocyte end-feet; *green*: with the astrocytic Ca2+ activity (Mann-Whitney test: $p=5.7*10^{-16}$; N=324 dilations without astrocyte Ca2+ and 344 with Ca2+).

G. Spread of PA dilations along the length of the PA as in E, but in the moving mouse; *black*: without Ca2+ activity in the astrocyte end-feet; *violet*: with the astrocytic Ca2+ activity (Mann-Whitney test: $p=1.5*10^{-9}$; N=78 dilations without astrocyte Ca2+ and 184 with Ca2+).
In E-G, data are from 8 FOVs: x=75-121 µm; y=53-111 µm; z=100-280 µm, in 10-20µm steps from 6 mice.

3D imaging of vessel dilations and astrocyte end-foot Ca2+ activity in the auditory cortex of awake mice: observations at the PA-capillary junction.

While PA dilations increase blood flow distribution to many cortical layers, a second and more specific level of regulation occurs at capillary branching points at different cortical depths (Ostergaard, 2020). There, an increased blood flow in one of the 1st order capillary branches enhances the delivery to areas downstream of the branch (Hartmann et al., 2022). Recently, a pre-capillary sphincter was described at the junction with the PA, at least in the barrel cortex (Grubb et al., 2020). Therefore, we decided to focus our study on this junction in the auditory cortex (Figure 2A). Via the luminal red fluorescence, we visualized the sphincter as a narrowing of the lumen proximal to the PA. In addition, in 50% of the junctions (n = 20), we noticed the presence of a bulb at the capillary edge, likely generated by a reduction in the number of contractile cells at that level (Cai et al., 2023). We found that the shape of the PA-capillary junction varied and that the indentation was less obvious at some junctions. Since contractile mural cells completely cover this part of the vascular inflow tract, they are all contractile (Cai et al., 2023; Grubb et al., 2020) The morphological differences likely reflect the extent of force in that contractility. Because we saw a continuum in the size of the indentations, but some degree of pre-constriction on all but one junction, we decided to define all connections between a PA and the 1st order capillary as sphincters. Initially, we used a few *GFAP-EGFP* mice with green-fluorescent astrocytes (Nolte et al., 2001) to investigate the position of the astrocytic structures at the vascular junction. The EGFP-positive astrocytes were positioned at the branching points (Figure 2A), covering most of the 1st order capillary up to and in contact with the sphincter (Figure 2B). To detect the potential role of these astrocytes, we then performed dynamic studies in TAM-treated *GFAPCreERT2:GCaMP6f* mice, centering our 3D-FOV at the level of the junction between the PA and the 1st order capillary. Thus, in the following text, when we write capillaries, we refer only to the 1st order capillaries. These 3D-FOVs were much smaller than those for studies along the PAs and taken at 1µm steps to ensure continuous imaging around the vasculature. Our fast two-photon scanning settings permitted quasi-simultaneous investigation of the dilation patterns of the two vascular compartments, together with rapid Ca^{2+} changes in astrocyte end-feet ROIs at both the arteriole and capillary levels (Sup. Figure S3). Thus, we could define the location and temporal sequence of astrocyte Ca2+ elevations relative to the vascular volume changes. In previous recordings in awake mice from 3D-FOVs with similar dimensions (Bindocci et al., 2017), we detected both spatially restricted and much larger Ca2+ activities in the astrocytic end-feet. The two types of activity were substantially different: the former was asynchronous and small (µm-scale), generally restrained within a single end-foot, whereas the latter expanded widely to occupy several end-feet in different z-planes. In the recordings around the vascular junction, we observed a large astrocytic Ca2+ elevation every few minutes that invaded ≥75% of the end-foot ROIs present in all z-planes of our 3D-FOV. We defined these events as

"large Ca2+ activities" (Figure 2C) and found that 71±7% of them overlapped in time with the movements of the mouse (Sup. figure S2D-G). Large astrocytic Ca^{2+} elevations are known to occur during arousal states driven by noradrenaline release (Ding et al., 2013). Such states are faithfully signaled by the animal's pupil expansions (Larsen & Waters, 2018; Privitera et al., 2020; Reimer et al., 2016; Reitman et al., 2023). Thus, we monitored the mouse pupil diameter during the imaging sessions using an IR-camera to verify if large astrocyte Ca2+ activities coincided with pupil expansions. While most pupil expansions occurred without a large astrocytic Ca^{2+} response, when such an activity occurred, it almost always (92 ± 13% of the cases) coincided (within 1 sec) with a pupil expansion, suggesting its association with the arousal state (Sup figure S2H). As observed for the dilations along the PA path, dilations around the junction were also not just triggered by animal movement or by large astrocytic Ca2+ elevations. Indeed, the majority of these dilations (75.4±5.9%) occurred when the mouse was at rest and in the absence of any large astrocytic Ca2+ activity. The temporal sequence of the large astrocytic Ca2+ responses seen during mouse movements indicates that astrocyte Ca2+ rises after the onset of movements (by 1.0 ± 1.25s, Sup. figure S2F). The onset of the Ca2+ response was in some cases earlier than the onset of the dilation, but on average this response rose after vessel dilations (by 2.3 ± 0.84s, Figure 2D). Therefore, while the large end-foot astrocytic Ca2+ elevations appear to be associated with movements and arousal states of the mice, they are not involved in triggering dilations at the junction where the 1st order capillaries branch from PAs into the capillary bed during movements.

Bidirectional spread of dilations at the pre-capillary sphincter: dependence on the activity and arousal state of the awake mouse.

During our repeated 2-minute 3D-imaging sessions, we detected many spontaneous vessel dilation events at the junction (Sup. Figure S3). We expected them to be a consequence of the NVC response to natural sound perception accompanied by increased excitation and metabolic needs of auditory neurons. We noticed, however, a large variation in the characteristics of such dilation events depending on whether the mouse was moving or resting at the time when they happened, as well as on the presence or not of large astrocytic Ca^{2+} activity (Figure 2E and F). Notably, if the mouse was moving, dilations lasted significantly longer (mean duration: 4.5 ± 1.16 s) than if the animal was at rest (3.06 ± 0.27 s, Figure 2E). Moreover, most of them (77%) were multicompartment, involving both PA and the capillary branch (Figure 2F). In contrast, if the mouse was resting, >50% of the dilations were mono-compartment and remained confined to either the vessel tract upstream of the sphincter or to the tract downstream. In the case of dilations occurring during mouse movement, the co-presence of a large astrocytic Ca2+ activity prolonged dilations further (Figure 2E), and almost all of them (92%) became multicompartmental (Figure 2F). Also, in the resting mouse, dilations were prolonged by the occurrence of a large astrocyte Ca2+ event (Figure 2E). However, the fraction of multicompartment dilations did not increase (Figure 2F). These data indicate that the animal movements, and to a lesser degree arousal, shape the hemodynamic responses in the auditory cortex and prolong dilations in time and space.

Next, we analyzed the origin and direction of the dilations in the different conditions. Since only 51±5% % of dilations during rest were multicompartment, i.e., involved both PA and capillaries, we wondered which part of the vascular bed would dilate alone in the remaining ones (Figure 2G). We found that the

monocompartment dilations most frequently involved the capillary branch (37%±6% of all the dilations at rest) followed by the PA (12±3%) (Figure 2G; Sup. figure S2J). This heterogeneity was also reflected in the origin and directionality of the multicompartment dilations. We found that some appeared first at the PA, others at the junction, and others at the capillary level. Only dilations first seen at the junction certainly originated within our 3D-FOV. They were a smaller fraction: 24 ± 4% of them started at the sphincter and even fewer at the bulb. The remaining ones, in general, originated outside the 3D-FOV; in 33 ± 5% of the cases, they were seen coming from the PA and in 32 ±6% of cases from the capillary bed (Figure 2H). When dilations spread across the sphincter, they were not necessarily progressing from one vessel segment to the next. In 43±9% of the multicompartment dilations, the sphincter dilation was slightly later. The heterogeneity in the sites of origin did not depend on whether the mouse moved or was at rest or whether the dilation was accompanied by a large astrocytic Ca2+ event or not (Sup. figure S2K). The site of origin did not influence the characteristics (volume and duration) of the dilations in each vascular compartment, which were instead modulated by the mouses' behavior and by the occurrence of large Ca2+ activity in astrocyte end-feet (Sup. figure S4). On the other hand, the co-existence in the resting mouse of monocompartment dilations stopping at the sphincter and of multicompartment dilations crossing it (Figure 2I) indicates that the pre-capillary sphincter is a site of control of the dilations' spread. Such control was overcome during animal movements or arousal states, notably when associated with large astrocytic Ca^{2+} events, with recruitment of both the upstream and downstream vascular compartments, independent of the initiation site and the direction of the dilation. This observation put regulation of the sphincter diameter centerstage.

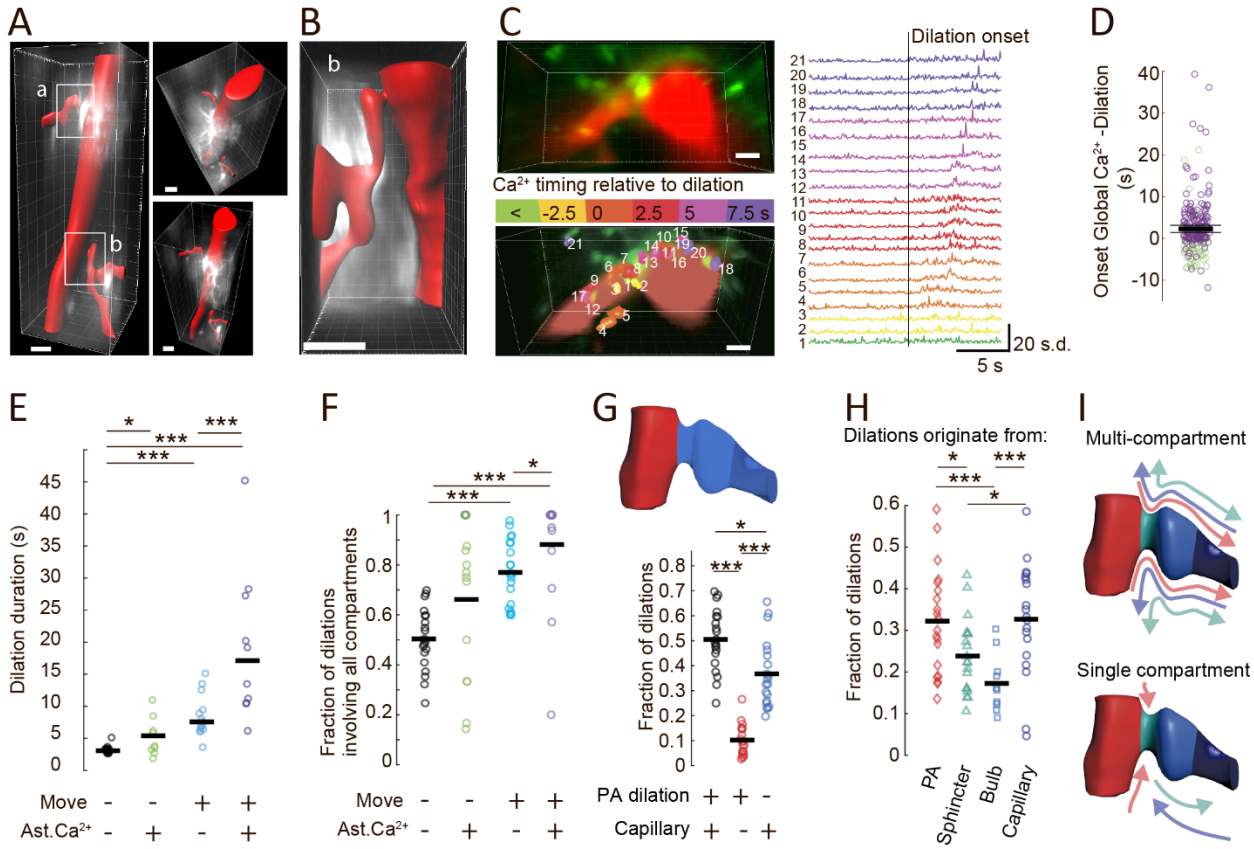

Figure 2. Spread of naturally occurring dilations in the auditory cortex of awake mice is gated at the sphincter between PA and capillary compartments. Correlation with end-foot astrocyte Ca2+ dynamics and animal motor state.

A. Reconstruction of a 3D stack imaged live from 90 to 360 µm below the surface in the auditory cortex of an *EGFP-GFAP* mouse. The reconstruction shows from two sides a penetrating arteriole delivering blood into the tissue and two 1st order capillaries branching at different depths of the cortical layer II/III (a and b white squares on the right). *Red*: Texas red-dextran highlights vessels lumen; *white*: EGFP signal shows a reconstruction of the astrocyte larger processes. Scale bar: 20 µm.

B. Zoom in on the 3D stack shown in A, depicting the lower branch (b) region shown from above (*left*) and the side (*right*, from 250 to 330 µm below the surface). Colors as in A. Scalebar 20µm

C. A representative cumulative average of a 3D time series, taken from a *GFAPCreERT2:GCaMP6f* mouse injected with Texas red-dextran in the vessel. The 3D-stack was imaged from 170 to 200 µm below the cortical surface, at 30 levels 1 µm apart. *Left, top*: cumulative signals show in red the vessel lumen and in green the neighboring astrocyte structures. *Left, bottom*: the same picture as above, but with multiple astrocyte Ca2+ activity ROIs measuring a large astrocytic Ca2+ event associated with the animal's locomotion and a dilation initiated at the pre-capillary sphincter. Ca2+ activity ROIs are color-coded to appreciate their temporal-spatial dynamics (Ca2+ onset time) relative to the dilation onset. The red signal is masked to show the 3D structure of the vessel.

Right: Traces of mean astrocyte end-foot Ca2+ activity from each ROI. ROI and traces are color-coded in relation to the timing of dilation onset. Scale bar: 8µm

D. Delay between onset time of all large astrocytic end-foot Ca2+ activity and onset time of the vessel dilation in the 3D-FOV in the resting (*green*) and moving (*violet*) mouse. Mean Delay 2.3±0.86 s (Mean: *Thick black line,* 95% C.L. limits *thin black lines*). N=223 dilation events in the moving mouse accompanied by large astrocyte Ca2+ activity.

E. Average duration of dilations per 3D-FOV in different conditions. *Black*: in the resting mouse when no astrocyte Ca2+ activity is observed; 162±31.2 dilations/FOV); *green*: in the resting mouse in the presence of large astrocyte Ca2+ activity (4.2±2.0 dilations/FOV); *azure*: in the moving mouse when no astrocyte Ca2+ activity is observed (47.6±22.1 dilations/FOV); *violet*: in the moving mouse in the presence of large astrocyte Ca2+ activity (6.5±2.5 dilations/FOV). All conditions: N=20 FOVs in 6 mice. Dilations occurring in the resting animal were significantly longer when accompanied by an astrocyte Ca2+ event (t-test: without vs. with Ca2+, p=0.0046), but significantly shorter than dilations occurring during mouse movements, accompanied or not by astrocyte Ca2+ (t-test: resting vs. moving without Ca2+: p= $6x10^{-7}$; resting vs moving with Ca2+: p = $3.3x10^{-6}$). Dilations during mouse movements were significantly longer when accompanied by an astrocyte large Ca2+ activity (t-test: moving vs moving with Ca2+: p= 0.0016). N=20 FOVs, T-tests were Paired, Two-tailed, and after a Holm correction for multiple comparisons.

F. Average fraction of dilations per 3D-FOV comprising all the vessel compartments in the FOV in different conditions. Color coding, conditions, number of dilations analyzed/FOV, number of FOV, and number of mice are as in E. The fraction of dilations significantly increased when the mouse moved with respect to when it was at rest, both when a large astrocyte Ca2+ activity accompanied the movement and when it did not (Wilcoxon test with Holm correction: resting without vs. with Ca2+: p=0.059; resting vs moving, both without Ca2+: p= 0.00019; resting vs moving with Ca2+: p=0.00016). The fraction of multicompartment dilations in the moving mouse further increased when movement was accompanied by an astrocytic Ca+ elevation (Wilcoxon test with Holm correction: moving without Ca2+ vs moving with Ca2+: p=0.013).

G. Average fraction of dilations per 3D-FOV in the resting animal according to the involved vessel compartments. *Top*: Representation of the vascular compartments present in the 3D-FOV in all our experiments. The different vascular compartments have been subdivided and depicted in different colors as PA (*red*), and the capillary branch, comprising the sphincter, bulb and 1st order capillary (*blue*). *Bottom*: Average fraction of dilations involving either all the compartments (multicompartment, *black*) or each of them individually according to color coding. 162±31.2 dilations/FOV, N=20 FOVs, 6 mice. Half the dilations where multicompartment, while the other half involved each compartment individually, with significantly more dilations occurring in the capillary branch (*blue*) compared to the PA (*red*). Wilcoxon test with Holm correction: multicompartment vs. PA: p =1.4×10^{-4}; multicompartment vs. capillary branch: p= 0.015; capillary branch vs PA: p= 1.0×10^{-4}.

H. Average fraction of dilations per 3D-FOV in the resting mouse according to the compartment in which they originate: segmented compartments are depicted with different colors and symbols: PA (*red, diamond*), sphincter (*cyan, triangle*), bulb (*light blue, square*), capillary (*dark blue, circle*); 162±31.2 dilations/FOV, N=20 FOVs, 6 mice. Dilations had heterogeneous origin and direction,

with significantly higher fractions originating from PA and capillary than from sphincter and bulb (After Kruskal Wallis test, Wilcoxon test with Holm correction: PA vs. sphincter: $p = 0.032$; PA vs bulb: $p = 4.4 \times 10^{-4}$; capillary vs sphincter: $p = 0.025$; capillary vs bulb: $p = 1.3 \times 10^{-3}$.

I. Illustration of the direction of spreading of the dilations across the sphincter according to the compartment of origination (color-coding as in H). *Top*: multi-compartment dilations; *bottom*: single-compartment dilations.

All data in this figure are from N=20 FOVs in 6 mice. 3D imaging coordinates: x=56-75 µm; y=15-44 µm; z=21-35 µm in 1µm steps.

Local Ca^{2+} activity in astrocytic end-feet at the sphincter precedes the arrival of multicompartment dilations.

In evaluating the role of astrocytes in the NVC response to auditory activation, large astrocytic Ca2+ elevations seen during mouse movements/arousals are likely confounding factors. According to recent data, they would rather be involved in associating brain states (Reitman et al., 2023) or in integrating past events (Rupprecht et al., 2024), which makes them irrelevant in the initiation of NVC. Therefore, we decided to focus our investigations on dilations and astrocyte Ca2+ elevations occurring during the animals' resting periods. (Figure 2A), we hypothesized that an astrocyte Ca^{2+}-based regulation could occur at the junction and focused our attention on the astrocyte Ca2+ activity related to multicompartment dilations spreading across the sphincter. By placing ROIs on local fluorescent maxima in time-averaged 3D images, we noticed the presence of heterogeneous Ca2+ activities in the astrocyte end-feet and processes around the junction (Sup. figure S5), which remained locally circumscribed and did not spread widely as the large Ca2+ activities did (Figure 2C). Intrigued by this, we developed an automated, context-dependent analysis of the astrocytic end-feet Ca2+ activity. To establish the spatial-temporal sequence of these local astrocyte Ca2+ events and of the dilation events in an unbiased and accurate way, we aligned the 3D astrocyte Ca2+ imaging data to the onset of all the spontaneous dilations. We then identified voxels of interest (VOIs) with increased Ca^{2+} activity in the astrocytic end-feet (Sup. figure S6). We evaluated the probability that a Ca^{2+} increase occurred within the VOIs prior to a given dilation pattern (Sup. figure S6). Thereby, we identified VOIs that consistently responded in a defined temporal relation with a dilation (Figure 3A, Sup. figure S6), i.e., we identified the position and timing of pre-dilation Ca^{2+} activities in the astrocytic end-feet. Although positions of the automatically generated VOIs and time-course of the related Ca2+ activities varied (Figure 3A), pre-dilation Ca2+ responses were found primarily in the end-feet covering the sphincter (Figure 3B), and their frequency was higher in the multicompartmental dilations that spread across it (Sup. figure S7A). These Ca2+ responses were not associated with a defined origin and direction of the multicompartment dilation (Figure 3B; Sup Fig S7B and C). Some local Ca2+ activity was present in end-feet along the capillary (Figure 3A and B; Sup Fig S7B), especially in association with dilations arriving from the capillary bed (Sup Fig S7B), while pre-dilation Ca2+ activity in the end-feet on the PA was rarely seen (Figure 3B; Sup Fig S7B). Regardless of their position, all the pre-dilation Ca^{2+} signals were local (9.7 ±3.8 µm z-axis) and short-lasting (0.98 ± 0.42 s) (Figure 3C). As for the interval between pre-dilation astrocyte Ca2+ elevations at the sphincter and dilation onset, this appeared to be longer (earlier Ca2+ elevations) when dilations arrived from upstream or downstream locations than when dilations started at the sphincter itself (Figure 3D and E). However, this longer anticipation of the Ca2+ signals might not be real because dilations coming from PA or capillaries were

likely initiated outside the FOV, i.e., earlier than observed. This been said, when the dilations started at the level of the capillary bed and arrived at the sphincter, pre-dilation astrocyte Ca2+ events occurred first at the sphincter and then at the capillary (Figure 3D and F). This sequence did not, however, visibly depend on the spreading of the Ca2+ from the sphincter along the capillary (sup. Figure S7D and E). Rather, there appeared to be two temporally separated groups of end-foot astrocyte Ca2+ events (Figure 3A, D-F and Sup. figure S7F). Suggesting that the activity at the sphincter is the primary event in the astrocytic end-feet before the dilations. Overall, the pre-dilation astrocyte Ca2+ activity at the sphincter showed anatomical and temporal characteristics in line with a possible role in controlling the spreading of dilations across the sphincter.

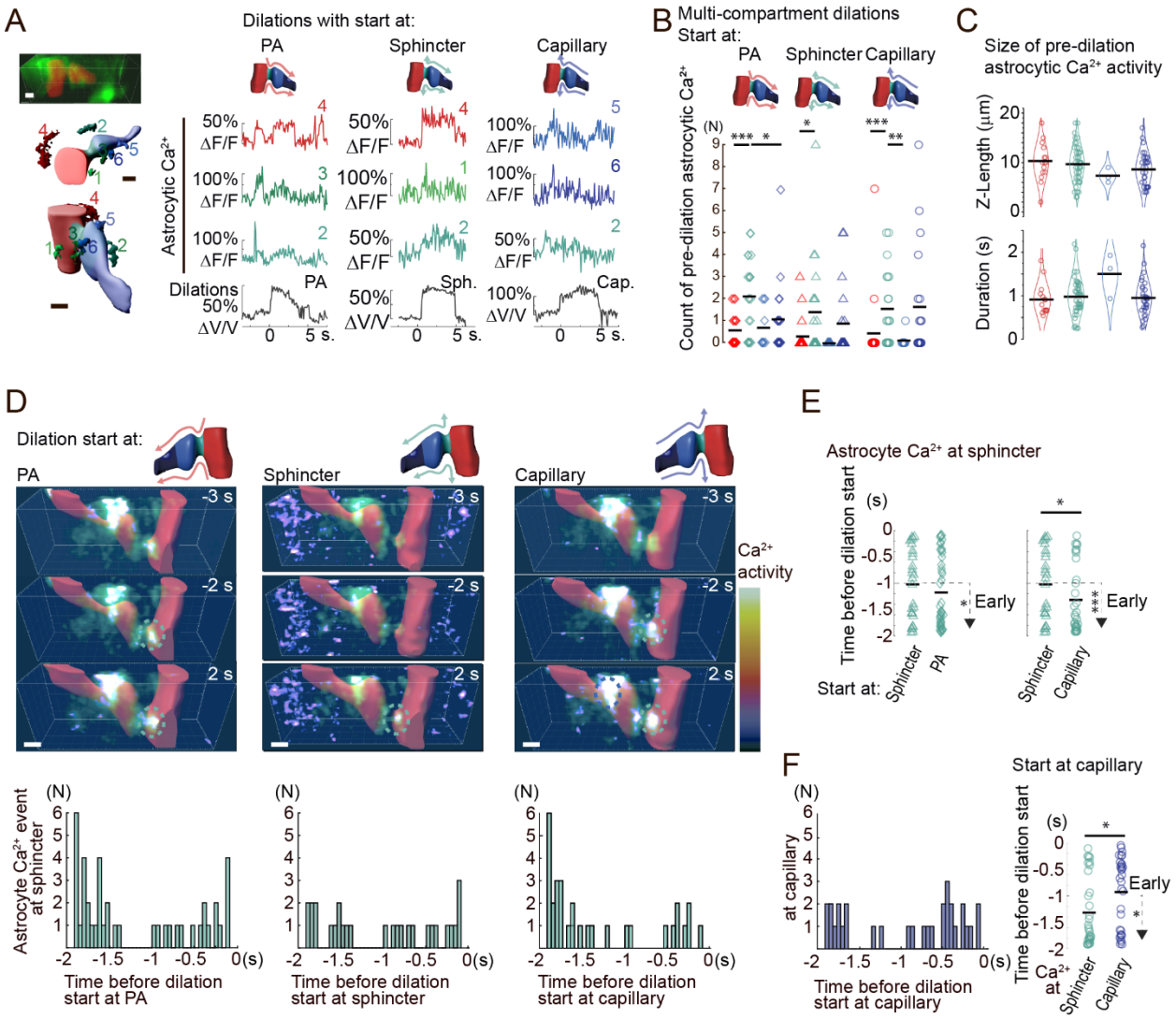

Figure 3. Local Ca^{2+} activity in astrocytic end-feet at the sphincter precedes multicompartment dilations arriving from distant vascular compartments in the resting mouse.

A. Representative data showing local astrocyte end-foot Ca2+ activity preceding dilations originating in different compartments in our 3D-FOV (x=56.6µm; y= 17.5µm; z: from 194 to 216µm below the brain surface in 1µm steps). *Left, top*: cumulative average of the GCaMP6f (end-feet) and Texas-Red (vessel lumen) signals; *bottom*: the same vascular structures (*red*: PA; *cyan*: sphincter; *blue*: bulb/1st order capillary) shown in two different orientations with several astrocytic VOIs at different locations around the junction corresponding to the end-foot regions displaying pre-dilation Ca2+ activity shown in the traces on the *right*. Numbers identify each VOI and the color its position on the vasculature. *Right*: Representative traces showing: *top*: time-course of astrocyte Ca2+ dynamics in VOIs numbered on the *left* during three dilations starting either at the PA (left column), the sphincter (middle column), or the capillary (right column); *bottom:* for each column, corresponding time-course of the dilation at the specific vessel segment where the dilation began. Pre-dilation Ca2+ activity appeared at several astrocyte end-foot locations, consisted of either individual peaks or more composite patterns, and was seen first in VOIs closest to the sphincter, including with dilations arriving from the PA or the capillaries. Scale bars: 5µm.

B. Analysis of local pre-dilation end-foot astrocyte Ca2+ elevations associated with multicompartment dilations. Quantification is by the number of end-feet VOIs with recurrent pre-dilation Ca2+ activity per FOV. Colors indicate the vascular location of the Ca2+ elevation (*red*: PA; *green*: sphincter; *light blue*: bulb; *blue*: capillary); symbols indicate the compartment of origination of the dilation (*diamond*: PA; *triangle*: pre-capillary sphincter; *empty circle*: capillary). Data are from 20 FOVs in 6 mice. End-foot Ca2+ events occurred more frequently at the sphincters, independent of the dilation initiated at the PA, the sphincter, or the capillaries. Tested with Kruskal Wallis ANOVA, then Wilcoxon with Holm-correction for multiple comparisons: (a) dilation starting at PA: end-foot Ca2+ at sphincter vs. at PA p= 5.5x10-4; at sphincter vs. at bulb: p=0.062; at sphincter vs. at capillary: p = 0.027; (b) dilation starting at sphincter: end-foot Ca2+ at sphincter vs. at PA: p = 0.006; at sphincter vs. at bulb: p=0.25; at sphincter vs. at capillary: p = 0.41; (c) dilation starting at capillaries: end-foot Ca2+ at sphincter vs at PA: p = 0.0011; at sphincter vs at bulb: p=0.048; at capillary vs at sphincter: p=0.21. The number of dilations/FOV starting at PA, sphincter and capillary, respectively, was 116.1±24.7, 82.4±19.7, and 67.2±16.2. N=20 FOV.

C. Properties of the local astrocyte end-foot Ca2+ activities observed at four different vascular locations before multicompartment dilations. Ca2+ activities are color-coded according to the vascular compartment where they are seen (*red*: PA; *green*: sphincter; *light blue*: bulb; *blue*: capillary). *Top*: spread of the end-foot Ca2+ activity along the z-axis (at PA: 10.1 ±1.9 µm; sphincter: 9.7 ±1.13 µm; bulb: 7.3 ±1.7 µm; capillary: 8.6 ±1.2 µm). *Bottom*: duration of the Ca2+ activity (at PA: 0.91 ±0.18 s; sphincter: 0.98 ±0.13 s; bulb: 1.5 ±0.58 s; capillary: 0.94 ±0.15 s). Data are from 20 FOVs in 6 mice.

D. Timing of the astrocytic end-foot Ca2+ activity associated with multicompartment dilations with different origination (*left*: PA; *middle*: sphincter; *right*: capillary bed). *Top*: Representative time-series of 3D-FOV (x= 75.5µm, y= 23.6µm taken from 95 to 125 µm below brain surface). Images are taken 3 sec before, 2 sec before and until 2 sec after the dilation start. In *red*: Texas red-dextran masked signal highlighting vessel lumen; in *green*: cumulative astrocyte GCaMP6f signal highlighting active perivascular end-feet; *pseudocolor* scale: Ca2+ activity levels normalized to show Ca2+ changes per voxel. *Dotted line circles* highlight astrocyte Ca2+ activity at the sphincter

(*green*) and the capillary (*blue*). The activity is most precocious and intense when dilations arrive from PA or capillaries. Scale bar: 7µm. *Bottom*: Distribution of the onset times of astrocytic Ca2+ signals seen at the sphincter before multicompartment dilations starting at different vessel compartments.

E. Comparison of the onset time of the different groups of pre-dilation Ca2+ activity shown in D. *Left*: timing of the pre-dilation Ca2+ signals for dilations starting at the sphincter vs the PA. On average, there is no significant difference in onset time, but the number of early events (onset >1 sec before dilation) is significantly higher for dilations starting at PA (Wilcoxon test; onset time: p=0.15; count of early events: p=0.029). *Right*: Same comparison but with dilations starting at the sphincter vs capillary. In this case, both onset time and number of early events are significantly different: end-foot Ca2+ activity starts earlier when dilations initiate at the capillary, and there are more early events (Wilcoxon test: onset time: p=0.027; count of early events: p=5.8x10-4). The number of Ca2+ events detected before dilations starting at PA, sphincter and capillary, respectively, was N= 42, 28 and 31. The number of dilations/FOV analyzed starting at PA, sphincter, and capillary, respectively, was 116.1±24.7, 82.4±19.7, and 67.2±16.2. All data from 20 FOVs in 6 mice.

F. Comparison of the onset times of astrocyte Ca2+ activities seen at the sphincter and at the capillary before arrival of multicompartment dilations from the capillary bed. *Left*: Distribution of the Ca2+ signals at the capillary (*blue*). *Right*: The onset time was earlier, and there were more early end-foot Ca2+ activities around the sphincter than at the capillary (Onset time: Mann-Whitney test p=0.016 N= 31 Ca2+ events; early Ca2+ events: Wilcoxon test, p=0.03, 67.2±16.2 dilations/FOV, from 20 FOVs in 6 mice.

The astrocytic pre-dilation Ca^{2+} activity in end-feet at the sphincter is reduced in IP3R2KO mice.

We then determined if the local pre-dilation astrocytic Ca^{2+} activity was IP3R2 dependent by repeating experiments in IP3R2KO mice, in which a large part, albeit not all, of the astrocyte end-foot Ca2+ activity observed in the awake mouse is suppressed (Srinivasan et al., 2015). Indeed, in this group of mice, we observed a significant reduction in the number of local pre-dilation Ca2+ signals in astrocyte end-feet, particularly at the sphincter, compared to wild-type mice (Figure 4A-C, Sup. figure S8). The count of pre-dilation activity at the PA and capillary was not significantly reduced (Sup. figure S8A and B). The reduction was most evident in association with multicompartment dilations, independent of whether they arrived from the PA or the capillary (Sup. figure S8C), and it affected particularly the earliest pre-dilation Ca^{2+} activity, namely the events starting >1 s before dilation onset (Figure 4D; Sup. figure S8D-E), and those closest to the sphincter (Figure 4E; Sup. figure S8D-E). Overall, these results support the presence of an early, pre-dilation, IP3R2-dependent, Ca2+ increase in astrocytic end-feet, notably in those surrounding the pre-capillary sphincter, prior to the spread of dilations beyond the branch point.

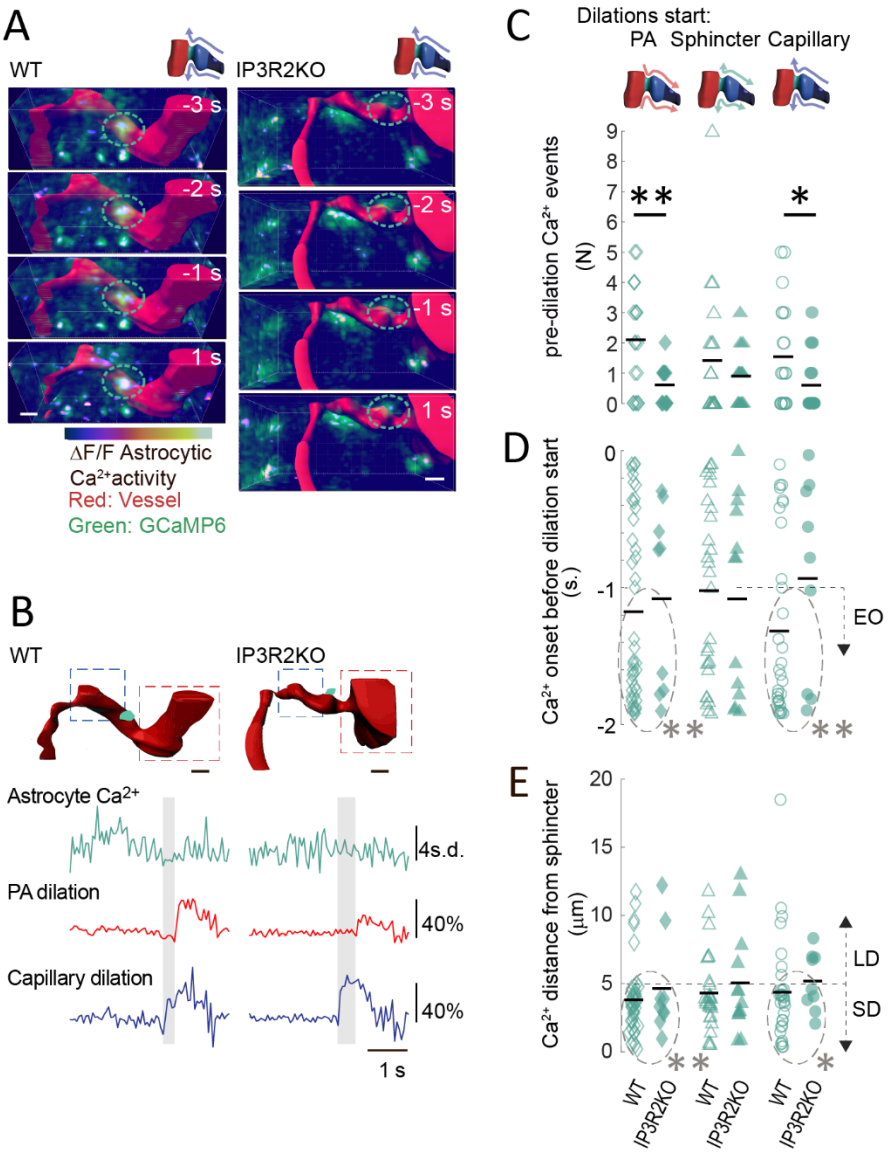

Figure 4. Pre-dilation astrocytic Ca^{2+} activity at the sphincter is suppressed in IP2R2KO mice; the events that occur at the earliest and closest to the sphincter are the most affected.

A. Pre-dilation astrocyte end-foot local Ca2+ dynamics in wild-type (WT) and IP3R2KO mice. Representative time-series in the period from 3 sec before to 1 sec after the start of a vasodilation at the capillary bed that spreads to the PA. Each image is the cumulative average of 1 s interval in a 3D-FOV in *left*: WT (x=75.5 µm, y=23.6 µm, z=170-200 µm below the cortical surface) and *right*: IP3R2KO (x=75.5 µm, y=30.7 µm, z=138-162µm below the surface). In *red*: masked vessel lumen; in *green*: cumulative astrocyte GCaMP6f showing active end-feet; *pseudocolor scale*: normalized Ca2+ activity. *Dotted line circles* highlight astrocyte Ca2+ activity at the sphincter. Scale bars: 7µm.
B. Comparison of pre-dilation astrocyte Ca2+ signals and vasodilation in WT and IP3R2KO mice. *Top*: astrocyte Ca2+ signals and vasodilations are measured in two ROIs spatially related to the vascular segments undergoing vasodilation starting at the 1st order capillary level (*blue*) and spreading to

the PA (*red*). *Bottom*: representative astrocyte Ca2+ and vessel dilation traces in the defined ROIs. The pre-dilation Ca2+ signals are reduced, and the PA dilation is delayed in the IP3R2KO mouse.

C. Number of astrocyte Ca2+ events seen at the pre-capillary sphincter before multicompartment dilations in several experiments in WT (*open symbols*) and IP3R2KO (*solid symbols*) mice. *Black lines* are mean values. Separate comparisons for dilations starting at PA (*diamonds*), sphincter (*triangles*) or capillaries (*circles*). The number of pre-dilation Ca2+ events was significantly reduced in IP3R2KO vs. WT mice for dilations starting at PA or capillary, but not for dilations starting at the sphincter (Mann-Whitney test: WT vs KO: (a) dilations with origin at PA: $p = 0.0077$; (b) dilation with origin at sphincter: $p = 0.45$; (c) dilations with origin at capillary: $p=0.029$. Number of dilations/FOV analyzed with origin at PA, sphincter and capillary, respectively, was in WT: 116.1±24.7, 82.4±19.7 and 67.2±16.2 in N=20 FOVs in 6 mice. In IP3R2KO: 130.3±35.4, 76.9±21.9, and 50.9±14.3 in 14 FOVs in 4 mice.

D. Timing of the pre-dilation astrocyte Ca2+ events seen at the sphincter in the 2 sec preceding multicompartment dilations in WT and IP3R2KO mice (*open* and *solid symbols*, respectively). Events are evaluated with regard to the difference in onset time, but the number of earlier-onset events is also evaluated (EO, starting >1 before dilations start). Comparisons are performed separately for dilations starting at PA, sphincter or capillaries (*symbols* as in C). Despite their being no significant difference between the onset time of the events in wt and IP3R2KO, In IP3R2KO mice, EO events were significantly suppressed (*dashed grey circles*) for dilations starting at PA or capillary but not for dilations starting at the sphincter (Mann-Whitney test, WT vs KO: Dilations starting at (a) PA: onset time $p=0.71$, count of EO $p = 0.0049$; (b) at sphincter: onset time $p= 0.79$ count of EO $p = 0.18$; (c) at capillary: onset time $p=0.13$, EO $p = 0.0075$). The number of dilations/FOV analyzed with origin at PA, sphincter and capillary, respectively, were in WT: 116.1±24.7, 82.4±19.7, and 67.2±16.2 in 20 FOVs in 6 mice and in IP3R2KO: 130.3±35.4, 76.9±21.9 and 50.9±14.3 in N=14 FOVs in 4 mice.

E. Distance from the sphincter of the pre-dilation astrocyte Ca2+ events in the 2 sec preceding multicompartment dilations in WT and IP3R2KO mice (*open* and *solid symbols*, respectively). *Black lines* are mean values that are equal between groups. Thus, events were divided into those occurring at a shorter distance from the sphincter (SD, <5 µm) and those occurring at longer distances (LD, 5-20 µm). Comparisons are performed between WTvs IP3R2KO for dilations starting at PA, sphincter or capillaries (*symbols* as in C). SD events were significantly more suppressed (*dashed grey circles*) than LD ones for dilations starting at PA or capillary, but not for dilations starting at sphincter (Mann-Whitney test: WT vs KO: for dilations starting at (a) PA: SD $p = 0.0038$; LD $p=0.18$; (b) sphincter: SD $p = 0.52$, LD $p=0.18$; (c) capillary: SD $p = 0.023$, LD $p=0.15$). The number of dilations with origin at PA, sphincter and capillary, respectively, were: in WT: 116.1±24.7, 82.4±19.7 and 67.2±16.2 in 20 FOVs in 6 mice; in IP3R2KO: 130.3±35.4, 76.9±21.9 and 50.9±14.3 in 14 FOVs in 4 mice.

Spread of dilations across the sphincter is impeded in IP3R2KO mice.

We then wondered whether the lack of pre-dilation Ca2+ activity at the sphincter affected the vascular dilation patterns. Our first observation was that in IP3R2KO mice, the number of multicompartmental dilations decreased by 14% compared to those in WT mice (Sup. figure S9A), and the number of dilations involving only the capillary branch increased by 29% (Sup. figure S9A). In addition, fewer dilations arrived at the junction from outside the 3D-FOV, both from the PA and the capillary compartments (Figure 5) and proportionally more initiated at the sphincter or the bulb (Figure 5A). Similarly, if dilations involved just the capillary compartment, in IP3R2KO mice, fewer arrived from the capillary bed (Sup. figure S9B). On top of this, a lower fraction of the dilations arriving from the capillary compartments spread across the sphincter to the PA in the IP3R2KO mice (Figure 5B). We then investigated the time dilations took to spread from one compartment to the next, considering the three most common sites of dilation origin (Figure 5C). In WT mice, the spread of dilations from PA to capillary took, on average, 488 ± 18 ms, and, in the opposite direction, from capillary to PA, 667 ± 17 ms (Figure 5C). The speed of transition from PA to capillary was much faster (608 ± 57 µm/s) than from capillary to PA (112 ± 5 µm/s, Sup. figure S9C). In IP3R2KO mice, dilations arriving at the junction from the PA were, on average, 260 ms slower in engaging the capillary than in WT mice. Dilations with the opposite direction, arriving from the capillaries, were delayed by 140 ms in crossing the sphincter to the PA (Figure 5C, Sup. figure S9C). For the dilations that were initiated at the pre-capillary sphincter, spreading to the capillary was also delayed (by 110 ms) in IP3R2KO compared to WT mice (Figure 5C). The slower spread of the dilations in IP3R2KO mice was not due to structural differences of the PA and capillary or their average distance compared to WT mice (Sup. figure S9D).

The reduced spread between compartments in IP3R2KO mice was also seen in the dilations during movements (Sup. figure S10A-C). Some parameters were unchanged between WT and IPR2KO mice, such as the frequency (Sup. figure S10D) and total volume increase (Sup. figure S10E). However, as dilations in the resting IP3R2KO animals took longer to progress between vascular compartments, the total duration of the events was longer than in WT mice (Sup. figure S10F). The prolonged duration was not the cause of reduced spread, as the latter phenomenon was visible even upon plotting dilations as a function of their duration (Sup. figure S10G and H). Overall, in IP3R2KO mice, we found that both the pre-dilation Ca^{2+} activity in the astrocytic end-feet surrounding the sphincter and the speed and efficiency of the spread of dilations across the sphincter were reduced. The latter phenomenon may be the basis for the failed recruitment of neighboring vessel compartments.

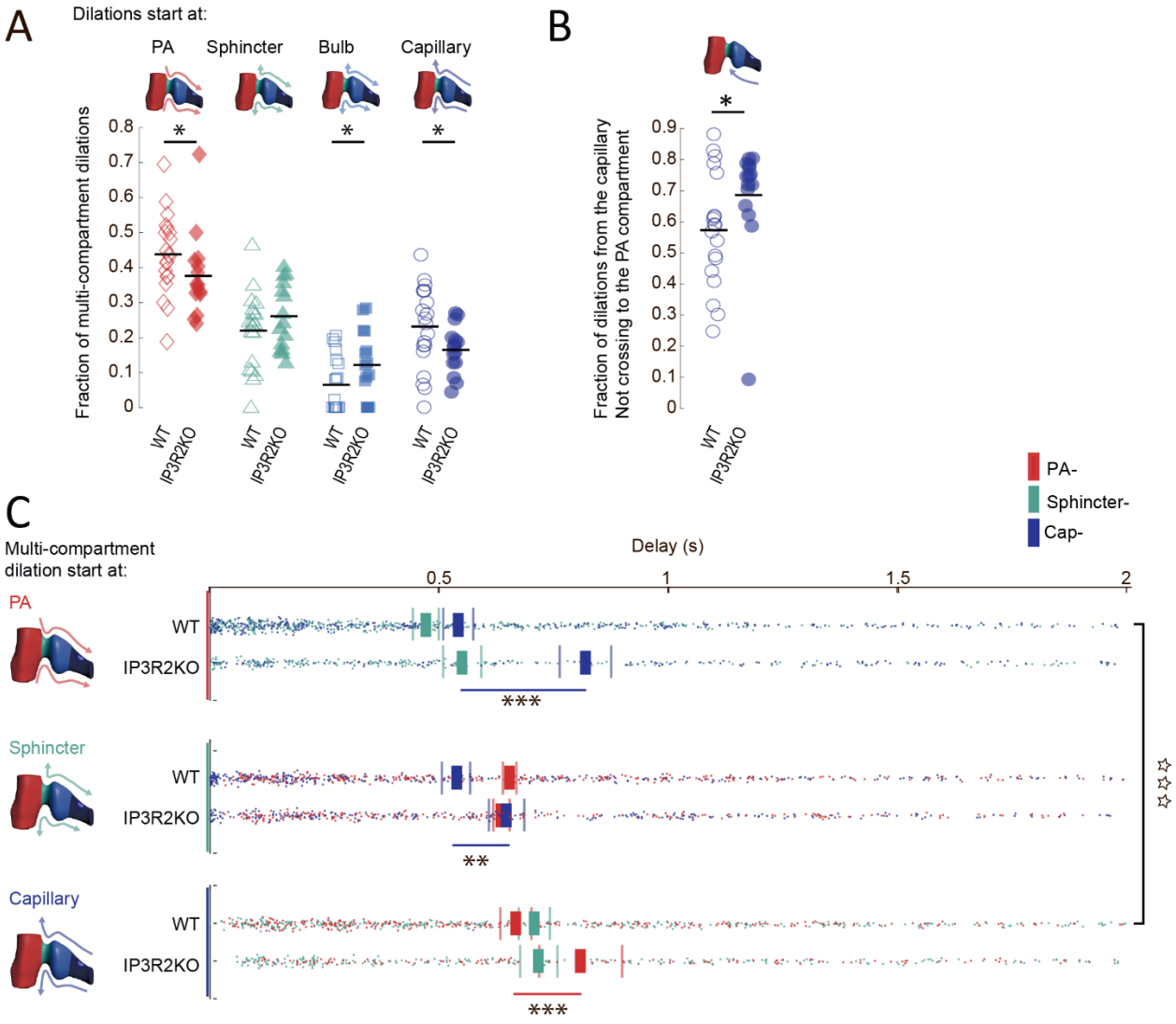

Figure 5. The spread of dilations from one vascular compartment to another is impaired in IP3R2KO mice.

A. Fraction of multicompartment dilations according to initiation site in WT and IP3R2KO mice. WT: *open symbols*; IP3R2KO: *solid symbols*. Dilations starting at PA: *red diamonds*; sphincter: *cyan triangles*; bulb, *light blue squares*; capillaries, *blue circles*. *Black lines* are mean values. In IP3R2KO mice, the fraction of multicompartment dilations starting at the PA or the capillary bed was reduced compared to WT mice (Mann-Whitney test: WT vs KO: dilations at PA: p = 0.017; at sphincter: p = 0.16; at bulb: p = 0.044; at capillary: p= 0.025). The number of dilations/FOV analyzed in WT was 82.65±20.13 in N=20 FOVs in 6 mice; in IP3R2KO, 75.27 ±16.73 in N=14 FOVs in 4 mice.

B. Characteristics of the dilations arriving from the capillary compartment in WT and IP3R2KO mice. WT: *blue open circles*; IP3R2KO: *blue solid circles*. *Black lines* are mean values. In IP3R2KO mice, a larger fraction of dilations did not cross the sphincter to become multicompartment than in WT mice (Mann-Whitney test, WT vs IP3R2KO; p = 0.027). Number of dilations/FOV analyzed: in WT: 166.84±30.41 in N=20 FOVs in 6 mice; in IP3R2KO: 176.2±41.24 in N=14 FOVs in 4 mice.

C. Timing of spread of multicompartment dilations between vessel segments in WT and IP3R2KO mice. Dilations are presented according to initiation segment (*top*: PA, *red*; *middle*: sphincter, *cyan*; *bottom*: capillary, *blue*). Color-coded dots along the x-axis mark the start time of dilation of a given vessel compartment, which is measured as a delay from the start time of the initiating compartment. The color-coded rectangles are the corresponding mean values, and the surrounding thin lines show the SEM. In WT mice (20 FOVs from 6 mice), dilations spread faster from PA to capillary than in the opposite direction, from capillary to PA (*Open stars* in vertical; Wilcoxon signed-rank test, $p = 4.4 \times 10^{-6}$; n = 366 dilations spreading from PA to capillary and 323 dilations from capillary to PA). In IP3R2KO mice, the spread of dilations across the sphincter was slower than in WT mice for dilations arriving from outside the FOV, regardless of the initiating compartment. Dilations starting at the sphincter were slower to reach the capillary (Mann-Whitney test; WT vs. KO: (a) initiation at PA and spread to sphincter: p=0.62; capillary: p = 0.0000048; n = 366 dilations in WT and 142 in IP3R2KO mice; (b) initiation at sphincter and spread to capillary: p = 0.0017; PA: p = 0.62; n = 329 dilations in WT and 239 in IP3R2KO mice; (c) initiation at capillary and spread to: PA: p = 0.0083; sphincter: p = 0.93; n= 323 dilations in WT and 145 in IP3R2KO mice. Data from 20 FOVs in 6 WT mice and from 14 FOVs in 4 IP3R2KO mice.

Dilations and local astrocytic Ca2+ activity evoked by auditory stimulations resemble those occurring naturally in resting mice.

All our investigations so far were on dilations occurring naturally in the resting animal. By focusing on the resting condition, we excluded contributions to dilations by movement/arousal-induced mechanisms. However, we did not directly demonstrate that the observed vascular responses are part of NVC or exclude the influence of other factors unrelated to the local neuronal activation generated by sound perception (Kameyama et al., 2008). To address this issue, we induced vascular responses via direct auditory stimulation and compared their properties with those of the "natural" dilations. The auditory cortex is formed by zones that gradually change sensitivity to different pitches (Tsukano et al., 2015). Therefore, we tested several tones and used intrinsic optical signaling (IOS) detection to determine which tonalities would appropriately stimulate the cortical region exposed in the craniotomy. With the IOS, we could also establish rough tonality maps of where, in a given cortical area, the tone frequencies activated the maximum blood flow increase (Figure 6A). We then compared 10-sec-long tone stimulations and the associated IOS-blood flow responses (IOS maps) with the local dilations seen at PA-capillary junctions under two-photon imaging (Figure 6A-B). For this, we used a combination of three tones that we expected would trigger a response in at least one region of our cranial window. To initially correlate wide-field IOS maps with regulations at individual vessel levels, we investigated four PA-junctions in one preparation of the auditory cortex. We sampled individual vessel responses in parallel at these four branch points, one in layer I and three in layer II/III, on three PAs entering the tissue at different auditory cortex locations. The dilations that we saw at these junctions differed in origin and directionality. Still, their duration always reflected the strength of the IOS signal detected in the same area: longer-lasting dilations were associated with tones producing strong local IOS responses, and shorter-lasting ones to tones producing weak IOS responses (Figure 6B). Noteworthy, the junction in layer I showed less tone specificity than those in layer II/III, possibly reflecting a less restrictive flow pattern in superficial layers than in the deeper layers

downstream. Most of our auditory preparations were investigated at fewer locations, so in order to extend the study to all, we made a generalized classification based on the individual IOS maps. In this way, we tried to link specific dilation patterns at PA-capillary junctions to the strength of the tone-evoked IOS responses. We did this by considering the position of the entrance of the PA in the cortex relative to the IOS map, i.e., whether its path and the related PA-capillary junction were at the center of the IOS map or displaced from it (Figure 6C). We found that most of the tones induced IOS responses somewhere in our cranial window, but not all these responses were centered on the region where a PA entered the cortex. When a tone induced a strong IOS response in the area of a junction (Figure 6C left), most of the dilations were long-lasting and quickly progressed across the pre-capillary sphincter to become multicompartment, independent if they began at the capillary or the PA. In cases when the junction area was not at the center of the tone-evoked IOS response, we could still observe dilations in our 3D-FOV, but they mostly arrived from the capillaries (rarely from the PA) or originated at the sphincter (Figure 6C right). Tone-induced dilations varied in duration, ranging from >60 seconds to <1 sec. When the junction area was located at the center of the IOS response, all were >5 s-long and showed a capacity to progress beyond the sphincter that was proportional to the duration of the dilation. The shortest ones were mainly restricted to the capillary bed. In contrast, the longest ones always propagated to all compartments (Sup. figure S11B), resembling the "natural" dilations in the resting animal (Figure 2). Moreover, the proportion of tone-evoked dilations starting respectively upstream, downstream, or at the sphincter was analogous to that of the "natural" dilations (Sup. figure S11C). These observations strengthen the case that naturally occurring dilations in the resting animal directly reflect the auditory experience and represent the associated NVC response.

As a next step, we investigated whether tone-evoked dilations, like "natural" dilations, were preceded by local astrocyte end-foot Ca^{2+} activity. For this, we used the same unbiased automated approach used for extracting the Ca2+ dynamics preceding "natural" dilations (Figure 3). In this investigation, the much lower number of dilations made our inclusion criterion less permissive(Sup. figure S6). Despite this, we could still consistently identify pre-dilation Ca2+ signals, which preponderantly occurred at the pre-capillary sphincter (Figure 6D, Sup. figure S11D).

The tone-evoked Ca2+ responses in astrocytes and blood vessel dilations are affected in IP3R2KO mice.

To directly address the impact of the local astrocyte Ca2+ activity on the progression of tone-evoked dilations, we repeated experiments in IP3R2KO mice. In WT mice, the large majority (79%) of the dilations arriving from either the PA or the capillary compartments were preceded by an astrocytic Ca2+ activity at the sphincter. This proportion decreased to 48% in IP3R2KO mice, and we identified fewer pre-dilation events (Figure 6E). As for the spontaneous dilations, the fraction of dilations that could not cross the sphincter and remained confined to the capillary bed was more than twice that in WT mice (28.7 ± 10.8% vs. 13.2 ± 7.4% in WT, Figure 6F). In complement, we observed that the progression of tone-evoked dilations across the sphincter was slowed down. Dilations arriving from the PA were delayed in reaching the capillary by 416 ± 145ms. Dilations from the capillary bed were also delayed, mostly in recruiting the sphincter, by 376 ±208ms, while an additional 91 ± 266ms delay reaching the PA was not statistically significant (Figure 6G). We conclude that IP3R2 deletion has a clear negative impact on tone-evoked dilations. Its effect is in many parameters similar to the one seen in naturally occurring dilations. These

data indicate that by their local Ca2+ activity at the sphincter, astrocytes act as physiological regulators of the spreading of dilations between vascular compartments as part of the NVC response to auditory stimulation.

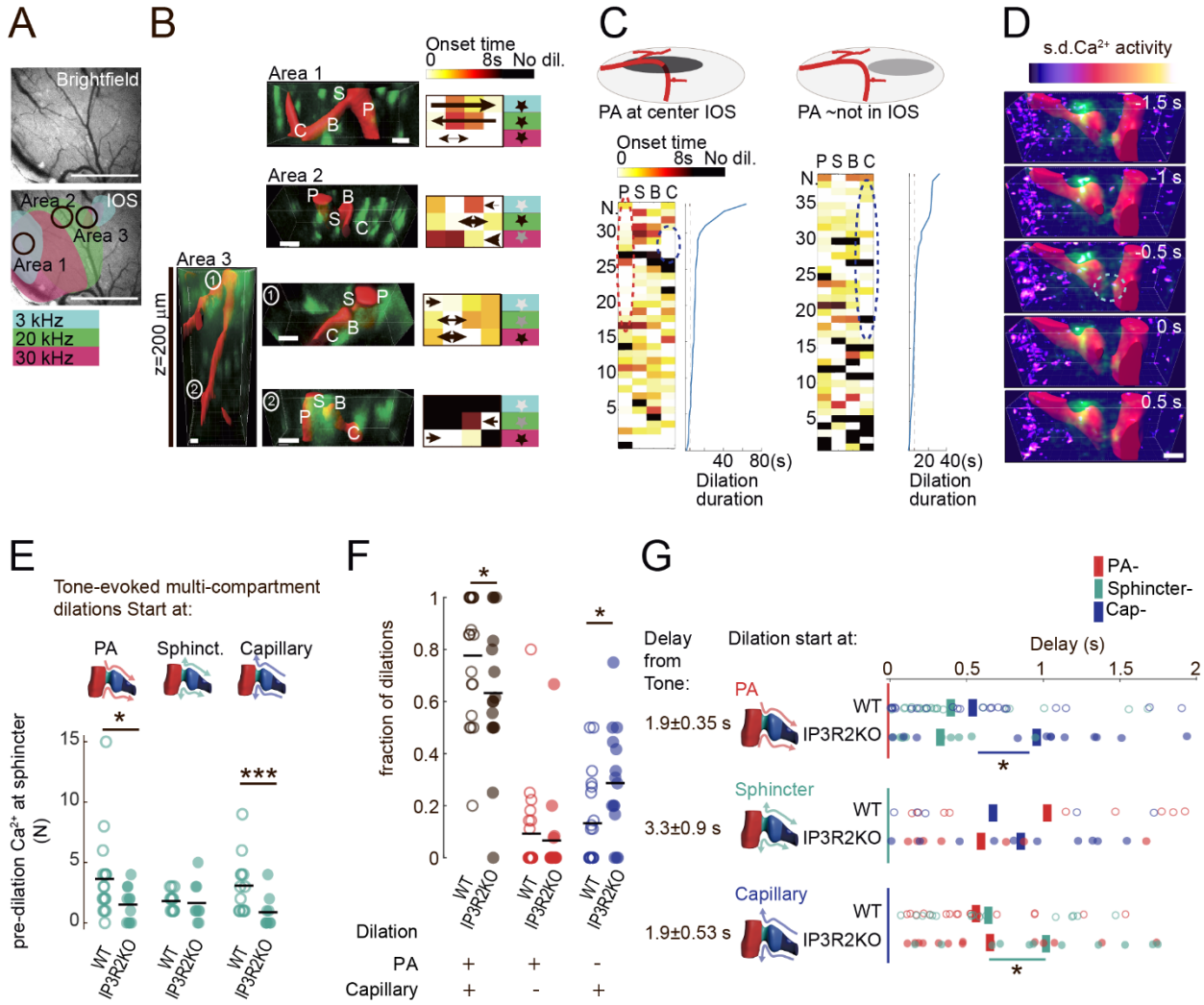

Figure 6. Pre-dilation astrocytic Ca^{2+} activity at the sphincter and dilation patterns after auditory stimulations resemble naturally occurring NVC responses and are similarly altered in IP3R2KO mice.

A. *Top*: Brightfield image of the brain surface in a chronic craniotomy at the level of the auditory cortex. *Bottom*: Intrinsic optical signal (IOS)-based map of the tonality in the same auditory cortex region, with an overlay of three colors, each one marking the response pattern to the stimulation of the corresponding tonality (*azure*: 3kHz; *green*: 20 kHz; *red*: 30 kHz). The map shows that the three tone frequencies activate distinct but partly overlapping regions. Black circles identify the areas where three PAs enter the tissue (see panel B). Scale bar: 1mm.

B. Representative dilations at PA-1st order capillary junctions in response to tone stimulations. Recordings are from 4 3D-FOVs in the 3 auditory cortex areas shown with circles in panel A. *Left*: images show vascular and astrocytic structures in the 4 3D-FOVs in the 3 areas and are cumulative averages of 2 minutes 3D timeseries; in *red*: Texas red-dextran masked signal highlighting vessel

lumen; in *green*: astrocyte GCaMP6f signal highlighting the active perivascular end-feet. The 3D-FOVs in Areas 1 and 2 each contain a single pre-capillary junction showing the branching of the capillary from the PA at the level of layer II/III (170-200 µm and 177-202 µm below the cortical surface, respectively). The 3D-FOV in Area 3 contains 2 junctions (circled 1 and 2, respectively): the upper one in layer I (1, 64-86 µm below surface), and the other in layer II/III (2, 194-216 µm below surface). The different vascular sections are marked P: PA, S: Sphincter, B: Bulb, C: Capillary. *Right*: schematic representation of dilations evoked by tones of different frequencies (color-coded as in panel A). The timing of individual vessel segment dilation is depicted on a white-to-dark-red temporal scale (black indicates no dilation). The direction and duration of the dilations are schematized by the direction and thickness of the arrows, respectively (longer duration = thicker arrow). The position of the PA with respect to the IOS response evoked by a given tone frequency stimulation is summarized by color-coded stars: *black*, PA at the center of the IOS response; *grey*, PA at the border of the IOS response; *light grey*, PA further away from the IOS border. The length of the dilations correlated with the tone frequency that elicited the strongest IOS response in the specific 3D-FOV. Vessel dilation durations: Area 1: 3kHz stimulation: 40.7s; 20kHz: 15.4s; 30kHz: 3s. Area 2: 3kHz: 3.5s; 20kHz: 25.5s; 30kHz: 7.2s. Area 3, upper junction 1: 3kHz: 13.5s; 20kHz: 6.5s; 30kHz: 63.8s; lower junction 2: 3kHz: no dilation; 20kHz: 12.4s; 30kHz: 10.3s. The junction in layer I showed less tone specificity than the three junctions in layer II/III. Scale bars: 10µm.

C. Dilation patterns were observed in the average responses to different tones in all the 3D-FOVs included in this study (n = 73 tone responses in 20 FOVs in 6 mice). *Left:* patterns associated with tones that evoked a strong IOS response around the PA; *right:* patterns associated with tones that evoked weak or no IOS response around the PA. Dilation responses are ordered according to their duration (*blue plots* on the right of each column), from bottom (shortest) to top (longest). Timing of dilation of individual vessel compartments is represented in white-to-dark-red temporal scale as in panel B. The different vascular sections are marked P: PA, S: Sphincter, B: Bulb, C: Capillary. Dilations with the longest duration were evoked by tone stimulations with IOS response centered around the PA (*left*). They began at either the capillary (*blue dotted line circle*) or PA (*black dotted line circle*) and quickly progressed across the sphincter. In contrast, short dilations were evoked in areas with approximately no IOS response and often did not involve all compartments (*right*). Those involving all compartments mostly originated from the capillary (*blue dotted line circle*).

D. Representative time-series of pre-dilation astrocytic Ca2+ activity associated with tone-evoked multicompartment dilations. The 3D-FOV, x= 75.5µm, y= 23.6µm, goes from 194 to 216 µm below the brain surface. Images are from 1.5 seconds before the spread of a multicompartment dilation from the PA to 0.5 seconds after its start. *Red*: Texas red-dextran masked signal highlights vessel lumen; *green*: cumulative astrocyte GCaMP6f signal highlights active perivascular end-feet. *Pseudocolor*: Normalized astrocytic Ca2+ activity. *Dotted line circle* shows astrocytic Ca2+ activity at the sphincter prior to dilation onset. Scale bar: 10µm.

E. Number of pre-dilation astrocyte end-foot Ca2+ activities seen at the sphincter before tone-evoked multicompartment dilations in WT and IP3R2KO. WT: *cyan, open circles*; IP3R2KO: *cyan, solid circles*. *Black lines* are mean values. Comparisons are presented in separate columns according to the site of origination of the dilation. The number of pre-dilation Ca2+ signals was

significantly reduced in IP3R2KO compared to WT mice for dilations that began either upstream (PA) or downstream (capillary) the sphincter (Mann-Whitney test: WT vs. KO: dilation starting at PA: p = 0.026; capillary: p=0.0046) but not for those initiated at the sphincter (WT vs KO: p = 0.22). Number of dilations/FOV starting at PA, sphincter, and capillary, respectively, in WT, were: 1.98±0.62, 0.85±0.38, and 1.25±0.58, from N=20 FOVs in 6 mice. In IP3R2KO: 1.4±0.68, 1.3±0.83, and 1.13±0.63 from N=14 FOVs in 4 mice.

F. Fraction of multicompartment and single compartment dilations evoked by auditory stimulations in WT and IP3R2KO mice. WT: *open circles*; IP3R2KO: *solid circles*. *Black lines* are mean values. Analysis is restricted to dilations lasting >5 sec, i.e., the response group containing multicompartment dilations. Comparisons are presented for the ensemble of multicompartment dilations (*black circles*), and separately for single-compartment ones that involved the PA (*red circles*) or the capillary (*blue circles*). Multicompartment dilations were significantly reduced in IP3R2KO mice, whereas single compartment dilations confined to the capillary were increased (Mann-Whitney test: WT vs KO: multicompartment dilations: p = 0.049; single compartment involving the PA p=0.52 and the capillary: p = 0.012). The number of dilations/FOV analyzed in WT was 7.55±1.79 in N=20 FOVs in 6 mice. In IP3R2KO: 9.67±2.52 in N=14 FOVs in 4 mice.

G. Temporal progression of tone-induced multicompartment dilations arriving from outside the FOV in WT and IP3R2KO mice. WT: *open circles*; IP3R2KO: *solid circles*. Representation as detailed in Fig. 5C, according to starting compartment: *red*, PA; *cyan*, sphincter; *blue*, capillary. Data are normalized to the arrival of the dilation in the FOV, but the average start point after the tone stimulation for each compartment is reported on the y-axis. The Spread of the dilations to and across the sphincter was delayed in IP3R2KO mice. The recruitment of the PA from the capillary is less than in spontaneous dilations (Kruskal Wallis followed by Mann-Whitney test; WT vs KO: (a) for dilations starting at PA: onset time at sphincter p = 0.55; at capillary p =0.019. N= 43 dilations in WT and 21 dilations in IP3R2KO; (b) for dilations starting at sphincter: onset time at PA p=0.82; at capillary p=0.37. N= 17 dilations in WT and 20 dilations in IP3R2KO; (c) for dilations starting at capillary: onset time at sphincter: p = 0.032; at PA: p = 0.19. N= 29 dilations in WT and 17 dilations in IP3R2KO. Data from 20 FOV in 6 WT mice and form 14 FOV in 4 IP3R2KO mice.

Discussion

In this study, we revealed a new role for astrocytes in neurovascular coupling in the auditory cortex, notably as regulators of the spread of dilations between the PA and capillary compartments in response to sound perception. We found that the astrocyte control is exerted via focal Ca2+ elevations occurring specifically at the pre-capillary sphincters connecting the two compartments. Such local astrocyte activity, impaired in IP3R2KO mice, precedes the arrival of dilations at the sphincters and, by controlling their contractility, determines how much and how far blood is distributed during cortical activation. We could obtain this information thanks to an unconventional two-photon imaging approach in the awake mouse, in which we combined volumetric recording of a large FOV, comprising both the PA and capillary compartments and the connecting junction, to fast acquisitions of vascular and astrocyte Ca2+ dynamics. By centering our 3D-FOV on the vascular tree and the associated astrocytic end-feet and peri-vascular regions, we could capture even the most transient local Ca2+ activities and their interplay with the vascular dilations throughout the imaged vascular tracts. Only a minority of the preceding studies were

performed in the awake mouse, and none used fast volumetric imaging. This approach enabled us not only to study all the natural dilation patterns occurring in a behaving mouse but also, in most cases, to establish their origin, directionality, and level of progression between imaged compartments, revealing a previously unappreciated complexity. This methodological advance overcomes several of the shortcuts that affected previous work and likely contributed to the multi-year controversies about the role (or not) of astrocytes and their Ca2+ dynamics in NVC that we summarized in the Introduction section. It also enabled us to revisit the few recent studies performed in the awake mouse (Del Franco et al., 2022; Institoris et al., 2022; Ozawa et al., 2023; Renden, Institoris, Sharma, & Tran, 2024; Tran et al., 2018) and complement their findings, providing a more comprehensive picture. Among others, we could here dissociate components of the natural vascular responses, and related astrocyte Ca2+ signals, that depend on the activity state of the mouse during locomotion and arousal from those evoked by sound perception. The latter was seen in isolation when the animal was at rest and showed a strong analogy to the responses evoked by natural tone stimulations, indicating that they are directly induced by the sensory experience and likely represent the physiological NVC response to auditory activation.

The dilation patterns that we observed here differ significantly from those reported previously in anesthetized mice. In the latter, hemodynamic responses correlate less to neural activity (C. Chen et al., 2021) and are quite stereotyped (Cai et al., 2018; Hall et al., 2014). In our naturally behaving mice, dilation patterns were highly heterogeneous. They incorporated contextual contributions from the animal's brain state or inputs from other cortical areas, such as the motor cortex. During our recordings, mice moved and underwent arousals, activities associated with large astrocytic Ca2+ events not seen in anesthetized mice (Bindocci et al., 2017). Such large astrocytic Ca2+ elevations were reminiscent of those recently shown to prolong the duration of PA dilations during sustained whisker stimulation in the barrel cortex of awake mice (Institoris et al., 2022). We found that during arousals, more dilations spread across the pre-capillary sphincters than in the resting mouse, suggesting that the associated bursts of astrocytic Ca2+ activity might function to ensure an abundance of blood flow to the tissue in the aroused state, keeping the neurons metabolically prepared to handle additional auditory stimulations.

An important advantage of our volumetric imaging approach was its ability to follow the spatial and temporal dynamics of dilations more comprehensively than in past studies. Thereby, we could define sites of origin and direction of the dilations as they progressed along the different vascular compartments. This approach was instrumental in discovering the central regulatory role of the pre-capillary sphincters, which was difficult to appreciate in previous work in which dilations were imaged separately at either the capillary or the PA level. It was similarly necessary to identify the presence of an associated local astrocyte Ca2+ activity that preceded the passage of dilations from the sphincters.

The spatial dynamics of dilations were also investigated in previous work, but without reaching firm conclusions about their origination. Most of those studies were performed in anesthetized mice in which dilations had to be evoked, and authors reported initiations either at lower cortical levels (Tian et al., 2010) triggered by activity along the capillaries (Cai et al., 2018; Hartmann et al., 2022; Rungta et al., 2018; Wei et al., 2016), or at upper levels, with the recruitment of the PA from the surface arteries (B. R. Chen, Kozberg, Bouchard, Shaik, & Hillman, 2014; O'Herron et al., 2016). This diversity might reflect the different methods used in different studies for evoking the dilatory responses (Rungta et al., 2021) and the fact that

a blood flow increase can be initiated at any cortical lamina in which the response is elicited (Fabricius, Akgoren, Dirnagl, & Lauritzen, 1997). In our study focusing on the PA-capillary junctions in awake mice, the observed variety in dilation originations occurred naturally. We could capture the specific directionality of these natural dilations as they arrived from either capillary, PA, or initiated at the junction level, thanks to the simultaneous fast imaging of all these compartments. Interestingly, a similar variety of originations was recently described in the barrel cortex of awake mice (Rungta et al., 2021). This is not surprising because the two regions are similarly organized for blood flow regulation, with analogous densities of branching vessels (Kirst et al., 2020), relays in the neuronal circuits, and projections from other cortical areas (Kral, Yusuf, & Land, 2017). Brain regions with simpler organization display more stereotyped blood flow responses (Kornfield & Newman, 2014; Rungta et al., 2018). The different positions at which the naturally occurring dilations originated in the auditory cortex must depend on differences in the modes by which blood flow regulation is recruited. The mode, in turn, stems from the large diversity in the neuronal circuit relays that can project the sensory stimuli to the processing cortical region (De Franceschi & Barkat, 2021; Duque, Pais, & Malmierca, 2018; Szymanski, Rabinowitz, Magri, Panzeri, & Schnupp, 2011). In our analysis of tone-evoked dilations, we propose a classification based on the positioning of the dilations relative to the IOS response, which we considered to represent the core of the neuronal excitation. When the latter coincided with the area supplied by the PA, the neuronal origin of the dilation would be along the PA inflow tract, but when the IOS response was in the vicinity and not exactly at the PA, the neuronal excitation would trigger the dilation further down the vascular tree, around the capillary compartment (Figure 7a). Albeit roughly reliable, the above classification may still not fully grasp the complexity of the dilation patterns that we observed, and other contributory factors need to be considered. For example, the more articulated nature of the tonotopy compared to the IOS map, given its heterogeneity at the cellular level (Bandyopadhyay, Shamma, & Kanold, 2010; Issa et al., 2014) which implies a diversity of neuronal activation patterns capable of triggering the NVC response. In addition, the higher complexity of the natural sounds that induce the natural vascular responses compared to the tones that we used to evoke them. Complex sounds often trigger tonotopic neuron responses in different fields of the auditory cortex in parallel (Solyga & Barkat, 2022).

In addition to describing the varied origin of natural dilations in awake mice, we here describe, for the first time, the central role of the pre-capillary sphincters in determining by which extent these natural dilations spread between PA and capillary compartments under local control by astrocyte Ca2+ signaling. Pre-capillary sphincters have been anatomically well characterized only in recent years and only in the somatosensory cortex (Grubb et al., 2020). They have been described as a hemodynamic structural division between capillary and arterial blood flow, acting as a bottleneck opposing high resistance to blood flow (Grubb et al., 2021). In view of the strategic interposition between PA and capillaries in the upper cortical layers, under baseline conditions, sphincters would protect capillaries from high arterial pressures. They do not provide, however, only passive flow resistance but can also actively contract thanks to α-smooth muscle actin expressed in their mural cells. Experiments in anesthetized mice have shown that they undergo significant diameter changes upon whisker stimulation (Grubb et al., 2020) or vasoactive agent infusion (Zambach et al., 2021), hinting at a potential role in blood flow regulation during endogenous functional stimulation. Here, we provide the first direct evidence of this physiological role during the auditory NVC response. Due to the unique strategic placement at PA branching points, pre-

capillary sphincters can control blood supply to larger domains than the downstream contractile capillary pericytes. Thus, a single PA connects to various capillaries that branch out and supply blood flow to distinct sensory areas (O'Herron et al., 2016; Wu et al., 2016). Flow regulation at this branching point can optimize blood delivery in register with neural activity (Angleys, Jespersen, & Ostergaard, 2018; Gutierrez-Jimenez et al., 2016) and may well be the basis of the laminar activation pattern observed in human fMRI brain imaging (Egbert, Lojek, Biswal, Pluta, & Harmonia, 2021). On the other hand, the spread of dilations up-stream, from the capillaries to the PA (Cai et al., 2019; Rungta et al., 2018), is equally important for pairing increased local demands to global activation and likely contributes to the accurate and sufficient blood distribution essential for optimal brain function and health (Hartmann et al., 2022; Ostergaard, 2020). The upstream-directed regulation apparently depends on endothelial K+ signaling (Longden et al., 2017) and can be elicited by stimulating TRPA1 or KIR channels directly on 1st and higher-order capillaries (Thakore et al., 2021). Moreover, this critical regulation is supported by another level of regulation with a similar upstream direction that occurs at higher-order capillary branch points (Gonzales et al., 2020).

While all the above observations align with our current results, they have provided only a fragmentary picture of the NVC-related dilation dynamics. Thanks to our 3D imaging approach and the large number of natural dilations that we recorded, we were able to put pieces together. Based on this information, we propose the following interpretation of the observed dilation patterns: dilations arriving from the PA compartment may or may not involve the capillaries. The main factor determining their spread beyond the pre-capillary sphincter and the blood delivery to the downstream capillary bed is most likely the position where the neuronal activation driving the NVC response occurs (Figure 7b). If it localizes primarily to the deeper cortical layers at the layer II/III junction, the dilation generally involves only the PA. However, if the activation and its metabolic needs also concern the upper cortical lamina, the downstream capillary region receives additional local blood flow via expansion of the sphincter and 1st order capillary. Likewise, local neuronal activation can trigger dilations that initiate at the 1st order capillary (Hartmann et al., 2022; Rungta et al., 2018) and only involve the capillary branches or be part of a larger neuronal response. In the latter case, the activation recruits additional blood from the surface vessels by spreading across the sphincter to increase delivery via the PA (Figure 7b).

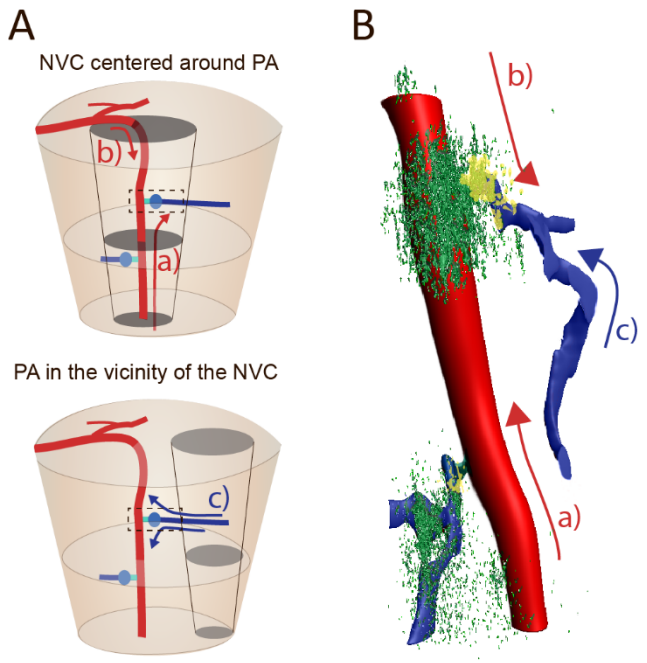

Figure 7. Schematic representation of the mode of progression of vascular dilations at upper cortical junctions under the control of astrocyte Ca2+ activity.

A. Origin and direction of dilations at any given PA-capillary junction with respect to areas of excitation. *Top*: when excitation (*grey region*) occurs exactly in the cortical area around the PA (*red*), the NVC (a) is initiated in the layers below by excitation of layer IV-VI neurons or (b) arrives from the surface vessels due to widespread excitation. Either way, the dilation is perceived to arrive at the junction (*dashed-line rectangle*) from the PA (*red arrow*) in the upper cortical layers. *Bottom*: when excitation (*grey region*) occurs in a region close but not coincident to the area supplied by the PA (*red*), the dilatory response arrives at the junction (*dashed-line rectangle*) from the capillary compartment (c, *blue arrow*) and will first recruit either the capillary (*blue*) or the pre-capillary sphincter (*cyan*) in the dilation.
B. Illustration of how astrocyte Ca2+ activities at strategic locations regulate the spread of dilations across the sphincter between the PA and the 1st order capillary. Astrocytes (*green*) regulate the progression of dilations with local and short-lasting Ca2+ activities in the end-feet enwrapping the pre-capillary sphincter (*yellow*). This regulation occurs when dilations arrive from deeper cortical layers (a, *red arrow*), from increased blood flow from surface arteries (b, *red arrow),* or from activity downstream in the arbor along the capillary (c, *blue arrow*), as detailed in panel A. We observed pre-dilatory Ca2+ elevations in astrocyte end-feet also for dilations initiated at the sphincter. Still, we did not find conclusive evidence that they exerted a regulatory role as dilations were apparently not affected in IP3R2KO mice.

Our study is also the first to describe a physiological regulatory role of astrocytic Ca2+ activity on the spread of dilations at the pre-capillary sphincters. This conclusion is supported by the observation that

IP3R2KO mice, which lack a large part of the astrocyte Ca^{2+} signaling, display an altered NVC response, specifically a reduced capacity of dilations to engage vascular compartments across the sphincters. Several past studies rejected an astrocytic contribution to NVC (Bonder & McCarthy, 2014; Del Franco et al., 2022; Nizar et al., 2013) because they failed to observe any changes in the blood flow responses in IP3R2KO mice. Among them is the recent study by Del Franco et al. (2022), albeit performed in awake mice and considering multiple compartments, from PA to 4th order capillaries. We, too, found parameters of the dilation patterns that were unchanged in the IP3R2KO mice. We need to highlight, however, that the study by Del Franco et al. differs in important aspects from ours': first, the authors did not image all the vessel compartments at the junction simultaneously; second, they did not consider the pre-capillary sphincter region in their analysis, nor the site of origin of the dilations; third, they evoked dilations by stimulations that elicited in astrocytes widespread Ca2+ elevations not directly comparable to the local Ca2+ elevations that we found precede naturally occurring dilations, and finally they did not image the dilations along the z-axis. Given these key differences, the results by Del Franco et al. (2022) are difficult to compare to ours. We could identify vascular abnormalities in IP3R2KO mice because we focused on an aspect never investigated before, namely the progression of dilations across the sphincter. This led to a twofold discovery: first, the recognition of the pre-capillary sphincter as a locus of physiological blood flow regulation, and second, the identification of a local astrocyte IP3R2-dependent Ca2+ activity controlling the sphincter's contractility.

When considered collectively, astrocyte Ca^{2+} activity is highly complex and involves a panoply of signals whose functional roles often remain enigmatic (Bindocci et al., 2017; Volterra, Liaudet, & Savtchouk, 2014). Such signals go from highly visible, spatially large, and temporally long Ca2+ elevations to more elusive, local, and fast Ca2+ transients. Importantly, Ca2+ signals relevant to synaptic activity were identified as part of the local transients occurring at the level of peri-synaptic processes (Arizono et al., 2020; Bindocci et al., 2017; Di Castro et al., 2011; Panatier et al., 2011). Therefore, vascular-relevant signals are logically expected to occur at astrocytic end-feet. However, even restricting the focus to end-feet, these structures display a multiplicity of Ca2+ signals with possibly different functions (Haidey et al., 2021; Institoris et al., 2022; Stobart, Ferrari, Barrett, Stobart, et al., 2018). Thus, when the aim is to identify potential regulatory signals, where and how the imaging is performed and how the extra blood flow is experimentally recruited are of critical importance. We used high-speed 3D imaging and focused on natural vascular changes at the pre-capillary sphincters, which regulate blood flow to a specific cortical lamina. Since this approach had not been attempted before, we did not apply strict criteria for defining the relevant astrocyte Ca2+ activity but just considered that such activity should (a) occur in the end-feet within a short distance from the vessel surface, (b) be time correlated to the dilations, and (c) appear at any dilation with a given pattern. We classified dilation patterns according to the site of origin and capacity to cross the sphincter. As discussed, such parameters reflect different types and loci of neuronal activation and suggest that the related astrocytic Ca2+ activities should also be diverse. Indeed, we observed pre-dilation end-foot Ca2+ responses with different onset times and positions along the PA-capillary junction. This heterogeneity is probably also fueled by the existence of anatomical differences in the junction-astrocyte contact points and by the incorrect calculation of onset times, when dilations originate outside the 3D-FOV. Nonetheless, our "loose" analytical approach was strong enough to identify NVC-relevant astrocyte Ca2+ activity, particularly because we sampled only physiological vascular events induced by

auditory perception, either occurring naturally during resting states of the mouse or evoked by natural sounds in the awake animal. The parallel reduction that we observed in the frequency of local astrocytic Ca2+ transients and of dilations that progressed across the sphincter in IP3R2KO mice supports the relevance of the identified astrocytic Ca2+ activity to the NVC auditory response.

In this study, we did not identify the mechanism responsible for the relevant local Ca2+ activity in astrocyte end-feet and the subsequent changed sphincter responsivity. For example, is the astrocyte Ca2+ elevation secondary to neuronal activation and synaptic transmission (Arizono et al., 2020; Bindocci et al., 2017) or not or only in part? Does it also depend on brain state and noradrenaline levels (Ding et al., 2013; Reitman et al., 2023)? Many different synaptic mechanisms have been shown to lead to Ca2+ increase in astrocytes (Mishra, Gordon, MacVicar, & Newman, 2024), including activation of Gq-GPCRs associated with IP3R2-dependent signaling such as mGluR5 or P2Y1R (Di Castro et al., 2011; Lind et al., 2013; Petzold et al., 2008), or of ionotropic receptors such as P2X1 and P2X5 (Bazargani & Attwell, 2016; Mishra et al., 2016). Alternative sources could be astrocyte plasma membrane Ca2+ channels such as TRPA1 (Shigetomi, Jackson-Weaver, Huckstepp, O'Dell, & Khakh, 2013) or TRPV4 (Diaz, Kim, Brands, & Filosa, 2019), or the Na+/Ca2+ exchanger following neurotransmitter uptake (Brazhe, Verisokin, Verveyko, & Postnov, 2018). TRPA1 channels could also be activated in endothelial cells (Thakore et al., 2021) and, in turn, trigger K+ release onto the astrocytic end-feet and initiate the local astrocytic Ca2+ response.

Another aspect that needs to be clarified is the relation between the local astrocytic Ca2+ responses that we identified mainly at the sphincter and the larger, spreading Ca2+ events occupying multiple end-feet. In other words, how exactly is the NVC influenced by changing brain states with activation of secondary pathways or neuromodulator effects that overlap with the primary auditory excitation (Eyre et al., 2022; Shimaoka, Harris, & Carandini, 2018)? This relation may hold the key to a more comprehensive understanding of how astrocytes contribute to keeping healthy and adequate levels of substrate and oxygen in the brain. In view of this, the fact that in the course of several CNS diseases, astrocytes undergo morphological changes leading to alteration or loss of the end-feet contact with the blood vessels surface (Khakh & Sofroniew, 2015), likely implies that the regulatory functions here identified will be impaired, contributing to the disturbed blood flow seen in such pathologies (Iadecola, 2017) notably in those accompanied by cognitive decline (Vestergaard et al., 2022). While our study leaves important open questions, we believe that the identification of the peculiar control exerted by astrocytes at the sphincter, a critical point of blood flow regulation in the vascular tree, significantly advances our understanding of the astrocytic contribution to NVC.

Materials and Methods

Animals

Most experiments in this study utilized mice induced to genetically express the Ca2+ sensitive indicator GCaMP6f selectively in the cytosol of astrocytes based on the GFAP promotor. This was obtained by crossing two transgenic mouse lines, a lox-STOP- lox-cytosolic-GCaMP6f (purchased from The Jackson Laboratory http://www.jax.org, JAX 024105 (*B6;-Gt(ROSA)26Sortm95.1(CAG-GCaMP6f)Hze/J*), and *hGFAPCreERT2* mice (Hirrlinger, Scheller, Braun, Hirrlinger, & Kirchhoff, 2006) obtained from Prof. F. Kirchhoff, University of Saarland, Germany, as previously described(Bindocci et al., 2017). A subgroup of these GFAPCreERT2xGCAMP6f mice was then crossed with the *Itpr2KO* mouse strain that carries a constitutive deletion of IP3 receptor type-2 (IP3R2) expressed in the ER and displays conspicuous reduction in astrocytic Ca^{2+} activity (Bonder & McCarthy, 2014). We used only IP3R2 ko/ko homozygotes in this study. Though IP3R2 contributes largely to astrocytic Ca^{2+} activity, especially in Ca^{2+} mediated Ca2+ release from the ER, not all Ca^{2+} activities depend on this receptor, and only the largest are abolished in the knockout (Sherwood, Arizono, Panatier, Mikoshiba, & Oliet, 2021). The mice were treated with Tamoxifen at 8 weeks of age to induce *Cre* recombination and trigger GCaMP6f expression in astrocytes. Tamoxifen (Sigma-Aldrich) was dissolved in corn oil (10mg/ml) and administered i.p. (0.1 ml/10 g body weight/day) for 5 days prior to the chronic cranial window surgery. The mice had surgery when they were 8 weeks old and, after a 4-week period of recovery and training, were included in the experiments between 12-28 weeks of age. Two 12-16 weeks-old GFAP-EGFP mice (Nolte et al., 2001) were used for morphological investigations. All experiments and procedures were conducted under license and according to regulations of the Cantonal Veterinary Offices of Vaud (Switzerland).

Chronic cranial window preparation

Chronic cranial windows were established as previously described (Bindocci et al., 2017). To target the auditory cortex, it was (centered around -3mm anterior-posterior (AP) and 5 mm mediolateral (ML) from bregma, right hemisphere). The surgical procedure was done under isoflurane 1.5% anesthesia supplemented with a Carprofen injection (5mg/kg, s.c.) and local anesthesia in the form of Lidocaine (0.2%, s.c.) under the scalp. Animals were kept warm on a temperature-controlled heat blanket during the procedure, and their eyes were protected against dehydration with viscotears. Hair was removed, and betadine used to sterilize the skin prior to the first incision. A square hole 3x3 mm was drilled in the bone and, leaving the dura intact, was covered with a fitting glass coverslip (thickness #1), which was then glued to the cranium. A L-shaped metal plate used to head-restrain the mice during the imaging was fixed to the skull by glue and dental cement. Analgesics were given for three days after surgery (paracetamol 125mg dissolved in 250ml water).

Electromyography (EMG)

We precisely recorded animal movements by electromyography (EMG)(King, Brown, & Pauly, 2014; Papouin, Dunphy, Tolman, Dineley, & Haydon, 2017). To achieve this, two electrodes were implanted

within the neck muscles of the mouse after the chronic cranial window preparation and connected to two micro sockets. During *in vivo* imaging, the sockets were connected to a preamplifier and a Molecular Devices digitizer (Digidata 1440A). The signal was recorded using pClamp and then filtered (50Hz filter) using a custom-made Matlab script. The onset of each recording was triggered by a digital signal from the Bruker microscope upon initiation of each 2-photon imaging sequence. The periods with the largest changes in activity were identified to detect mouse movements.

Fluorophores

To visualize the lumen of the blood vessels, we introduced dyes to the circulation. These were dextran conjugates with Texas red 70.000MW or TRITC (tetramethylrhodamine) 10.000MW (2% in 0.9% NaCl sterile solution, 100ul bolus I.V.) by tail-vein injection just prior to the imaging session. The vascular dyes were of a size that prohibits extrusion into the tissue surrounding the vessel. Hence, they were ideally suited to highlight the lumen of the blood vessels and signal diameter changes (Damisah, Hill, Tong, Murray, & Grutzendler, 2017; Mishra et al., 2016).

3D Awake Imaging

Before imaging, the mouse was habituated to human handling for two days and gradually introduced to being head-restraint under the microscope and thoroughly trained for an additional five days. The head of the animal was restrained by a custom-made system in which a metal plate attached to the head mount of the mouse was fastened with a screw to a matching metal bar. During imaging, the mouse sat on an air-supported, freely floating ball that acted as a spherical treadmill, allowing the animal to run when it wanted. The head of the mouse was slightly tilted, and the objective was at a 40° angle to allow perpendicular imaging through the glass covering the auditory cortex. Two-photon imaging was done with a Bruker *in vivo* Investigator system (Bruker Nano Surfaces Division, Madison, WI, USA) equipped with an 8kHz resonant galvanometer scanner, coupled to a MaiTai eHP DS laser (Spectra-physics, Milpitas, CA, USA) with 70fs pulse duration, tuned to 920 nm. Negative dispersion was optimized for each wavelength, and laser power was rapidly modulated by Pockels cells. A 20x LUMPFL60X W/IR-2 NA 0.9 Olympus objective was used. Emission was separated by a dichroic beam splitter (t560lpxr) and passed through either an et520/540m-2p (for red) or an et610/675m-2p (for green) emission filter. The combination of a resonant scanner with a piezoelectric actuator made high-speed 3D imaging possible, while highly sensitive GaAsP detectors with negative dispersion allowed for minimal laser dose applied to the tissue. The laser power varied during experiments depending on the depth of the focus, but it was kept below 7 mW and measured continuously with a power meter. These imaging settings were previously thoroughly investigated to ensure their non-toxicity to the tissue, even at high-speed image acquisitions (Bindocci et al., 2017). PA and 1st order branch points defined which depths were imaged. All but one junctional imaging site were ≥ 80 µm below the brain surface, with a maximal depth of 328 µm. The 3D-FOV covered an imaging volume of (56-75 µm (x) x 15-44 µm (y) x 21-35 µm (z); acquisition speed: 200 Hz; optical-zoom: 8x; with pixel size of 0.29-0.59 µm lateral resolution and 1 µm axial resolution. The scanning rate

was 8-10 Hz 3D stacks per second. A maximum of 20 Imaging sequences, 100 seconds long (800-1000 stacks in total), taken with 1-5 min breaks between them, depending on the mouse behavior.

Auditory stimulations

Once, during each of the 100s imaging sequences, mice were subjected to sound stimulation from an Electrostatic loudspeaker (Tucker-Davis Technologies, Inc.) placed 30cm from the left ear of the mouse. This was connected to the pClamp digitizer, which was programmed to produce a 10 s-long, 1 Hz auditory stimulation with 10 repetitions of a tone, each lasting 500ms, 30 s after the initiation of the imaging sequence. Four different tone frequencies were used as stimuli: either white noise, 3 kHz, 20 kHz, or 30 kHz. Each tone was repeated over 10 seconds, once during three different 100 s long imaging sessions.

Intrinsic optical signaling (IOS)

Before performing 2-photon imaging, a tonicity map of the auditory cortex was made using intrinsic optical signaling. Using the 4× objective of the microscope, we could include the entire cranial window in the field of view. The light source consisted of a light source with a green light excitation filter (532nm) to ensure imaging of changes in blood volume (Frostig, Lieke, Ts'o, & Grinvald, 1990). Images were sampled at 10Hz and compared between 10 s before and 10 s during a tone stimulation. Comparisons were repeated for all the tone frequencies used in the stimulations. The difference in absorption due to shifts in oxyhemoglobin and deoxyhemoglobin concentrations was calculated (Harrison, Sigler, & Murphy, 2009) to show the position of the largest hemodynamic response to each of the different tone stimulations.

Mouse pupil imaging

During some 2-photon imaging experiments, a high-resolution, fast-speed IR camera was focused on the eye of the mouse. The camera was a Dalsa Genie Nano, run with the Sapera LT and CamExpert software. The onset of this imaging was triggered by a digital signal from the Bruker microscope upon initiation of each imaging sequence. In addition, a bandpass filter of 850nm was placed before the objective to keep out visible light. The pupil was reflecting the IR light during the 2-photon imaging, making it possible to follow the contractions and dilations with a simple custom-made MATLAB script. The periods with pupil dilations were detected based on the z-score of the data. An expansion was defined as a pupil enlargement >2 standard deviations of its average size in the imaging period. The timing of the pupil expansions was compared to astrocytic Ca2+ levels averaged across the entire FOV. This was a rough measurement of large astrocytic Ca2+ events. Overlap between the two (Suppl. Fig S2H) was quantified as periods with >2SD in both measurements.

3D imaging data analysis

The data obtained by the 3D two-photon imaging was analyzed with custom-made MATLAB scripts and visualized using both ImageJ and Imaris 8.2. The analysis consisted of several steps. First each z-level (or focal plane) in the 3D stack was considered as an independent 2D image (Sup. Figure S1A and B). In each of these images, the vessel compartments and the related astrocyte end-feet structures were

automatically detected in rectangular regions, which were manually defined by the user based on the position of the vessel structure (Sup. Figure S1C). This was done in the following way: For each XYZT scan, rectangular crops were manually drawn to roughly outline a specific vessel segment in each focal plane (Sup. Figure S1D and S3). The area and position of the vessel within each of these during the time course of the imaging sequence were found at each z-level. This detection was done by first normalizing the pixel intensities in the red channel, considering all images in the crop during the entire imaging sequence, and calculating the z-score. Then, the image at each timepoint was masked using a gaussian filter (imgaussfilt.mat variable sigma decreasing from 8- 5 with increasing imaging depth), and a size threshold disregarding any structure found to be smaller than 8% of the selected rectangle (bwareaopen.mat) (Sup. Figure S1E). Movements were corrected based on the position of the centromere of the mask compared to the centromere of the average of all images over the imaging sequence, disregarding all other z-levels, and used to reposition the rectangular crop for each time point. In cases when the vessel left the 3D-field of view at a given time point so that a repositioning of the crop could not catch it, the timepoint was deleted from the entire xyzt stack. Such a deletion could be necessary during substantial movements or locomotions, and such data was thus excluded from the study. End-feet structures were defined for each imaging plane based on the edges of the vessel and 2 µm from that edge, which gave a 3D annulus ROI around the vascular structure (Sup. Figure S1F). These end-feet ROIs would then consider activity within all astrocytic structures at a proximity of 2 µm, regardless of which cell was the origin of the structure or any possible lack of end-feet coverage. The ROI width of 2 µm was chosen based on previous EM descriptions of the continuity and thickness of end-foot layer around vessels in the CNS(Mathiisen, Lehre, Danbolt, & Ottersen, 2010). End-feet thickness is less than 1 µm, and we then added a conservative +1 µm margin to ensure its complete inclusion. This ROI was divided into fours so it could be moved in relation to vessel position and constriction/dilation activity along the x- and y-axis (Sup. Figure S1G). Thus, first, the position of the rectangular crop was adjusted according to the detected movements, and then the end-feet ROIs were moved in relation to the position of the vessel mask. The Ca2+ activity in the astrocytic end-feet was averaged within these ROIS, and the pre-dilation activity was detected in 3D as further described below (Sup. Figure S6). This detection depended on the onset of dilation events, which were first quantified in 3D. To do so, the vessel area was quantified as the sum of pixels in the red channel with a significant (>2SD) level of fluorescence considering all pixels in the x- and y-rectangle along all time points in the timeseries. These values were summarized to reveal the zt diameter changes (Figure 1C) used to further characterize dilation patterns in 3D (Sup. Figure S3).

Detection of dilation events and patterns

The vascular structures within the 3D-FOV were classified as either PA, sphincter, bulb, or capillary region when the rectangular crops were manually drawn at each 2D image at a given z-level (Sup. Figure S1C and S3B). Thus, the spatial-temporal pattern of each dilation event could be detected. For each vessel segment, the change in diameter over time in the different z-levels was calculated using SD values considering the periods without movements as baseline periods, which were used in the normalization of the data from the entire imaging session. These normalized values were then combined in a zt image with the relative changes in x-y diameter shown as the intensity of the pixels (Sup. Figure S3C). This zt rendering of the data was then normalized (P-mean(P) /std(P)), considering all time points of the acquisition equally.

A 2SD threshold was used prior to a gaussian blurring (imgaussfilt.mat, sigma=2) followed by a removal of the smallest entities that were either too local or of too short a duration (bwareaopen.mat, filter: ¼*z-levels*Imaging frequency), to define periods of dilations that reached through the 3D levels of the vessel (Sup. Figure S3D). In this way, a diverse and, in some cases, ambiguous vascular activity (Sup. Figure S3E) was simplified into a binary dilation (1) or no dilation (0). The binarization was done for each vessel segment during the acquisition period (Sup. Figure S3F). Comparing the information from the different segments, the onset of each dilation event was evaluated as it either initiated within or reached the 3D-FOV. For each, it was quantified which vessel segment dilated first and when. In addition, the number of vessel compartments participating in the dilation and the onset of dilation in the other vessel segments relative to the initial onset of the dilation event was detected (Sup. Figure S1G). Based on the information on dilation duration and onset, dilations were considered as separate events when occurring with >500 ms intervals.

Detection of astrocytic activity along the PA in the large step 3D imaging

In the 3-FOVs scanning down along the PA, the astrocytic end-feet structures were imaged 10-20 µm apart along the z-axis. Thus, the structures were treated as individual entities, and activities averaged within each focal plane were analyzed separately. Astrocytic Ca2+ activity was defined as the peaks in the mean fluorescent signal from all the end-feet surrounding the PA. Peaks were detected in the normalized ((x-mean)/sd), smoothed (`sgolayfilt.mat`, order value=10) mean signal. The Matlab command `findpeaks.mat` was used with `MinPeakHeight` = 1 SD of the smoothed data, `'MinPeakProminence'`= 0.8 SD of the smoothed data, `MinPeakWidth` =1 second, and `widthReference=halfheight`. After the peaks start and stop had been detected, finding where the smoothed data came above and below baseline values, the true prominence of the signal was verified to be >2 SD in the non-smoothed normalized data. Finally, the timing of the Ca2+ events was compared between the different focal planes and, based on continuity and overlay in time, classified as one event that could be quantified in z-spread (µm) and duration (s).

Detection of pre-dilation astrocytic 3D Ca2+ activity

Following the quantification of the timing and dilation patterns based on the Texas red fluorescence in the vessel lumen (Sup. Figure S6A-B), the known onset of each dilation event was used to identify recurring Ca2+ activity in the astrocytic end-feet in relation to the different dilation patterns (Sup. Figure S6C). The average astrocytic Ca2+ activity from the end-feet ROIs around each vessel segment at each z-level in the 3D-FOV stack was normalized to SD-values, considering the periods without movements as baseline. As with the vessel dilation data, this normalized information was combined in a zt matrix. The matrix showed the average Ca2+ changes in the astrocytic end-feet ROIs, found at each xy imaging level, as changes along the z-axis over time. The 3D-t responses were then cropped based on the onset of each dilation, including a 2-second period preceding and the first second during the dilation event(Sup. Figure S6D). This period was chosen based on the expected delay from neuronal activation to vascular responses found in neurovascular coupling studies(Cai et al., 2018; Institoris et al., 2022; Rungta et al., 2018). Of course, since the dilations were spontaneous and some were based on activations further from or closer to the 3D-FOV, the true onset of the different processes leading to these dilation events could not be known with certainty. The information we had was when the dilation began or arrived at the parts of the vessels under investigation. Based on previous findings, it was expected that any astrocytic activity

relevant to the dilation spread or initiation would be present within a 2-second pre-dilation period(Lind et al., 2018). The zt investigation of the astrocytic Ca2+ activity was normalized in each crop considering all z-levels over the entire 3 s period. Periods with elevated Ca2+ activity and its position along the z-axis were identified by using a threshold to include only Ca^{2+}increases >2SD, a gaussian filtering with a 0.5 sigma gaussian blur (imgaussfilt.mat), and the exclusion of events smaller than 3 µmx100ms (bwareaopen.mat). The result was a binary mask in zt defining the temporal and spatial position of any astrocytic Ca2+ activity in the end-feet in relation to each dilation event. The masks were then compared between all dilation events that recruited the 1st order capillary junction within all imaging sessions from that experiment. In the comparison, the overlap between the binary masks was used to define the pre-dilation astrocytic Ca2+ activity ROIs with regards to timing and spread along the xyz-axis. After establishing these ROIs, they were then re-applied to the Ca2+ activity related to the individual dilation events to detect whether the astrocytic end-feet showed significant activity in the depth and time specified by the ROI in relation to the dilation (Sup. Figure S6E). A dilation was considered to be preceded by this type of pre-dilation Ca2+ activity if an overlap was found between the Ca2+ activity and the average zt ROI at that specific position in xyzt. Finally, it was investigated how recurrently each possible pre-dilation Ca2+ activity was detected prior to the dilations, considering the specific dilation patterns with regards to the location of dilation onset and which vessel segments participated in the dilation events (Sup. Figure S6F). Only the pre-dilation Ca2+ signal preceding all dilations with a specific dilation pattern was included in the study. This inclusion criteria was based on occurrence frequency, with a margin defined by the number of dilations and using a 0.1 confidence limit (1-(((N/2)-((sqrt(N)/2)*3.291)/N). Hence, if a pre-dilation Ca2+ signal occurred in 59% of N=50 dilations, it was considered to be a reoccurring event related to that dilation pattern (Sup. Figure S6G).

Detection of large astrocytic Ca2+ events.

The astrocytic Ca2+ activity from the end-feet ROIs was analyzed using the zt projection of activity to identify large activity. A large activity was defined as activity that was more than 2 SD above non-movement values and would spread through the z-layers to include the entire depth of the z-stack in >75 % of the end-feet ROIs.

Statistics

For all statistical analyses, OriginPro 2018b (OriginLab, Northampton, MA), Matlab 2019b, and Excel were used. Data were considered significantly different when the p-value was *<0.05, but additional strength was marked with **<0.01 and *** <0.005. When data could not be considered independent or achieve normal distribution with a log transformation, non-parametric tests were used: the Wilcoxon signed-rank test for paired data and the Mann-Whitney test for non-paired data. When comparing individual points from two groups, we performed the Kruskal-Wallis test or two-way ANOVA to exclude group effects before moving on to the single-point comparisons. When performing multiple comparisons on data, we used the Holm correction (similar to Holm-Bonferroni) on both parametric and non-parametric data based on the number of comparisons that the data group used to correct the p-value.

Acknowledgments

We would like to thank Ph.D. Giovanni Carriero and Erika Bindocci for their practical support during the project. In addition, we would like to thank prof. Tania Barkat, University of Basel, for her advice on setting up the auditory stimulations. We would like to thank MD PhD professor Martin Lauritzen and PhD Søren Grubb of the University of Copenhagen for valuable scientific discussions. This work was supported by ERC advanced "Astromnesis", the SNSF 31003A-173124, and SNSF 31003B-201276 grants to AV and by a post. doc fellowship to B.L. from The Lundbeck Foundation, Denmark.

Reference List

Arizono, M., Inavalli, V., Panatier, A., Pfeiffer, T., Angibaud, J., Levet, F., . . . Nagerl, U. V. (2020). Structural basis of astrocytic Ca(2+) signals at tripartite synapses. *Nat Commun, 11*(1), 1906. doi:10.1038/s41467-020-15648-4

Bandyopadhyay, S., Shamma, S. A., & Kanold, P. O. (2010). Dichotomy of functional organization in the mouse auditory cortex. *Nat Neurosci, 13*(3), 361-368. doi:10.1038/nn.2490

Bazargani, N., & Attwell, D. (2016). Astrocyte calcium signaling: the third wave. *Nat Neurosci, 19*(2), 182-189. doi:10.1038/nn.4201

Biesecker, K. R., Srienc, A. I., Shimoda, A. M., Agarwal, A., Bergles, D. E., Kofuji, P., & Newman, E. A. (2016). Glial Cell Calcium Signaling Mediates Capillary Regulation of Blood Flow in the Retina. *J Neurosci, 36*(36), 9435-9445. doi:10.1523/JNEUROSCI.1782-16.2016

Bindocci, E., Savtchouk, I., Liaudet, N., Becker, D., Carriero, G., & Volterra, A. (2017). Three-dimensional Ca2+ imaging advances understanding of astrocyte biology. *Science, 356*(6339). doi:10.1126/science.aai8185

Bonder, D. E., & McCarthy, K. D. (2014). Astrocytic Gq-GPCR-linked IP3R-dependent Ca2+ signaling does not mediate neurovascular coupling in mouse visual cortex in vivo. *J Neurosci, 34*(39), 13139-13150. doi:10.1523/JNEUROSCI.2591-14.2014

Cai, C., Fordsmann, J. C., Jensen, S. H., Gesslein, B., Lonstrup, M., Hald, B. O., . . . Lauritzen, M. J. (2018). Stimulation-induced increases in cerebral blood flow and local capillary vasoconstriction depend on conducted vascular responses. *Proc Natl Acad Sci U S A, 115*(25), E5796-E5804. doi:10.1073/pnas.1707702115

Cai, C., Zambach, S. A., Grubb, S., Tao, L., He, C., Lind, B. L., . . . Lauritzen, M. J. (2023). Impaired dynamics of precapillary sphincters and pericytes at first-order capillaries predict reduced neurovascular function in the aging mouse brain. *Nat Aging, 3*(2), 173-184. doi:10.1038/s43587-022-00354-1

Chen, B. R., Kozberg, M. G., Bouchard, M. B., Shaik, M. A., & Hillman, E. M. (2014). A critical role for the vascular endothelium in functional neurovascular coupling in the brain. *J Am Heart Assoc, 3*(3), e000787. doi:10.1161/JAHA.114.000787

Chen, C., She, Z., Tang, P., Qin, Z., He, J., & Qu, J. Y. (2021). Study of neurovascular coupling by using mesoscopic and microscopic imaging. *iScience, 24*(10), 103176. doi:10.1016/j.isci.2021.103176

Damisah, E. C., Hill, R. A., Tong, L., Murray, K. N., & Grutzendler, J. (2017). A fluoro-Nissl dye identifies pericytes as distinct vascular mural cells during in vivo brain imaging. *Nat Neurosci, 20*(7), 1023-1032. doi:10.1038/nn.4564

De Franceschi, G., & Barkat, T. R. (2021). Task-induced modulations of neuronal activity along the auditory pathway. *Cell Rep, 37*(11), 110115. doi:10.1016/j.celrep.2021.110115

Del Franco, A. P., Chiang, P. P., & Newman, E. A. (2022). Dilation of cortical capillaries is not related to astrocyte calcium signaling. *Glia, 70*(3), 508-521. doi:10.1002/glia.24119

Di Castro, M. A., Chuquet, J., Liaudet, N., Bhaukaurally, K., Santello, M., Bouvier, D., . . . Volterra, A. (2011). Local Ca2+ detection and modulation of synaptic release by astrocytes. *Nat Neurosci, 14*(10), 1276-1284. doi:10.1038/nn.2929

Ding, F., O'Donnell, J., Thrane, A. S., Zeppenfeld, D., Kang, H., Xie, L., . . . Nedergaard, M. (2013). alpha1-Adrenergic receptors mediate coordinated Ca2+ signaling of cortical astrocytes in awake, behaving mice. *Cell Calcium, 54*(6), 387-394. doi:10.1016/j.ceca.2013.09.001

Duque, D., Pais, R., & Malmierca, M. S. (2018). Stimulus-specific adaptation in the anesthetized mouse revealed by brainstem auditory evoked potentials. *Hear Res, 370*, 294-301. doi:10.1016/j.heares.2018.08.011

Eyre, B., Shaw, K., Sharp, P., Boorman, L., Lee, L., Shabir, O., . . . Howarth, C. (2022). The effects of locomotion on sensory-evoked haemodynamic responses in the cortex of awake mice. *Sci Rep, 12*(1), 6236. doi:10.1038/s41598-022-10195-y

Fabricius, M., Akgoren, N., Dirnagl, U., & Lauritzen, M. (1997). Laminar analysis of cerebral blood flow in cortex of rats by laser-Doppler flowmetry: a pilot study. *Journal of Cerebral Blood Flow & Metabolism, 17*(12), 1326-1336.

Frostig, R. D., Lieke, E. E., Ts'o, D. Y., & Grinvald, A. (1990). Cortical functional architecture and local coupling between neuronal activity and the microcirculation revealed by in vivo high-resolution optical imaging of intrinsic signals. *Proc.Natl.Acad.Sci.U.S.A, 87*(16), 6082-6086.

Grubb, S., Cai, C., Hald, B. O., Khennouf, L., Murmu, R. P., Jensen, A. G. K., . . . Lauritzen, M. (2020). Precapillary sphincters maintain perfusion in the cerebral cortex. *Nat Commun, 11*(1), 395. doi:10.1038/s41467-020-14330-z

Grubb, S., Lauritzen, M., & Aalkjaer, C. (2021). Brain capillary pericytes and neurovascular coupling. *Comp Biochem Physiol A Mol Integr Physiol, 254*, 110893. doi:10.1016/j.cbpa.2020.110893

Gu, X., Chen, W., Volkow, N. D., Koretsky, A. P., Du, C., & Pan, Y. (2018). Synchronized Astrocytic Ca(2+) Responses in Neurovascular Coupling during Somatosensory Stimulation and for the Resting State. *Cell Rep, 23*(13), 3878-3890. doi:10.1016/j.celrep.2018.05.091

Haidey, J. N., Peringod, G., Institoris, A., Gorzo, K. A., Nicola, W., Vandal, M., . . . Gordon, G. R. (2021). Astrocytes regulate ultra-slow arteriole oscillations via stretch-mediated TRPV4-COX-1 feedback. *Cell Rep, 36*(5), 109405. doi:10.1016/j.celrep.2021.109405

Hall, C. N., Reynell, C., Gesslein, B., Hamilton, N. B., Mishra, A., Sutherland, B. A., . . . Attwell, D. (2014). Capillary pericytes regulate cerebral blood flow in health and disease. *Nature*. doi:10.1038/nature13165

Harrison, T. C., Sigler, A., & Murphy, T. H. (2009). Simple and cost-effective hardware and software for functional brain mapping using intrinsic optical signal imaging. *J Neurosci Methods, 182*(2), 211-218. doi:10.1016/j.jneumeth.2009.06.021

Hartmann, D. A., Berthiaume, A. A., Grant, R. I., Harrill, S. A., Koski, T., Tieu, T., . . . Shih, A. Y. (2021). Brain capillary pericytes exert a substantial but slow influence on blood flow. *Nat Neurosci, 24*(5), 633-645. doi:10.1038/s41593-020-00793-2

Hartmann, D. A., Coelho-Santos, V., & Shih, A. Y. (2022). Pericyte Control of Blood Flow Across Microvascular Zones in the Central Nervous System. *Annu Rev Physiol, 84*, 331-354. doi:10.1146/annurev-physiol-061121-040127

Hill, R. A., Tong, L., Yuan, P., Murikinati, S., Gupta, S., & Grutzendler, J. (2015). Regional Blood Flow in the Normal and Ischemic Brain Is Controlled by Arteriolar Smooth Muscle Cell Contractility and Not by Capillary Pericytes. *Neuron, 87*(1), 95-110. doi:10.1016/j.neuron.2015.06.001

Hirrlinger, P. G., Scheller, A., Braun, C., Hirrlinger, J., & Kirchhoff, F. (2006). Temporal control of gene recombination in astrocytes by transgenic expression of the tamoxifen-inducible DNA recombinase variant CreERT2. *Glia, 54*(1), 11-20. doi:10.1002/glia.20342

Howarth, C., Mishra, A., & Hall, C. N. (2021). More than just summed neuronal activity: how multiple cell types shape the BOLD response. *Philos Trans R Soc Lond B Biol Sci, 376*(1815), 20190630. doi:10.1098/rstb.2019.0630

Iadecola, C. (2017). The Neurovascular Unit Coming of Age: A Journey through Neurovascular Coupling in Health and Disease. *Neuron, 96*(1), 17-42. doi:10.1016/j.neuron.2017.07.030

Institoris, A., Vandal, M., Peringod, G., Catalano, C., Tran, C. H., Yu, X., . . . Gordon, G. R. (2022). Astrocytes amplify neurovascular coupling to sustained activation of neocortex in awake mice. *Nat Commun, 13*(1), 7872. doi:10.1038/s41467-022-35383-2

Issa, J. B., Haeffele, B. D., Agarwal, A., Bergles, D. E., Young, E. D., & Yue, D. T. (2014). Multiscale optical Ca2+ imaging of tonal organization in mouse auditory cortex. *Neuron, 83*(4), 944-959. doi:10.1016/j.neuron.2014.07.009

Kameyama, H., Masamoto, K., Imaizumi, Y., Omura, T., Katura, T., Maki, A., & Tanishita, K. (2008). Neurovascular coupling in primary auditory cortex investigated with voltage-sensitive dye imaging and laser-Doppler flowmetry. *Brain Res, 1244*, 82-88. doi:10.1016/j.brainres.2008.09.058

Khakh, B. S., & Sofroniew, M. V. (2015). Diversity of astrocyte functions and phenotypes in neural circuits. *Nat Neurosci, 18*(7), 942-952. doi:10.1038/nn.4043

King, R. L., Brown, J. R., & Pauly, K. B. (2014). Localization of ultrasound-induced in vivo neurostimulation in the mouse model. *Ultrasound Med Biol, 40*(7), 1512-1522. doi:10.1016/j.ultrasmedbio.2014.01.020

Kirst, C., Skriabine, S., Vieites-Prado, A., Topilko, T., Bertin, P., Gerschenfeld, G., . . . Renier, N. (2020). Mapping the Fine-Scale Organization and Plasticity of the Brain Vasculature. *Cell, 180*(4), 780-795 e725. doi:10.1016/j.cell.2020.01.028

Kornfield, T. E., & Newman, E. A. (2014). Regulation of blood flow in the retinal trilaminar vascular network. *J Neurosci, 34*(34), 11504-11513. doi:10.1523/JNEUROSCI.1971-14.2014

Kral, A., Yusuf, P. A., & Land, R. (2017). Higher-order auditory areas in congenital deafness: Top-down interactions and corticocortical decoupling. *Hear Res, 343*, 50-63. doi:10.1016/j.heares.2016.08.017

Larsen, R. S., & Waters, J. (2018). Neuromodulatory Correlates of Pupil Dilation. *Front Neural Circuits, 12*, 21. doi:10.3389/fncir.2018.00021

Lind, B. L., Jessen, S. B., Lonstrup, M., Josephine, C., Bonvento, G., & Lauritzen, M. (2018). Fast Ca(2+) responses in astrocyte end-feet and neurovascular coupling in mice. *Glia, 66*(2), 348-358. doi:10.1002/glia.23246

Longden, T. A., Dabertrand, F., Koide, M., Gonzales, A. L., Tykocki, N. R., Brayden, J. E., . . . Nelson, M. T. (2017). Capillary K+-sensing initiates retrograde hyperpolarization to increase local cerebral blood flow. *Nat Neurosci*. doi:10.1038/nn.4533

Mathiisen, T. M., Lehre, K. P., Danbolt, N. C., & Ottersen, O. P. (2010). The perivascular astroglial sheath provides a complete covering of the brain microvessels: an electron microscopic 3D reconstruction. *Glia, 58*(9), 1094-1103. doi:10.1002/glia.20990

McCaslin, A. F., Chen, B. R., Radosevich, A. J., Cauli, B., & Hillman, E. M. (2011). In vivo 3D morphology of astrocyte-vasculature interactions in the somatosensory cortex: implications for neurovascular coupling. *J Cereb Blood Flow Metab, 31*(3), 795-806. doi:10.1038/jcbfm.2010.204

Mishra, A., Gordon, G. R., MacVicar, B. A., & Newman, E. A. (2024). Astrocyte Regulation of Cerebral Blood Flow in Health and Disease. *Cold Spring Harb Perspect Biol, 16*(4). doi:10.1101/cshperspect.a041354

Mishra, A., Reynolds, J. P., Chen, Y., Gourine, A. V., Rusakov, D. A., & Attwell, D. (2016). Astrocytes mediate neurovascular signaling to capillary pericytes but not to arterioles. *Nat Neurosci, 19*(12), 1619-1627. doi:10.1038/nn.4428

Mughal, A., Nelson, M. T., & Hill-Eubanks, D. (2023). The post-arteriole transitional zone: a specialized capillary region that regulates blood flow within the CNS microvasculature. *J Physiol, 601*(5), 889-901. doi:10.1113/JP282246

Nizar, K., Uhlirova, H., Tian, P., Saisan, P. A., Cheng, Q., Reznichenko, L., . . . Devor, A. (2013). In vivo Stimulus-Induced Vasodilation Occurs without IP3 Receptor Activation and May Precede Astrocytic Calcium Increase. *The Journal of Neuroscience, 33*(19), 8411-8422. doi:10.1523/jneurosci.3285-12.2013

Nolte, C., Matyash, M., Pivneva, T., Schipke, C. G., Ohlemeyer, C., Hanisch, U. K., . . . Kettenmann, H. (2001). GFAP promoter-controlled EGFP-expressing transgenic mice: a tool to visualize astrocytes and astrogliosis in living brain tissue. *Glia, 33*(1), 72-86.

O'Herron, P., Chhatbar, P. Y., Levy, M., Shen, Z., Schramm, A. E., Lu, Z., & Kara, P. (2016). Neural correlates of single-vessel haemodynamic responses in vivo. *Nature, 534*(7607), 378-382. doi:10.1038/nature17965

Ostergaard, L. (2020). Blood flow, capillary transit times, and tissue oxygenation: the centennial of capillary recruitment. *J Appl Physiol (1985), 129*(6), 1413-1421. doi:10.1152/japplphysiol.00537.2020

Otsu, Y., Couchman, K., Lyons, D. G., Collot, M., Agarwal, A., Mallet, J. M., . . . Charpak, S. (2015). Calcium dynamics in astrocyte processes during neurovascular coupling. *Nat Neurosci, 18*(2), 210-218. doi:10.1038/nn.3906

Ozawa, K., Nagao, M., Konno, A., Iwai, Y., Vittani, M., Kusk, P., . . . Hirase, H. (2023). Astrocytic GPCR-Induced Ca(2+) Signaling Is Not Causally Related to Local Cerebral Blood Flow Changes. *Int J Mol Sci, 24*(17). doi:10.3390/ijms241713590

Panatier, A., Vallee, J., Haber, M., Murai, K. K., Lacaille, J. C., & Robitaille, R. (2011). Astrocytes are endogenous regulators of basal transmission at central synapses. *Cell, 146*(5), 785-798. doi:10.1016/j.cell.2011.07.022

Papouin, T., Dunphy, J. M., Tolman, M., Dineley, K. T., & Haydon, P. G. (2017). Septal Cholinergic Neuromodulation Tunes the Astrocyte-Dependent Gating of Hippocampal NMDA Receptors to Wakefulness. *Neuron, 94*(4), 840-854 e847. doi:10.1016/j.neuron.2017.04.021

Paukert, M., Agarwal, A., Cha, J., Doze, V. A., Kang, J. U., & Bergles, D. E. (2014). Norepinephrine controls astroglial responsiveness to local circuit activity. *Neuron, 82*(6), 1263-1270. doi:10.1016/j.neuron.2014.04.038

Petzold, G. C., Albeanu, D. F., Sato, T. F., & Murthy, V. N. (2008). Coupling of neural activity to blood flow in olfactory glomeruli is mediated by astrocytic pathways. *Neuron, 58*(6), 897-910. doi:10.1016/j.neuron.2008.04.029

Privitera, M., Ferrari, K. D., von Ziegler, L. M., Sturman, O., Duss, S. N., Floriou-Servou, A., . . . Bohacek, J. (2020). A complete pupillometry toolbox for real-time monitoring of locus coeruleus activity in rodents. *Nat Protoc, 15*(8), 2301-2320. doi:10.1038/s41596-020-0324-6

Reimer, J., McGinley, M. J., Liu, Y., Rodenkirch, C., Wang, Q., McCormick, D. A., & Tolias, A. S. (2016). Pupil fluctuations track rapid changes in adrenergic and cholinergic activity in cortex. *Nat Commun, 7*, 13289. doi:10.1038/ncomms13289

Reitman, M. E., Tse, V., Mi, X., Willoughby, D. D., Peinado, A., Aivazidis, A., . . . Poskanzer, K. E. (2023). Norepinephrine links astrocytic activity to regulation of cortical state. *Nat Neurosci, 26*(4), 579-593. doi:10.1038/s41593-023-01284-w

Renden, R. B., Institoris, A., Sharma, K., & Tran, C. H. T. (2024). Modulatory effects of noradrenergic and serotonergic signaling pathway on neurovascular coupling. *Commun Biol, 7*(1), 287. doi:10.1038/s42003-024-05996-y

Rungta, R. L., Chaigneau, E., Osmanski, B. F., & Charpak, S. (2018). Vascular Compartmentalization of Functional Hyperemia from the Synapse to the Pia. *Neuron, 99*(2), 362-375 e364. doi:10.1016/j.neuron.2018.06.012

Rungta, R. L., Zuend, M., Aydin, A. K., Martineau, E., Boido, D., Weber, B., & Charpak, S. (2021). Diversity of neurovascular coupling dynamics along vascular arbors in layer II/III somatosensory cortex. *Commun Biol, 4*(1), 855. doi:10.1038/s42003-021-02382-w

Rupprecht, P., Duss, S. N., Becker, D., Lewis, C. M., Bohacek, J., & Helmchen, F. (2024). Centripetal integration of past events in hippocampal astrocytes regulated by locus coeruleus. *Nat Neurosci, 27*(5), 927-939. doi:10.1038/s41593-024-01612-8

Santello, M., Toni, N., & Volterra, A. (2019). Astrocyte function from information processing to cognition and cognitive impairment. *Nature Neuroscience, 22*(2), 154-166. doi:10.1038/s41593-018-0325-8

Sherwood, M. W., Arizono, M., Panatier, A., Mikoshiba, K., & Oliet, S. H. R. (2021). Astrocytic IP(3)Rs: Beyond IP(3)R2. *Front Cell Neurosci, 15*, 695817. doi:10.3389/fncel.2021.695817

Shigetomi, E., Jackson-Weaver, O., Huckstepp, R. T., O'Dell, T. J., & Khakh, B. S. (2013). TRPA1 channels are regulators of astrocyte basal calcium levels and long-term potentiation via constitutive D-serine release. *J Neurosci, 33*(24), 10143-10153. doi:10.1523/JNEUROSCI.5779-12.2013

Shimaoka, D., Harris, K. D., & Carandini, M. (2018). Effects of Arousal on Mouse Sensory Cortex Depend on Modality. *Cell Rep, 25*(11), 3230. doi:10.1016/j.celrep.2018.11.105

Solyga, M., & Barkat, T. R. (2022). Distinct integration of spectrally complex sounds in mouse primary auditory cortices. *Hear Res, 417*, 108455. doi:10.1016/j.heares.2022.108455

Srinivasan, R., Huang, B. S., Venugopal, S., Johnston, A. D., Chai, H., Zeng, H., . . . Khakh, B. S. (2015). Ca(2+) signaling in astrocytes from Ip3r2(-/-) mice in brain slices and during startle responses in vivo. *Nat Neurosci, 18*(5), 708-717. doi:10.1038/nn.4001

Stobart, J. L., Ferrari, K. D., Barrett, M. J. P., Gluck, C., Stobart, M. J., Zuend, M., & Weber, B. (2018). Cortical Circuit Activity Evokes Rapid Astrocyte Calcium Signals on a Similar Timescale to Neurons. *Neuron, 98*(4), 726-735 e724. doi:10.1016/j.neuron.2018.03.050

Stobart, J. L., Ferrari, K. D., Barrett, M. J. P., Stobart, M. J., Looser, Z. J., Saab, A. S., & Weber, B. (2018). Long-term In Vivo Calcium Imaging of Astrocytes Reveals Distinct Cellular Compartment Responses to Sensory Stimulation. *Cereb Cortex, 28*(1), 184-198. doi:10.1093/cercor/bhw366

Szymanski, F. D., Rabinowitz, N. C., Magri, C., Panzeri, S., & Schnupp, J. W. (2011). The laminar and temporal structure of stimulus information in the phase of field potentials of auditory cortex. *J Neurosci, 31*(44), 15787-15801. doi:10.1523/JNEUROSCI.1416-11.2011

Takuwa, H., Matsuura, T., Obata, T., Kawaguchi, H., Kanno, I., & Ito, H. (2012). Hemodynamic changes during somatosensory stimulation in awake and isoflurane-anesthetized mice measured by laser-Doppler flowmetry. *Brain Res, 1472*, 107-112. doi:10.1016/j.brainres.2012.06.049

Thrane, A. S., Thrane, V. R., Zeppenfeld, D., Lou, N., Xu, Q., Nagelhus, E. A., & Nedergaard, M. (2012). General anesthesia selectively disrupts astrocyte calcium signaling in the awake mouse cortex. *Proc Natl Acad Sci U S A, 109*(46), 18974-18979. doi:10.1073/pnas.1209448109

Tian, P., Teng, I. C., May, L. D., Kurz, R., Lu, K., Scadeng, M., . . . Devor, A. (2010). Cortical depth-specific microvascular dilation underlies laminar differences in blood oxygenation level-dependent functional MRI signal. *Proc.Natl.Acad.Sci.U.S.A, 107*(34), 15246-15251.

Tran, C. H. T., Peringod, G., & Gordon, G. R. (2018). Astrocytes Integrate Behavioral State and Vascular Signals during Functional Hyperemia. *Neuron, 100*(5), 1133-1148 e1133. doi:10.1016/j.neuron.2018.09.045

Tsukano, H., Horie, M., Bo, T., Uchimura, A., Hishida, R., Kudoh, M., . . . Shibuki, K. (2015). Delineation of a frequency-organized region isolated from the mouse primary auditory cortex. *J Neurophysiol, 113*(7), 2900-2920. doi:10.1152/jn.00932.2014

Vestergaard, M. B., Lindberg, U., Knudsen, M. H., Urdanibia-Centelles, O., Bakhtiari, A., Mortensen, E. L., . . . Larsson, H. B. W. (2022). Subclinical cognitive deficits are associated with reduced cerebrovascular response to visual stimulation in mid-sixties men. *Geroscience, 44*(4), 1905-1923. doi:10.1007/s11357-022-00596-2

Volterra, A., Liaudet, N., & Savtchouk, I. (2014). Astrocyte Ca(2)(+) signalling: an unexpected complexity. *Nat Rev Neurosci, 15*(5), 327-335. doi:10.1038/nrn3725

Wang, X., Lou, N., Xu, Q., Tian, G. F., Peng, W. G., Han, X., . . . Nedergaard, M. (2006). Astrocytic Ca2+ signaling evoked by sensory stimulation in vivo. *Nat Neurosci, 9*(6), 816-823. doi:10.1038/nn1703

Wei, H. S., Kang, H., Rasheed, I. D., Zhou, S., Lou, N., Gershteyn, A., . . . Nedergaard, M. (2016). Erythrocytes Are Oxygen-Sensing Regulators of the Cerebral Microcirculation. *Neuron, 91*(4), 851-862. doi:10.1016/j.neuron.2016.07.016

Winship, I. R., Plaa, N., & Murphy, T. H. (2007). Rapid astrocyte calcium signals correlate with neuronal activity and onset of the hemodynamic response in vivo. *J.Neurosci., 27*(23), 6268-6272.

Zambach, S. A., Cai, C., Helms, H. C. C., Hald, B. O., Dong, Y., Fordsmann, J. C., . . . Lauritzen, M. J. (2021). Precapillary sphincters and pericytes at first-order capillaries as key regulators for brain capillary perfusion. *Proc Natl Acad Sci U S A, 118*(26). doi:10.1073/pnas.2023749118

Supplemental Figures:

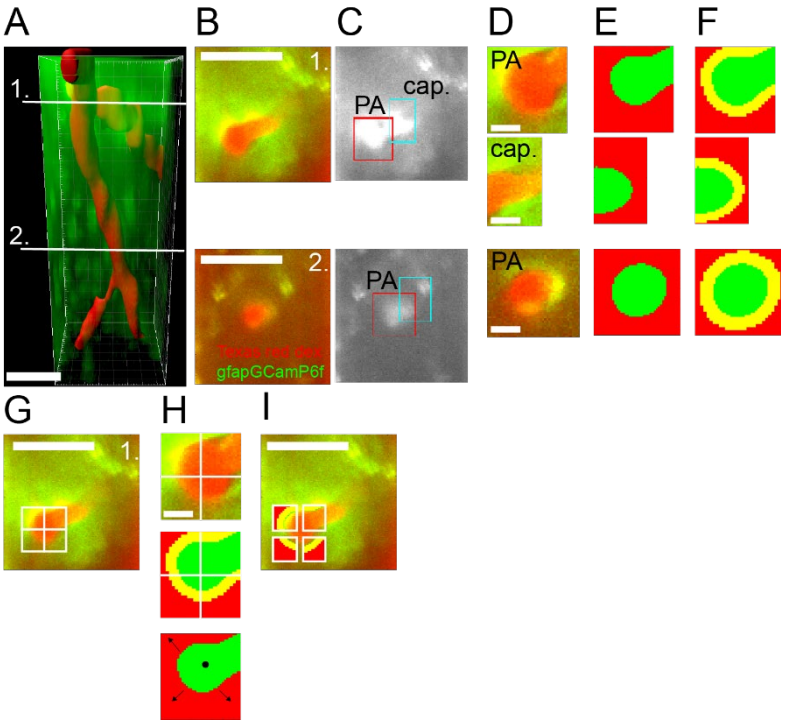

Sup. Figure S1. Method to detect vessel position and astrocyte end-feet ROIs within manually defined vessel segments in a 3D-FOV.

A) PA with two 1st order capillary branches taken 40-240 µm below the cortical surface. Cumulative average of a 3D-FOV x= 75.5µm, y= 75.5µm, z=200µm timeseries taken from the auditory cortex of a Texas red-dextran injected *GFAPCreERT2:GCaMP6f* mouse. *Red*: Masked vessel lumen. *Green*: GCaMP6f, *White lines*: show the position of two z-levels depicted in B)-F). Scalebar 30µm

B) Two 2D x-y images from the cumulative averaged xyz stack in A). *Red*: Texas red dextran in the vessel lumen, *Green*: GCaMP6f. Scalebar 30µm

C) Based on the cumulative average of the timeseries, the rectangular regions containing the relevant vessel segments were manually defined at each Z-level. This has to be done for every XYZ-T scan in the experiment. The manual definition must be consistent from level to level to follow the same vessel between layers. (*Red rect*.: PA segment, *blue rect*.: capillary segment).

D) Average fluorescence in the crops defined in C). Within the manually defined rectangle would be the Texas red dextran signal outlining that specific vessel segment and the GCaMP6f signal from the astrocyte structure surrounding this vessel segment. Scalebar 5µm

E) The area of each vessel segment was automatically found by masking gaussian filtered, normalized images using custom-written software (*green*).

F) End-feet structures were automatically defined for each imaging plane based on the edges of the vessel and 2 µm from that edge, which defined an ROI around the vascular structure (*yellow*).

G) Average fluorescence from Texas red-dextran injected *GFAPCreERT2:GCaMP6f* mouse in level 1 from A)-F) with the initial position of the defined crop. Scalebar 30µm

H) The crop of the vessel segment was split in quarters and moved relative to the position of the centromere of the PA and the outline of the vessel lumen. Scalebar 5µm

I) The quarter of the crop containing the End-feet rois was moved relative to the outline of the vessel lumen to reposition as end-feet ROIs were moved in relation to vessel position and diameter changes before measurements of astrocytic end-feet Ca2+. Scalebar 30µm

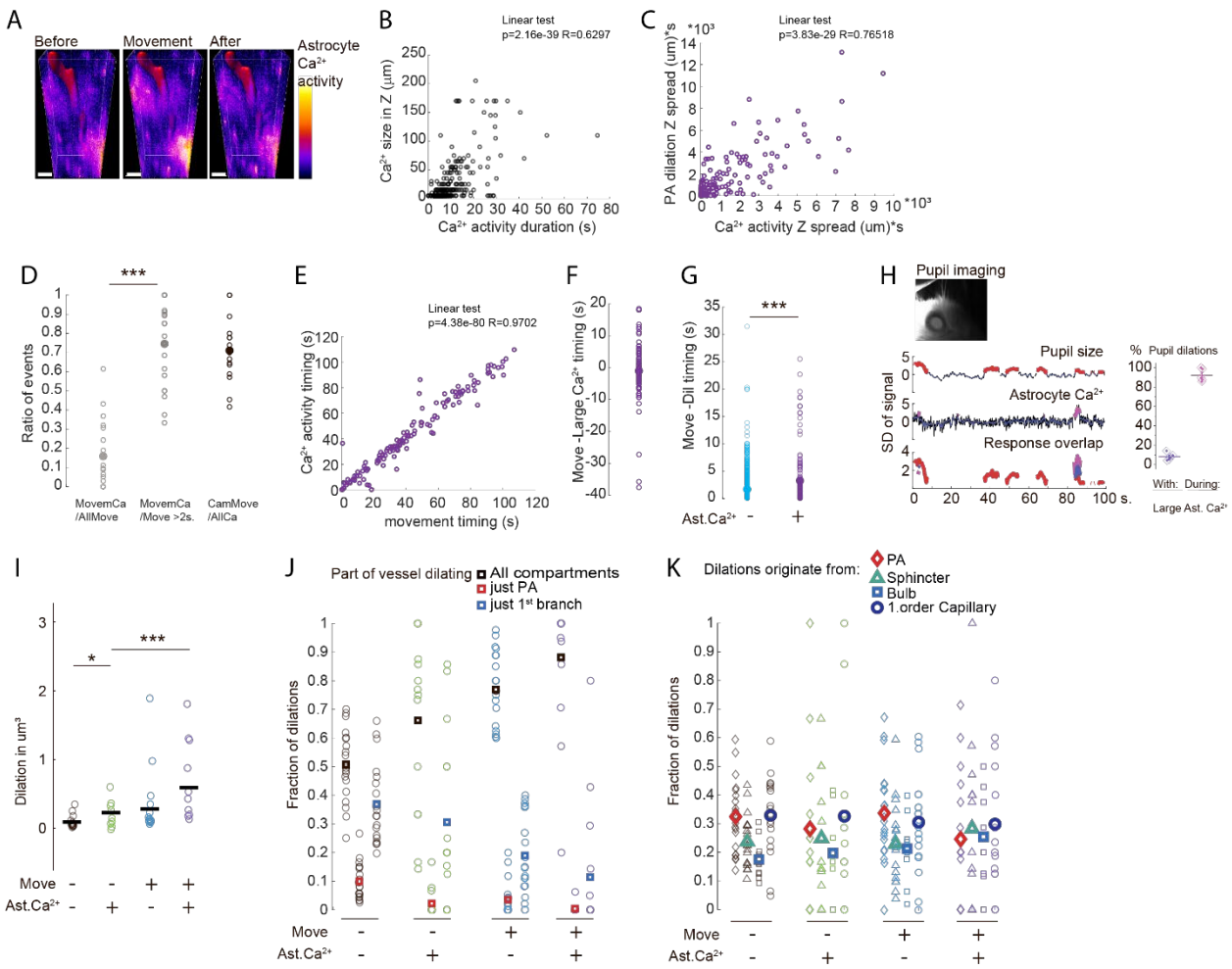

Sup. Figure S2. Correlations between movements, large astrocytic Ca2+ events, and dilations.

A) Astrocytic Ca2+ levels were measured with GFAPGCaMP6 (*pseudocolor*) during 5 s. of rest (*left*), during movements (*middle*) and after (*Right*). *Red*: Masked vessel lumen. Cumulative averages of the 5 s. of 3D-FOV from 2-photon imaging along the PA. Cortical depth 40-240 µm. Scalebar 20µm

B) Correlation between the duration (s) and size (in µm along the z-axis) of the Ca^{2+} activity in the events occurring along the z-axis of the PA in the resting animals (Pearson linear correlation $p=2.2*10^{-39}$, R=0.63, N=344 Ca^{2+} events, 8 FOV, in 6 mice).

C) Correlation between duration*spread along the z-axis of astrocytic Ca2+ vs PA dilations during movements (N= 145 dilations events, 8 PAs, in 6 mice), measured with 20 µm steps in z-stacks covering 100-280 µm of the depth of the cortex beginning from 50-100 µm below the surface. (Pearson linear correlation $p=3.9*10^{-29}$, R=0.76).

D) The ratio of events from each FOV shows how often large astrocytic Ca2+ activities and periods of movement overlap. Considering all movements, 15.9±7.5% overlapped, while of long duration movements (>2s), 74.6±10 was associated with astrocytic Ca2+ (Mann-Whitney test, p=0.0007, 11,1±4.6 Ca2+ events and 54.0±24.5 Movement events in N=20 FOV in 6 mice). 71.1±7.5% of large astrocytic Ca2+ activities were associated with movements of any duration.

E) Linear correlation between the onset of an astrocytic Ca2+ and movements considering all movements associated with a large Ca2+ activity in 129 events from 20 FOVs. (Pearson linear correlation, $p=4.37*10^{-8}$ R=0.97).

F) Movements initiated on average 1.03±1.25s before the astrocytic Ca2+ activity. Calculated per movement activity associated with a large Ca2+ activity in 129 events from 20 FOVs.

G) The delay between onset time of all movements and dilation of the vessels in the 3D-FOV shows that dilation initiated on average 1.71±0.16s before movements (*azure*). This delay was increased to 3.27±0.86s when the movement activity was associated with a large astrocytic Ca2+ event (*violet*). (Unpaired t-test, $p=9.9*10^{-9}$, N=953 no Ca2+ and N=129 movements with Ca2+ events from 20 FOVs).

H) *Top*: Mouse pupil diameter changes recorded during two-photon imaging sessions. *Left, bottom*: Example of simultaneous traces of pupil size measured in pixel area and normalized to SD values (*top*, dilations periods in red >2SD) and average astrocytic Ca2+ levels in the entire 3D-FOV measured as mean fluorescence intensity and normalized to SD values (*middle*, Ca2+ event periods in purple >2SD). The overlay (*bottom*) shows (*blue*) the overlapping periods. *Right, bottom*: Percentage of pupil dilations accompanied by a global Ca2+ activity (*left*) and, vice versa, percentage of global astrocytic Ca2+ events occurring in overlap with a pupil dilation (*right*). (N=95 Ca2+ activities and N=450 pupil dilations in 5 mice).

I) The average size of vessel dilation events per FOV in different conditions. (*black*: During rest 162±31.2 dilations/FOV, *green*: with large Ca2+ 4.2±2.0 dilations/FOV, *azure*: During move no Ca2+ 47.6±22.1 dilations/FOV, *violet*: During move with large Ca2+ 6.5±2.5 dilations/FOV, all in N = 20 FOV in 6 mice). Compared to the average dilation size during rest, dilations during large astrocytic Ca2+ activities alone or simultaneously with movements were significantly prolonged (t-test, with Holm correction: Rest vs. Ca2+: p=0.033, vs Ca2+ during movements:0.00039, N=20 FOV).

J) The fraction of all dilations in which one or all compartments dilated. Data points are color-coded depending on conditions, as in I). Mean value is shown in color dependent on the compartment recruited in the dilation, either just PA (*red*), just 1st order capillary branch (*blue*) or both (multicompartment, *black*). During movements or arousal, most dilations included both vessel compartments, whereas, during rest, only half the dilations spread between compartments (Wilcoxon test, All parts dilation in rest vs. Ca2+: p=0.059, rest vs. movement: p= 0.000047, movements vs movements with Ca2+: p=0.0067, rest vs movements with Ca2+: p=5.4*10-5, N=20 FOV, 6 mice).

K) The fraction of dilations that originated from either the PA (*red*), the sphincter (*cyan*), the bulb (*light blue*), or the 1st order capillary (*dark blue*). Data points' color coding is dependent on conditions such as I) and J). There was a heterogeneity of origin and, thus, of directionality, both in dilations during rest and when the animal was aroused or moved.

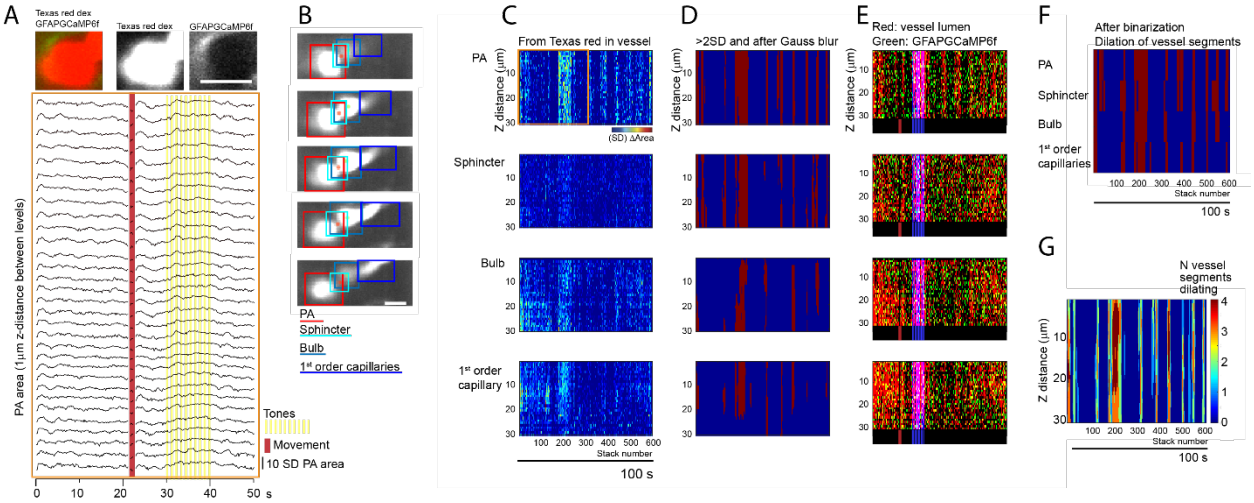

Sup. Figure S3. Method to detect dilation patterns in a 3D-FOV

A) *Above*: Average 2-photon image of PA and surrounding end-feet in a single z-level focal plane. *Red*: Texas red dextran shows vessel lumen. *Green*: GFAPGCaMP6f. Shown as an overlay (*left*) and as individual channels (*middle and right*). *Below*: The changes in vessel area of the PA from 1µm interspaced different z-depth between 95-125 µm below the surface. One dilation is related to a short movement (*red line*), and one to tone stimulation (*yellow marking*). Scalebar 10µm.

B) Rectangular crops are manually defined, marking vessel segments at different z-levels. The vessel segments are classified as PA (*red*), Sphincter (*cyan*), Bulb (*light blue*), and 1st order capillary (*blue*). Scalebar 10µm.

C) A zt depiction of the changes in vessel area of the four different vessel segments during the 100s 3D imaging session. Here, the normalized changes in vessel areas in the rectangular xy crops at different z levels are shown in pixel intensity (*Jet colormap*) over time. The *orange box* marks the time points presented as traces in A) from the changing PA area.

D) Binarization of the data shown in C) to define periods of dilations as zt pixels with values >2SD. Notice how some dilations of the capillary do not expand the vessel in all z-levels.

E) A zt depiction of the changes in vessel area during the 3D imaging session. *Red*: normalized vessel area detected with Texas red and *Green*: average GFAPGCaMP6f signal from astrocyte end-feet surrounding that specific vessel segment. *Blue* indicates tone stimulation. The *red* in the bar below indicates the movement of the mouse.

F) Summary of periods of dilations in each of the four vessel segments shown in D), now binarize to disregard the different degrees of dilation at different z-levels. From this, the heterogeneity of dilation patterns in the individual dilations is evident.

G) Overlay of the dilation patterns of the different vessel segments summarized in F). The color code shows the number of vessel segments participating in each dilation at different times during the 100s acquisition period. The graphical representation shows that not all vessel segments participate in each dilation.

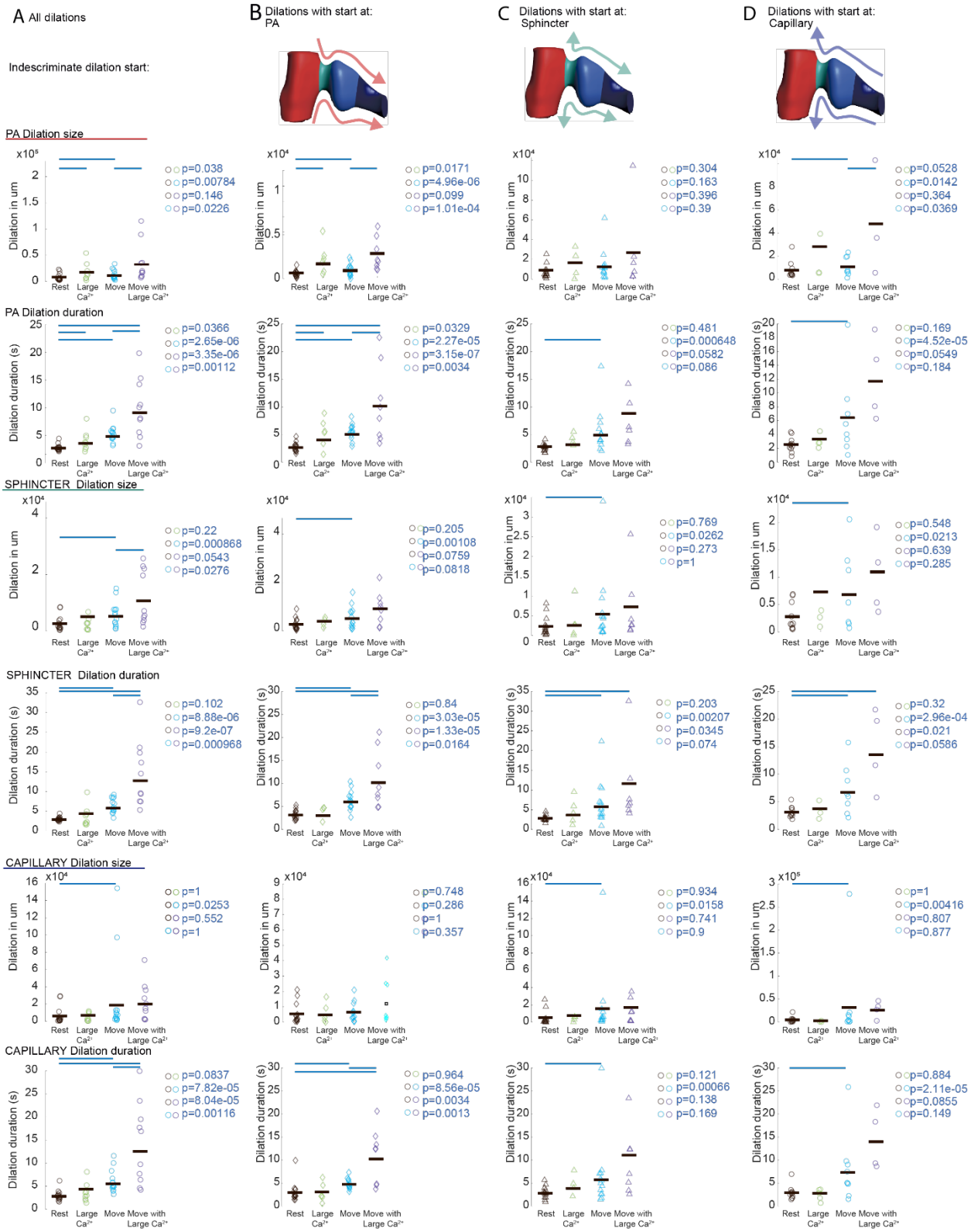
A All dilations
B Dilations with start at: PA
C Dilations with start at: Sphincter
D Dilations with start at: Capillary
Indescriminate dilation start:
PA Dilation size
PA Dilation duration
SPHINCTER Dilation size
SPHINCTER Dilation duration
CAPILLARY Dilation size
CAPILLARY Dilation duration
Dilation in um
Dilation duration (s)
Rest
Large Ca2+
Move
Move with Large Ca2+
p=0.038
p=0.00784
p=0.146
p=0.0226
p=0.0171
p=4.96e-06
p=0.099
p=1.01e-04
p=0.304
p=0.163
p=0.396
p=0.39
p=0.0528
p=0.0142
p=0.364
p=0.0369
p=0.0366
p=2.65e-06
p=3.35e-06
p=0.00112
p=0.0329
p=2.27e-05
p=3.15e-07
p=0.0034
p=0.481
p=0.000648
p=0.0582
p=0.086
p=0.169
p=4.52e-05
p=0.0549
p=0.184
p=0.22
p=0.000868
p=0.0543
p=0.0276
p=0.205
p=0.00108
p=0.0759
p=0.0818
p=0.769
p=0.0262
p=0.273
p=1
p=0.548
p=0.0213
p=0.639
p=0.285
p=0.102
p=8.88e-06
p=9.2e-07
p=0.000968
p=0.84
p=3.03e-05
p=1.33e-05
p=0.0164
p=0.203
p=0.00207
p=0.0345
p=0.074
p=0.32
p=2.96e-04
p=0.021
p=0.0586
p=1
p=0.0253
p=0.552
p=1
p=0.748
p=0.286
p=1
p=0.357
p=0.934
p=0.0158
p=0.741
p=0.9
p=1
p=0.00416
p=0.807
p=0.877
p=0.0837
p=7.82e-05
p=8.04e-05
p=0.00116
p=0.964
p=8.56e-05
p=0.0034
p=0.0013
p=0.121
p=0.00066
p=0.138
p=0.169
p=0.884
p=2.11e-05
p=0.0855
p=0.149

Sup. Figure S4. Dilation volume and duration in different vessel segments do not depend on the dilation initiation site but have different sensitivities to global Ca2+ events and movement.

A) Average dilation size and duration of PA, sphincter, and capillary vessel segments during rest; large astrocytic Ca2+ activities alone; movement activity; or movements with large Ca2+ activities. This column shows results independent of the dilation initiation site. PA dilation size and duration (*Two top rows*) increase during isolated Ca2+ events, which is not the case at the sphincter (*middle rows*) or the 1st order capillaries (*two bottom rows*). With respect to movement without a global Ca2+ activity, it would increase both the dilation size and duration of the sphincter, but at the capillaries or PA, it would only prolong the dilation duration, not the volume. At all vessel segments, the dilations were both larger and longer when a global Ca2+ activity occurred during movements (*black*: During rest 162±31.2 dilations, *green*: with large Ca2+ 4.2±2.0 dilations/FOV, *azure*: During move no Ca2+ 47.6±22.1 dilations/FOV, *violet*: During move with large Ca2+ 6.5±2.5 dilations/FOV).

B) Average dilation volume and duration at PA, sphincter, and capillary vessel segments from dilations with a perceived initiation at the PA that indicates the dilation arrives from the PA compartment. The results were not different from when all dilations were averaged indiscriminately at the dilation initiation site (*black*: During rest 50.9±12.8 dilations/FOV, *green*: with large Ca2+ 1.92±0.8 dilations/FOV, *azure*: During move no Ca2+ 15.0±7.1 dilations/FOV, *violet*: During move with large Ca2+ 2.1±0.9 dilations/FOV).

C) Average dilation volume and duration at PA, sphincter, and capillary vessel segments from dilations when the dilation began at the sphincter. These dilations do not show a sensitivity to large astrocytic Ca2+ activities but appear otherwise not different from when all dilations were average indiscriminately of the dilation initiation site (*black*: During rest 40.3±8.5 dilations/FOV, *green*: with large Ca2+ 1.6±0.5 dilations/FOV, *azure*: During move no Ca2+ 12.4±6.9 dilations/FOV, *violet*: During move with large Ca2+ 2.3±1.0 dilations/FOV).

D) Average dilation volume and duration at PA, sphincter, and capillary vessel segments from dilations with a perceived initiation at the capillary that indicates the dilation arrives from the capillary compartment. These dilations were less affected by large astrocytic Ca2+ activity, but results appear otherwise not to differ from when all dilations were averaged indiscriminately at the dilation initiation site. (*black*: During rest 56.4±13.0 dilations/FOV, *green*: with large Ca2+ 2.1±0.8 dilations/FOV, *azure*: During move no Ca2+ 14.7±7.9 dilations/FOV, *violet*: During move with large Ca2+ 2.4±0.7 dilations/FOV).

All p-values are from the t-test, modified with Holm correction for multiple comparisons N=20 FOV in 6 mice. Fik p>0.05, the two data columns are indicated with a blue line above.

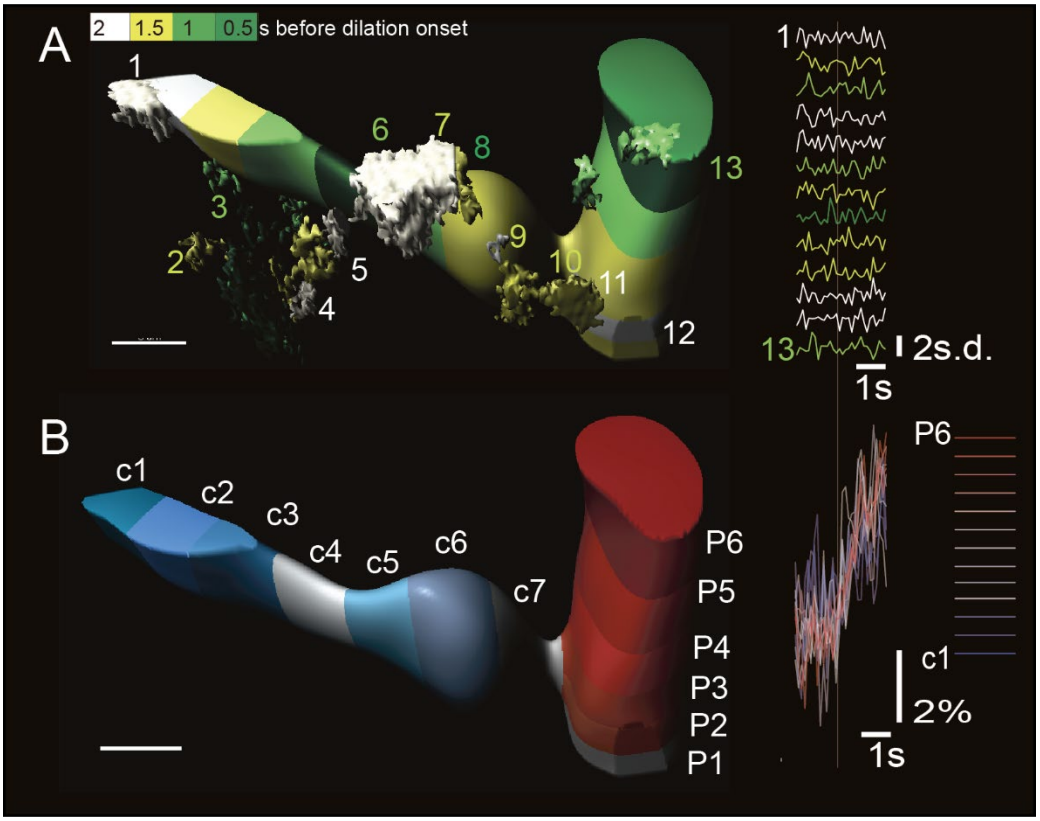

Sup. Figure S5. Example of pre-dilation Ca2+ activities in astrocytic end-feet and sequence of dilation of different vessel segments.

A. Regions of astrocytic Ca2+ activity in the last 1.5 seconds prior to a multi-compartment dilation arriving from the capillary. Color scale indicates the onset time of the Ca2+ activity in the ROIs on astrocytic structures and in the end-feet along the vessel surface(shown as segments of the vessel mask). *White*= 2 s before dilation onset; *Dark green*= just before dilation onset. The average Ca2+ activity in the ROIs is shown to the right. The pre-dilation astrocytic Ca2+ activity occurs first in two different locations: further downstream on the capillary (*ROI1*) and at the sphincter (*ROI11*), but also further from the end-feet (ROI4 and ROI5). From there, the Ca2+ appears to spread locally within a couple of micrometers.
B. The dilation sequence of different vessel segments is indicated in the color code. *White* indicates early dilations; *Blue* is the late parts of the capillary dilations; *Red*: is the late parts of the PA dilations. At this junction, the capillary dilation begins at the segment just after the bulb (*c4*). Once dilation is initiated at the capillary, it quickly spreads to the sphincter (*c7*) and only then to the rest of the capillary, and the PA dilates. The dilation of the individual vessel segments is shown to the right. Scalebar 8µm.

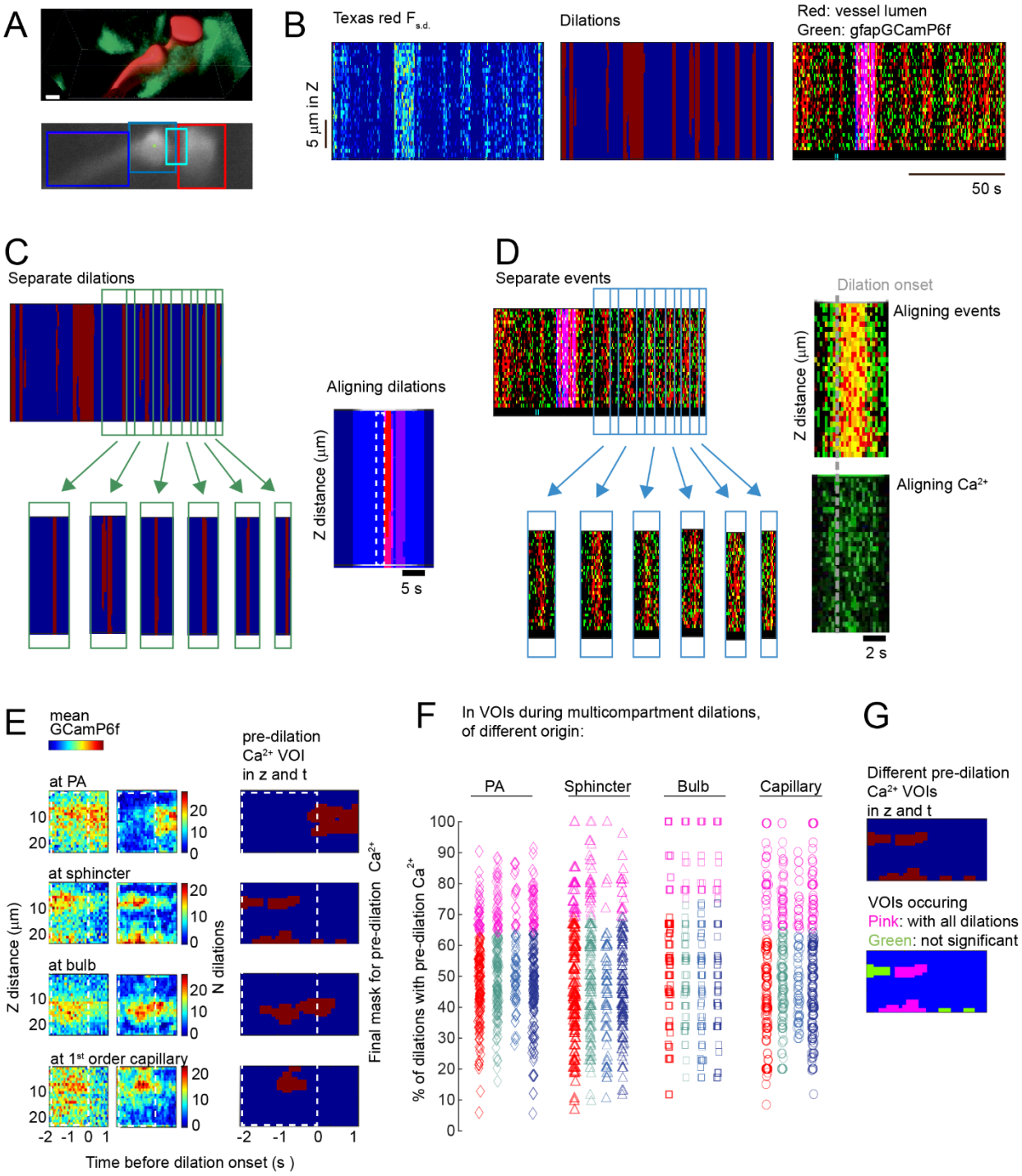

Sup. Figure S6. Method to detect regions with pre-dilation astrocytic Ca2+ signals and quantification of prevalence.

A) Cumulative average of a 3D timeseries taken from the auditory cortex of a Texas red-dextran injected *GFAPCreERT2:GCaMP6f* mouse. Example of 3D-FOV depicting a 1st order capillary branch from a PA. *Top*: entire xyz stack 64-86 µm below the cortical surface. *Red*: shows masked

vessel lumen. *Green*: GFAPGCaMP6f. *Bottom*: focal plane 72 µm below the surface. The average Texas red dextran signal from the vessel lumen and four manually defined rectangles identify the different vessel segments. *Red*: PA, *Cyan*: Sphincter, *Light blue*: Bulb, *Blue*: Capillary. Scalebar 5µm.

B) A zt detection of dilation events of PA across the different z-levels during the 100s 3D imaging session. *Left*: The normalized changes in vessel area in the rectangular xy crop at different z levels are shown in pixel intensity (*Jet colormap*) over time. *Middle*: Binarization showing a period of dilations (*red*) and their expansion along the z-axis. Right: Normalized signal from Texas red (*red*) and GFAPGCaMP6f (*green*). *Blue*: indicates tone stimulation. *Cyan* in the bar below shows the movement of the mouse.

C) *Left*: Periods with dilation events detected in the zt rendering were considered separate events and cropped (*green boxes*). *Right*: These crops were then aligned based on the onset of the dilations to allow for the detection of recurrent activity in relation to the dilation in a 2 second pre-dilation period (*white dashed line)* as well as during the first second of dilations.

D) Aligning the onset of the dilation events detected in c), average fluorescence activity from the GFAPGCaMP6 signal shows astrocytic Ca^{2+} activity rise before and lasting through dilations.

E) Defining zt position of astrocytic pre-dilation Ca^{2+} activity in different end-feet ROIs on the vessel segments. Two seconds period before dilation onset marked with a white dashed box. *Left*: mean GFAPGCaMP6f signal in end-feet in relation to dilation. *Middle*: Number of dilations during all imaging sessions with astrocytic Ca2+ at this time and depth in z. Detected by summarizing masks created from the mean GFAPGCaMP6f signals. N Shown in *pseudocolor*. *Right*: Binarization after Gaussian filtering defines the pre-dilation Ca^{2+} signal in cortical depth and time relative to the dilation onset. This mask was then used to evaluate the presence of this specific pre-dilation activity, occurring at a particular time and place, in the astrocyte Ca^{2+} activity prior to dilation events grouped by dilation patterns.

F) The percentage of dilations preceded by the different pre-dilation Ca2+ signals in different end-feet ROIs depends on dilation onset. The level of prevalence was used to define whether pre-dilation activities could be considered concurrently present in relation to the dilation to be considered in this investigation. The colors of the data points indicate which vessel segment the astrocytic end-feet ROI ensheathed (*red*: PA, *cyan*: sphincter, *light blue*: bulb, *blue*: capillary). The *pink* data points mark the pre-dilation Ca2+ activities that were significantly present before dilations of a specific pattern. The limit for counting the presence of a pre-dilation signal was if it occurred with 100 % of dilations, subtracted from the 0.1 confidence limit, which again depended on the number of dilations of a given dilation pattern.

G) Illustration of the division of a group of potential pre-dilations Ca^{2+} VOIs. *Top*: VOIs at the sphincter shown in E). *Below*: based on whether they occur with all dilations (*Pink*) or are not significantly present before the dilations (*Green*).

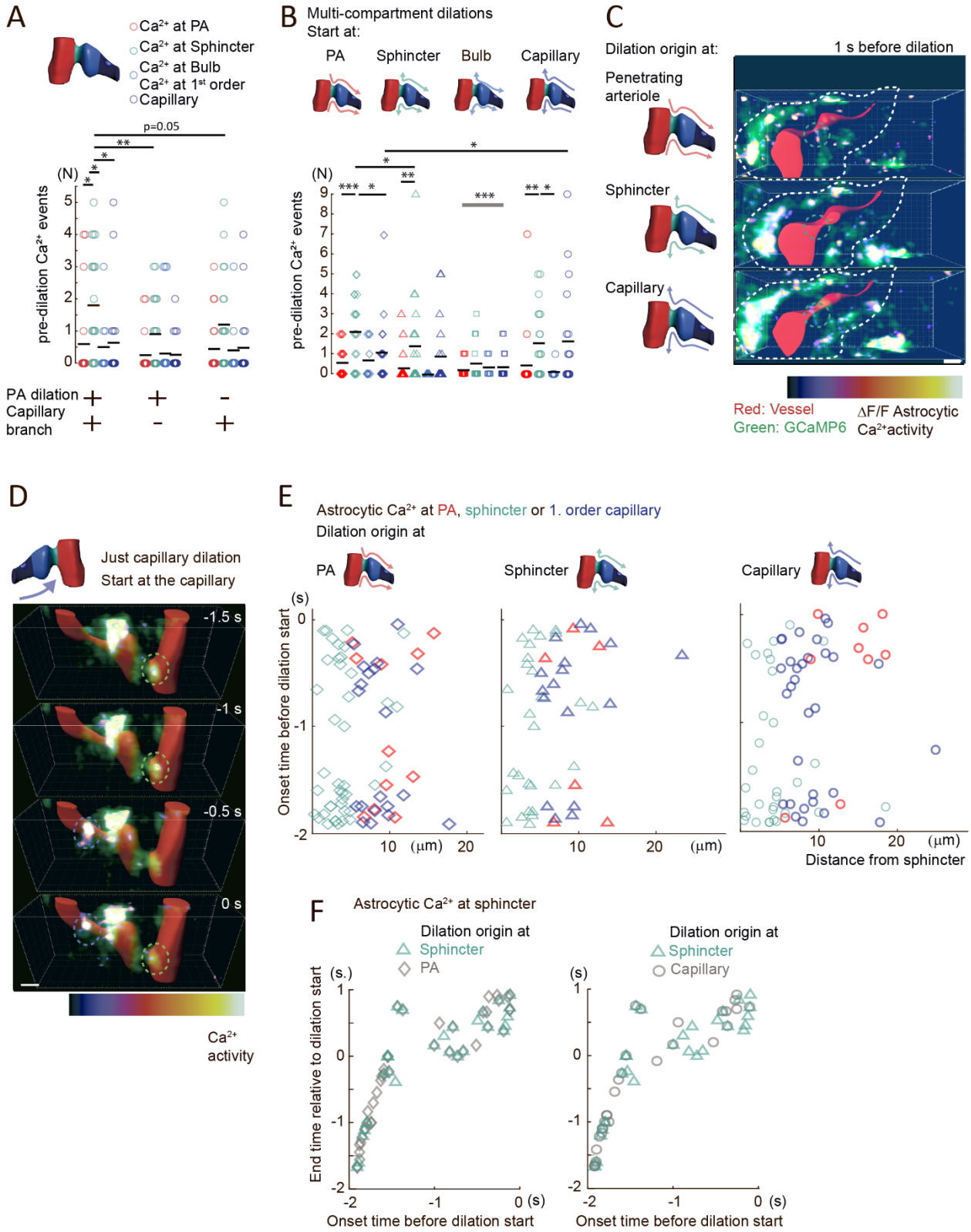
A
Ca2+ at PA
Ca2+ at Sphincter
Ca2+ at Bulb
Ca2+ at 1st order
Capillary
p=0.05
(N)
pre-dilation Ca2+ events
PA dilation
Capillary branch
B
Multi-compartment dilations
Start at:
PA
Sphincter
Bulb
Capillary
C
Dilation origin at:
1 s before dilation
Penetrating arteriole
Sphincter
Capillary
Red: Vessel
Green: GCaMP6
ΔF/F Astrocytic Ca2+activity
D
Just capillary dilation
Start at the capillary
-1.5 s
-1 s
-0.5 s
0 s
Ca2+ activity
E
Astrocytic Ca2+ at PA, sphincter or 1. order capillary
Dilation origin at
PA
Sphincter
Capillary
Onset time before dilation start
Distance from sphincter
F
Astrocytic Ca2+ at sphincter
Dilation origin at
Sphincter
PA
Capillary
End time relative to dilation start
Onset time before dilation start

Sup. Figure S7. Pre-dilation astrocytic Ca^{2+} activity in end-feet is most prevalent and earlier at the sphincter during multi-compartment dilations and consists of local punctate events that do not spread in a wave.

A. Count of pre-dilation astrocytic end-foot Ca2+ activities during different dilation types, either multi-compartmental or of just PA or the 1st order capillary branch. Pre-dilation activity shows a prevalence at the sphincter during multi-compartment dilations (*left*) and a higher prevalence compared to dilation of just the PA (*middle*) or the capillary branch (*right*). (Wilcoxon with Holm-correction for multiple comparisons, All ves dil. Ca2+ at PA (*red*) vs. at sphincter(*cyan*): p=0.012, at sphincter vs. at bulb(*light blue*): p=0.017, at sphincter vs. at capillary (*blue*): p=0.0178; After a Kruskal Wallis test, Ca2+ at sphincter All ves vs just PA dil.: p=0.0096, All ves vs just 1st branch dil.: p=0.05; 82.7±20.1 multi-compartment, 15.3±4.5 just PA and 61.4±14.7 just capillary branch dilations/FOV, N=20 FOV in 6 mice).
B. The number of pre-dilation Ca2+ activities seen during multi-compartment dilations is sorted depending on the dilation direction. For multi-compartment dilations involving all the vessel compartments in the FOV, the pre-dilation astrocyte end-foot Ca2+ elevation occurred more frequently at the sphincters, independent of the initiation site at the PA (*left, diamonds*), at the sphincter/ bulb (*middle, triangle/squares*) or the capillaries (*far right*, *circles*). Tested with Kruskal Wallis ANOVA, then Wilcoxon with Holm-correction for multiple comparisons: (a) dilation starting at PA: end-foot Ca2+ at sphincter(*cyan*) vs. PA (*red*): p= 5.5*10-4; at sphincter vs. at bulb(*light blue*): p=0.062; at sphincter vs. at capillary(*blue*): p = 0.027; (b) dilation starting at sphincter: end-foot Ca2+ at sphincter vs. at PA: p = 0.006; at sphincter vs. at bulb: p=0.25; at sphincter vs. at capillary: p = 0.41; (c) dilation starting at capillaries: end-foot Ca2+ at sphincter vs at PA: p = 0.0011; at sphincter vs at bulb: p=0.048; at capillary vs at Sphincter: p=0.21. Much less astrocytic Ca2+ was seen pre-dilation when the dilation started at the bulb (*squares*, Kruskal Wallis ANOVA to compare all values in the Bulb plot with the other three. Vs Origin PA: p=6.7*10-5, Vs Origin Sphincter: p=0.34; Vs. Origin capillary: p=0.037). Furthermore, pre-dilation end-foot Ca2+ events at the sphincter occurred more frequently when dilation began at the PA than at the sphincter itself (after Kruskal Wallis ANOVA, Wilcoxon test: dilation initiation at PA vs at sphincter: p = 0.019). Likewise, end-foot Ca2+ events at the capillary were significantly more frequent when dilations began in the capillary bed than at the PA (after Kruskal Wallis ANOVA, Wilcoxon test: dilation initiation at capillary branch vs at PA: p=0.029). Starting at PA, sphincter, bulb, and capillary, respectively: 116.1±24.7, 82.4±19.7, 70.4±18.9, 67.2±16.2 dilations/FOV, from N=20 FOVs in 6 mice N=20 FOV in 6 mice.
C. *Left*: Dilations are separated based on three different dilation patterns. *Right*: Example of astrocytic Ca2+ activity (intensity scale) and vascular lumen (masked, *red*) temporally aligned to dilation onset based on dilation pattern of one 3D-FOV x= 56.6µm, y= 17.5µm from 194-216µm below the brain surface. The *white dashed lines*: indicate end-feet; *cyan circles*: the area around the sphincter. Average from the last second before dilation onset shows that astrocytic Ca2+ activity is more substantial prior to dilation arriving from outside the FOV (i.e., the PA or the capillaries, *white arrow*). Scalebar 5µm.

D. Representative time series of astrocytic Ca2+ activity preceding a mono-compartment dilation spreading from the capillary bed up to the sphincter. 3D-FOV x= 75.5µm, y= 23.6µm, z=31µm as in A. Dilation start time = 0. In this case, the astrocytic Ca2+ activity at the sphincter (*green circle*) is weaker and shorter than in panel F *right*, and ends before dilation. Another pre-dilation local activity with 1s later onset is seen at the capillary (*blue circle*). Scalebar 7µm.
E. The onset time of pre-dilation astrocytic Ca2+ activities depends on the distance from the sphincter (*red*: in PA end-feet; *cyan*: in sphincter end-feet; *blue*: in capillary end-feet) when sorted based on the dilation point of origin (*diamonds*: PA; *triangles*: sphincter; *circles*: capillaries). The distribution shows that the activity does not spread like a wave in front of the dilation. Starting at PA, sphincter and capillary, respectively: 116.1±24.7, 82.4±19.7, 67.2±16.2 dilations/FOV, from N=20 FOVs in 6 mice.
F. Onset and end-time of pre-dilation Ca2+ activities at the sphincter before multi-compartment dilations arrive from either the PA (*Grey*) or the capillary (*Grey*) or initiated at the sphincter (*cyan*) in the 3D-FOV. Show two groups of activities and that some persist after dilation onset.

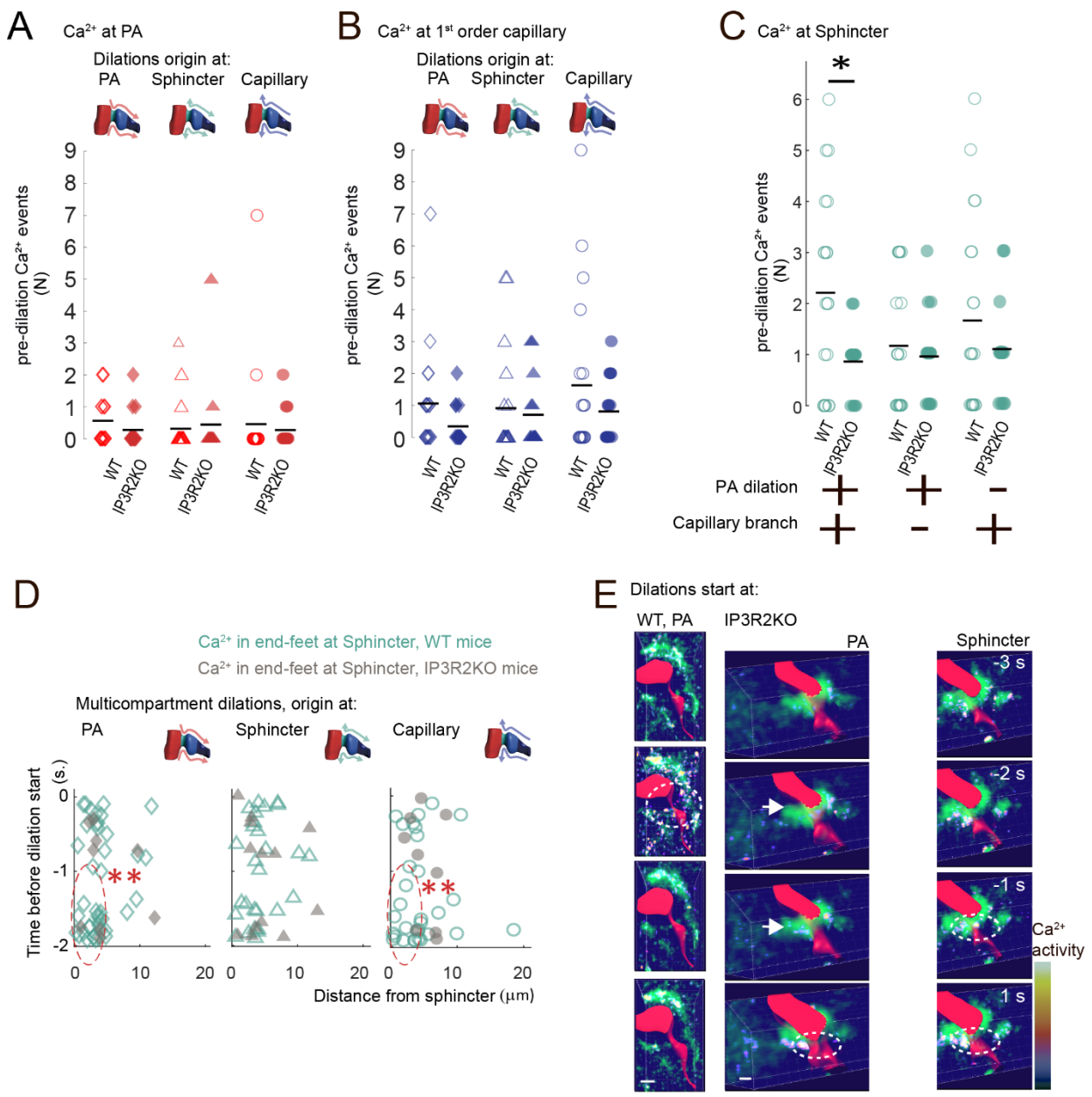

Sup. Figure S8. Not all pre-dilation astrocytic Ca^{2+} activity in end-feet was IP3R2 dependent, but in dilations arriving from the capillaries, some activity in end-feet at the capillaries was depleted.

A. The count of pre-dilation Ca2+ activities in end-feet covering the PA in WT (*red, open*) vs. IP3R2KO (*red, solids*) mice in multicompartment dilation arriving from the PA or the capillaries or initiated within the 3D-FOV at the sphincter. No difference was found between the FOVs in WT or IP3R2KO mice (Origin PA: 116.1±24.7 dilations/FOV, N=20 FOV, 6 WT mice vs. 130.3±35.4 dilations/FOV, N=14 FOV, 4 IP3R2KO mice; Origin Sphincter: 82.4±19.7 dilations/FOV, N=20 FOV, 6 WT mice vs 76.9±21.9 dilations/FOV, N=14 FOV, 4 IP3R2KO mice; Origin capillary: 67.2±16.2 dilations/FOV, N=20 FOV, 6 WT mice vs 50.9±14.3 dilations/FOV, N=14 FOV, 4 IP3R2KO mice).

B. The count of pre-dilation Ca2+ activities in end-feet covering the capillaries in WT (*blue, circles*) vs. IP3R2KO (*blue, solids*) mice in multicompartment dilation arriving from the PA or the capillaries or initiated within the 3D-FOV at the sphincter. No difference was found between the FOVs in WT or IP3R2KO mice(Origin PA: 116.1±24.7 dilations/FOV, N=20 FOV, 6 WT mice vs. 130.3±35.4 dilations/FOV, N=14 FOV, 4 IP3R2KO mice; Origin Sphincter: 82.4±19.7 dilations/FOV, N=20 FOV, 6 WT mice vs 76.9±21.9 dilations/FOV, N=14 FOV, 4 IP3R2KO mice; Origin capillary: 67.2±16.2 dilations/FOV, N=20 FOV, 6 WT mice vs 50.9±14.3 dilations/FOV, N=14 FOV, 4 IP3R2KO mice).
C. The count of pre-dilation Ca2+ activities in end-feet covering the sphincter in WT (*cyan, circles*) vs. IP3R2KO (*cyan, solids*) mice in multicompartment dilations or single-compartment dilations involving just the PA or the capillary. The pre-dilation Ca2+ was reduced in end-feet at the sphincter in IP3R2KO mice during multicompartment dilations (Mann-Whitney p=0.028, 82.7±20.1 dilations pr N=20 FOV, 6 WT mice vs 75.3±16.7 dilations pr N=14 FOV, 4 IP3R2KO mice), not in dilations that did not spread across the sphincter (Just 1st order capillary branch dilations, 61.4±14.7 dilations pr N=20 FOV, 6 WT mice vs 83.3±25.6 dilations/FOV, N=14 FOV, 4 IP3R2KO mice, Just PA dilations, 15.3±4.5 dilations pr N=20 FOV, 6 WT mice vs 10.3±2.5 dilations/FOV, N=14 FOV, 4 IP3R2KO mice).
D. Onset time and distance from sphincter of all pre-dilation Ca2+ activities seen prior to multi-compartment dilations arriving from the capillary compartment. The pre-dilation Ca2+ signals absent in the IP3R2KO mice are those occurring early, furthest from the sphincter.
E. Example time-series of astrocyte Ca2+ dynamics preceding multicompartment dilations starting either at the PA (WT: *left*, IP3R2KO: *middle*) or the sphincter in an IP3R2KO mouse(*right*). The WT 3D-FOV is taken from 194-216 µm and the IP3R2KO from 85-115 µm below the cortex surface. Timing is from 3 sec before to 1 sec after dilation onset. *Red*: Texas red-dextran masked signal highlights vessel lumen; *green*: astrocyte GCaMP6f signal highlights active perivascular end-feet. *Pseudocolor scale*: normalized Ca2+ activity. Dashed white circles demark Ca2+ dynamics at the sphincter region. White arrows point to where pre-dilation Ca2+ activity is usually seen in WT mice but is absent in IP3R2KO mice. Scalebars 5µm.

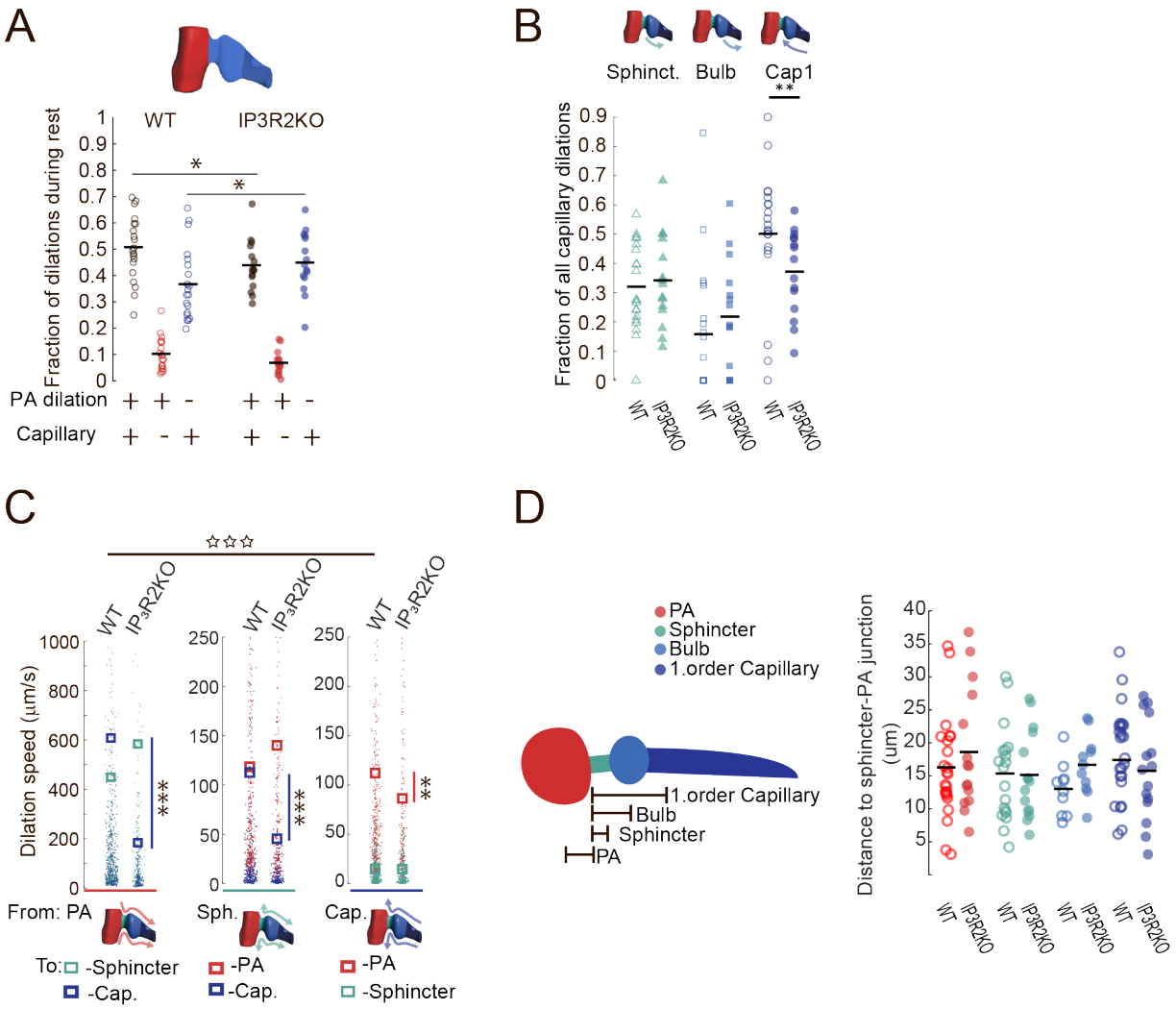

Sup. Figure S9. Dilation patterns and speed of dilation spread in IP3R2KO vs WT mice.

A) The fraction of all dilations in which one or all compartments dilated during rest. The dilation pattern was changed in IP3R2KO mice, showing an even larger fraction of dilations involving just one vessel compartment (Mann-Whitney test, All vessel parts: p=0.037, 1st branch p=0.02 WT: 236±45 dilations per N=20 FOV, 6 mice, IP3R2KO 235±53 dilations/FOV, N=14 FOV, 4 mice).

B) Fraction of dilations with different initiation sites staying within the capillary compartment. Dilation origin is either *cyan, triangles*: Sphincter; *light blue, squares*: Bulb or *blue, circles*: capillary. In the IP3R2KO mice (*solids*), fewer dilations were observed to arrive from the capillary bed (Mann-Whitney test: p=0.007, 99.62± 21.69 dilations/FOV, N=20 FOV, 6 WT mice, 120.94± 35.64 per N=14 FOV, 4 IP3R2KO mice).

C) The speed with which dilations spread between vessel segments in dilation was observed across all FOVs and mice. Color code *Red*: PA; *cyan*: Sphincter; *light blue*: Bulb; *blue*: capillary. Considering the three most common points of initiation. The speed by which dilations spread between the PA and capillary compartments in WT mice depended strongly on the initiation site and was much faster from PA to capillary than in the opposite direction from capillary to PA

(Open stars, Mann-Whitney test, $p=1.9*10^{-5}$, PA to Capillary N=366 dilations, Capillary to PA N=323 dilations, 20 FOVs, 6 mice). In the IP3R2KO mice, the speed by which dilations spread from one vessel segment to the next was reduced. Considering the three most common points of initiation, this was the case regardless of whether the dilation arrived from the PA (*left*)(Mann-Whitney test capillary: $p=1.5*10^{-7}$, WT: N=366 dilation events, IP3R2KO: N=142 dilations), were initiated at the sphincter (*middle*)(Mann-Whitney test: $p=6.02*10^{-7}$, WT: N=329 dilations, IP3R2KO: N=239 dilations) or arrived from the capillary bed (*right*) (Mann-Whitney test: p=0.0076, WT: N=323 dilations, IP3R2KO: N=145 dilations). Data from N=20 FOV, 6 WT mice, N=14 FOV, 4 IP3R2KO mice.

D) *Left*: Diagram of how the distance between vessel segments and the connection point between the PA and sphincter was estimated. *Red*: PA; *cyan*: Sphincter; *light blue*: Bulb; *blue*: capillary. *Right*: The distance from different vessel segments to the connection point between PA and sphincter. No difference was found in WT vs IP3R2KO mice, though a large diversity was observed at all levels. Data from N=20 FOV, 6 WT mice, N=14 FOV, 4 IP3R2KO mice.

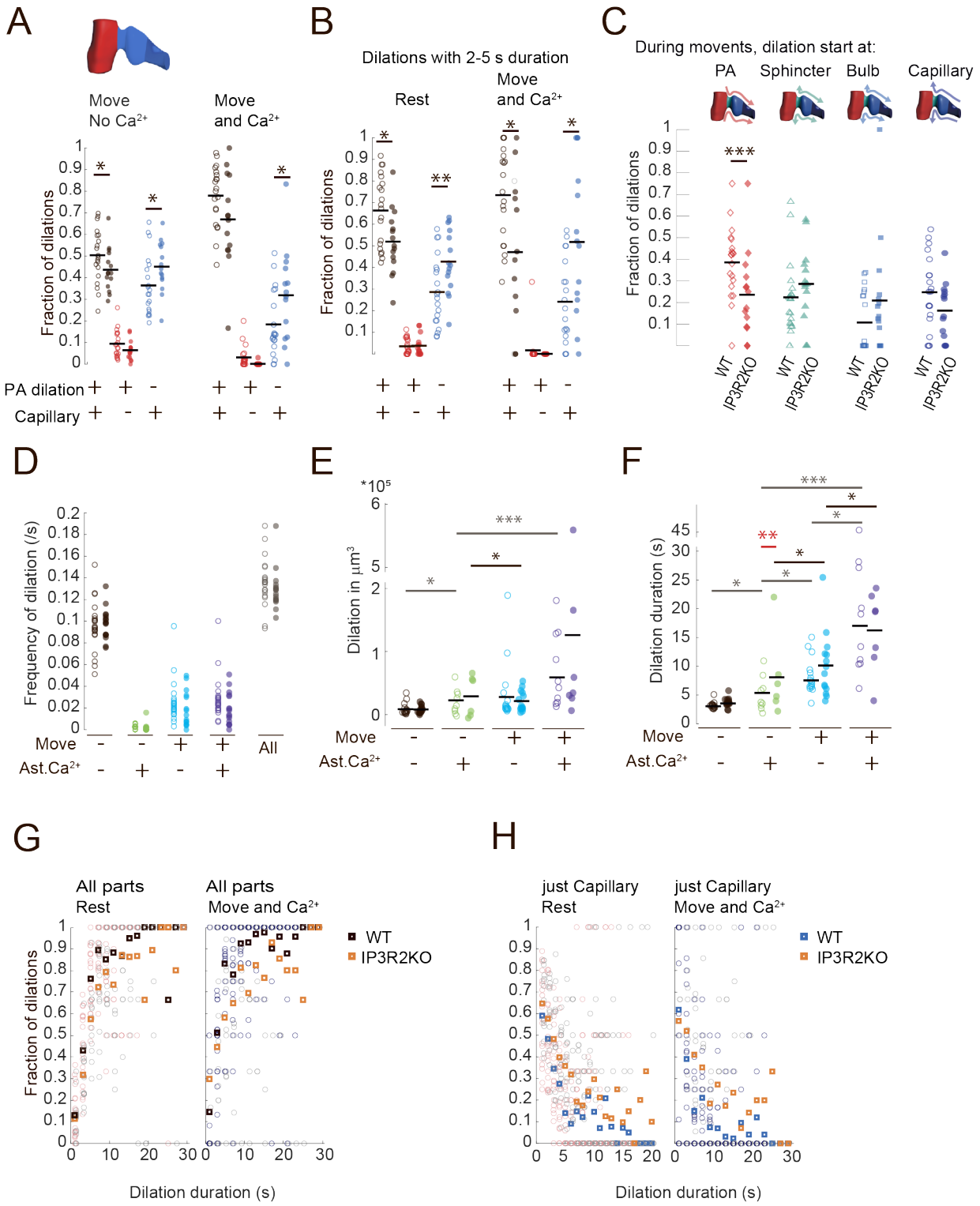

Sup. Figure S10. Dilation patterns and speed of dilation spread in IP3R2KO vs WT mice.

A) Fraction of dilations involving different vessel compartments during movement (*left*) and during movements and large astrocytic Ca2+ (*right*) in WT (*open*) vs IP3R2KO (*solid*) mice. Most dilations included all compartments (*black*), but this fraction appeared reduced in the IP3R2KO mice (Mann-Whitney test, Movements: Multi-compartment: p=0.045 capillary (*blue*): p=0.017 Movements and global Ca2+: Multi-compartment: p=0.066, capillary (*blue*): p=0.036, fraction of just PA dilations (*red*) did not significantly changes, WT: N=20 FOV, 6 mice, IP3R2KO N=14 FOV, 4 mice).

B) Fraction of dilations involving different vessel compartments during rest and movement and large astrocytic Ca2+ in WT vs IP3R2KO mice, considering only dilations with a duration between 2-5 sec. Both in rest and during movement/large Ca2+, fewer dilations included all compartments and more just the 1st capillary branch in the IP3R2KO compared to WT mice (Mann-Whitney test, At rest: Multi-compartment (*black*): p=0.011, capillary (*blue*): p=0.007, Move/Ca2+: Multi-compartment (*black*): p=0.015, capillary (*blue*): p=0.012, fraction of just PA dilations (*red*) did not significantly changes,, WT: N=20 FOV, 6 mice, IP3R2KO N=14 FOV, 4 mice).

C) During movements, the fraction of multi-compartment dilations beginning at the PA was significantly reduced in the IP3R2KO mice. (Mann-Whitney test: PA (*red*): p=0.0041, Sphincter (*cyan*): p=0.059, Bulb (*light blue*): p=0.13, capillary (*blue*).: p=0.070, WT N=20 FOV in 6 mice, IP3R2KO N=14 FOV, 4 mice).

D) The frequency of dilations shows no difference between WT and IOP3R2KO mice. Data from N=20 FOV, 6 WT mice, N=14 FOV, 4 IP3R2KO mice. (*black*: During rest, *green*: with large Ca2+, *azure*: During move no Ca2+, *violet*: During move with large Ca2+, number of dilations, respectively; In WT (*open circles*) 162±31.2 dilations, 4.2±2.0 dilations, 47.6±22.1 dilations 6.5±2.5 dilations/FOV, N = 20 FOV in 6 mice; in IP3R2KO (*solid circles*): 176±39.8 dilations, 2.27±1.61 dilations, 34.1±15.2 dilations 1.73±1.28 dilations/FOV, N = 14 FOV in 4 IP3R2KO mice).

E) Average size of dilation (in μm^3) pr 3D-FOV during rest (*black*), large astrocytic Ca2+ (*green*), movements (*azure*), or when both occur simultaneously (*violet*) in WT (*open*) vs. IP3R2KO (*solid*) mice. The activity of the mouse had a significant effect on dilation size in both mice types (T-test: <u>WT</u>: Large Ca2+ events p=0.033, Movement p=0.0678, Both p=0.00036, N=20 FOV in 6 mice. <u>IP3R2KO</u>: Large Ca2+ events p=0.069, Movement p=0.019, Both p=0.084, N=14 FOV in 4 mice), but no difference is found between the two groups of mice (Friedman test: T-test, <u>WTvsIP3R2KO</u>: Rest p=0.81, Large Ca2+ events p=0.58, Movement p=0.59, Both p=0.22, WT N=20 FOV in 6 mice, IP3R2KO N=14 FOV in 4 mice). (*black*: During rest 162±31.2 dilations/FOV, *green*: with large Ca2+ 4.2±2.0 dilations/FOV, *azure*: During move no Ca2+ 47.6±22.1 dilations/FOV, *violet*: During move with large Ca2+ 6.5±2.5 dilations/FOV, N = 20 FOV in 6 mice).

F) Average dilation durations pr 3D-FOV during rest (*black*), large astrocytic Ca2+ (*green*), movements (*azure*), or when both coincide (*violet*) in WT (*open*) vs. IP3R2KO (*solid*) mice. The activity of the mouse had a significant effect on dilation duration in both mice types (T-test: <u>WT</u>: Large Ca2+ events p=0.0138, Movement p=$4.62*10^{-7}$, Both p=$3.39*10^{-6}$, Movement with vs without Large Ca2+ events p=0.00159, N=20 FOV in 6 mice. <u>IP3R2KO</u>: Large Ca2+ events p=0.078, Movement p=0.00054, Both p=$2.25*10^{-6}$, Movement with vs without Large Ca2+ events p=0.129, N=14 FOV in 4 mice). In addition, a significant prolongation of dilation duration was found in the IP3R2KO mice, but only in dilations occurring during rest (T-test, <u>WTvsIP3R2KO</u>:

Rest p=0.0078, large Ca2+ p=0.26, Movement p=0.094, Both p=0.86, WT N=20 FOV in 6 mice, IP3R2KO N=14 FOV in 4 mice).

G) Comparing fraction of dilations involving all vessel compartments at different dilation durations in WT (*black*, average in bold) vs. IP3R2KO (*orange*, average in bold) mice. The reduced fraction of dilations involving all vessel compartments in the IP3R2KO mice is independent of dilation duration, both during resting and movements and large Ca2+ events.

H) Comparing fraction of dilations involving only the capillary branch at different dilation durations in WT (*blue*, average in bold) vs IP3R2KO (*orange*, average in bold) mice. The increased fraction of dilations involving only the capillary compartments in the IP3R2KO mice is independent of dilation duration, both during resting and movements and large Ca2+ events.

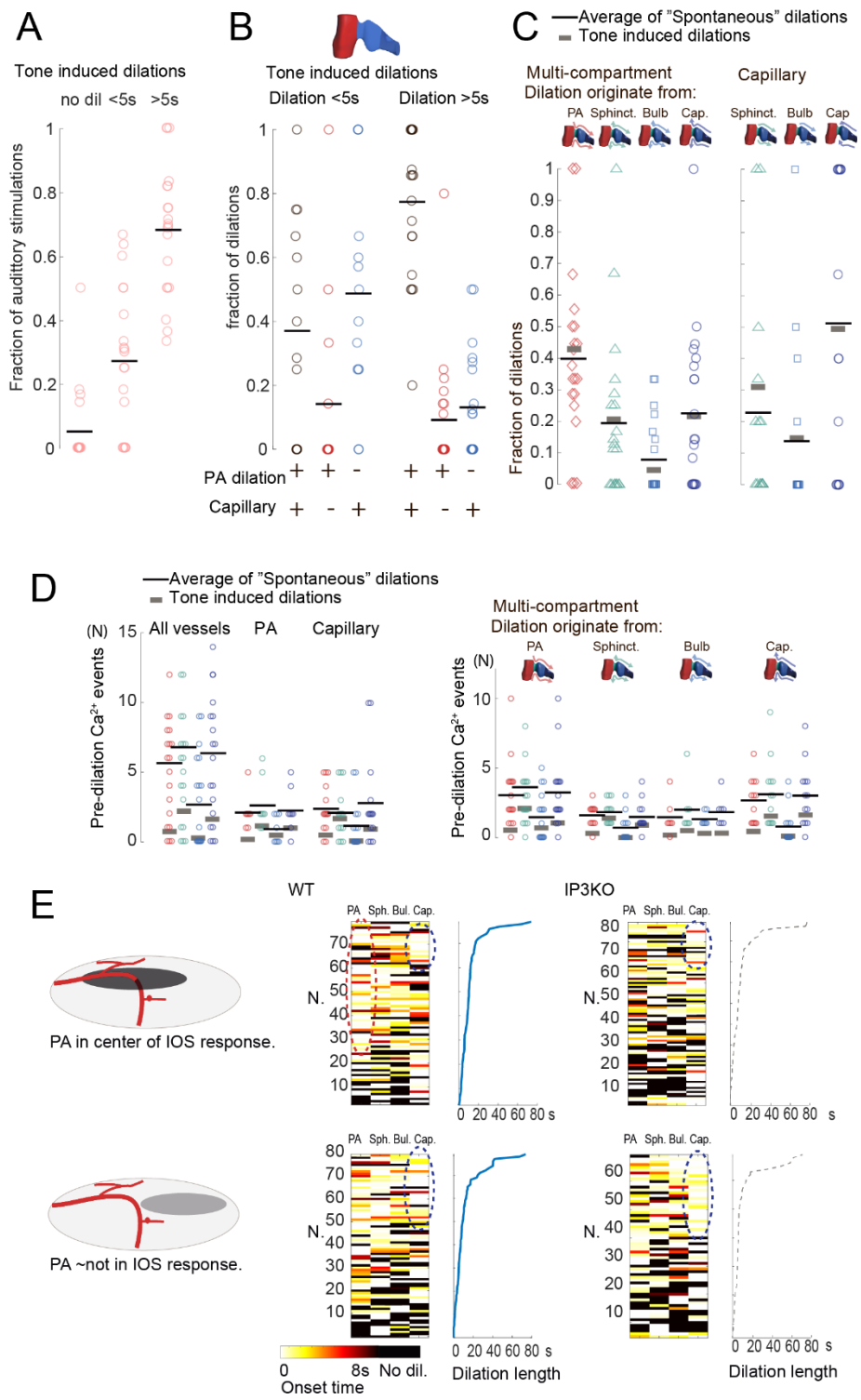

Sup. Figure S11. Dilation patterns were similar in spontaneous and tone-evoked dilations.

A) Dilatory response pr FOV as a fraction of all auditory stimulations. Only a few stimulations did not trigger any dilatory response (no dil). On average, ~ 30% triggered a <5s dilation, and > 65% triggered a >5s dilation. From 7.55±1.79 dilations/FOV, N=20 FOV in 6 mice.

B) The ratio of multicompartment(*black*) or single compartment dilations (*red*: PA, *blue*:1st order capillary) to auditory stimulations pr FOV, separated based on duration. As with spontaneous dilations, more multicompartment dilations were detected with longer dilation durations and the duration of the tone-induced dilations was reflected in how often the dilation progressed beyond the sphincter. <5s dilation was often restricted to just the capillary bed, whereas >5s dilations often included all vessel compartments. From 2.15±0.92 <5s dilations/FOV and 5.4±1.33 >5s dilations/FOV, N=20 FOV in 6 mice.

C) The ratio of dilations pr FOV with a different locus of onset in multi-compartment or just capillary dilations. Tone-induced dilations that originated from either the PA (*red, diamond*), the sphincter (*cyan, triangle*), the bulb (*light blue, square*), or the capillary (*dark blue, circle*) are plotted with their comparative spontaneous values (*grey lines*). The distributions between dilation patterns were similar in spontaneous dilations as among the tone-induced dilations.

D) Number of pre-dilation VOIs with astrocytic Ca2+ activity in relation to different tone-evoked dilation patterns. Counted in each FOV (*red*: in PA end-feet; *cyan*: in sphincter end-feet; *light blue*: in bulb end-feet; *blue*: in capillary end-feet). The average number found prior to spontaneous dilations is plotted on top (*grey lines*). *Left*: Count of pre-dilation astrocytic end-foot Ca2+ activities during different dilation types, either multi-compartmental or of just PA or the capillary branch. (Multi-compartment dilation; Just capillary branch dilations or Just PA dilations, respectively; Spontaneous dilations: 82.7±20.1,61.4±14.7, 15.3±4.5 dilations/FOV; Tone induced: 0.6±0.46, 0.65±0.36, 4.15±1.13 dilations/FOV, N=20 FOV, 6 WT mice). *Right*: In relation to induced multicompartment dilations. Pre-dilation Ca2+ was numerous at the sphincter to both tone and spontaneous dilations and reflected the tone-induced dilation pattern in the same way as the spontaneous dilations (Starting at PA, sphincter, bulb and capillary, respectively: Tone induced: 1.98±0.62, 0.85±0.38, 0.45±0.30, 1.25±0.58 dilations/FOV; spontaneous: 116.1±24.7, 82.4±19.7, 70.4±18.9, 67.2±16.2 dilations/FOV, from N=20 FOVs in 6 mice).

E) Dilation patterns were observed in all responses to different tones in all the 3D-FOVs included in this study (WT N = 158 tone responses in 20 FOV in 6 mice, IP3R2KO N = 155 tone responses in 14 FOV in 4 mice). *Left,* patterns associated with tones that evoked a strong IOS response around the PA; *right,* patterns associated with tones that evoked weak or no IOS response around the PA. Dilation responses are ordered according to the dilation duration (*blue plots*), from bottom (shortest) to top (longest). The timing of dilation of individual vessel segments is represented in a white-to-dark-red temporal scale. Dilations with the most extended durations were evoked by tone stimulations with IOS response centered around the PA. They began at either the capillary (*blue dotted line circle*) or PA (*black dotted line circle*) and quickly progressed across the sphincter. In contrast, short dilations were evoked in areas with approximately no IOS responses and often did not involve all compartments. Those that did mainly originated from the capillary (*blue dotted line circle*). In the IP3R2KO mice, the temporal scale indicates the reduced speed of the dilations between the different vessel parts. There were fewer of the longest dilations, with the PA centered on the IOS response, that began at the PA.